Nonlinear Behavioural Models for RF Devices using an Artificial Neural Network Technique

Mengyue Tian

This thesis is presented for the degree of
Doctor of Philosophy

Centre for High Frequency Engineering (CHFE)
School of Engineering, Cardiff University
United Kingdom
September 2024

Abstract

This work focuses on exploring the development of the Cardiff Model (CM) and the Artificial Neural Network (ANN) based behavioural model for reasonable model extrapolation performance while maintaining the interpolation accuracy.

As an opening segment following the theories explained in the literature review, both the CM and the ANN model accuracy are verified. The potential extrapolation problems of the two modelling techniques are investigated in detail. The experiments demonstrate that the determination of the internal model parameters, such as the model order of the CM, the initial values of hidden neuron numbers, weights and biases of the ANN, are the key correlated elements to reasonable/accurate model performance.

One solution to the extrapolation problem with the user-defined CM order is provided. A modified Levenberg-Marquart (LM) backpropagation training algorithm that can be utilised as part of the ANN based behavioural model is introduced. The modified LM algorithm allows the implementation of an ANN technique-based CM coefficient extractor. The invented coefficient extractor is verified with datasets acquired under ideal simulation and practical load-pull measurement scenarios from the Wolfspeed 10 W packaged device. Results prove that the novel coefficient extractor is able to provide interpolation predictions at the same level of accuracy as the conventional CM, at a Normalised Mean Square Error (NMSE) level below - 50 dB. Then, a method that combines the conventional A-B wave-based ANN behavioural model and the invented coefficient extractor for extracting high user-defined order

CM coefficients is also presented. Two sets of practical load-pull measurement data, acquired with the Wolfspeed 10 W packaged device and the WIN NP12 4x25 um on-wafer device, are used for method verification. The coefficients, extracted using the proposed combined method, have been proven with reasonable extrapolation ability and robustness under different measurement scenarios, maintaining the interpolation accuracy at a NMSE level below - 50 dB for the predicted output power and - 40 dB for the predicted efficiency.

Another solution to the configuration of the ANN with the values of internal model parameters is also given. A direct link between the CM and the A-B wave-based ANN behavioural model is established. The established equation set enables an alternative ANN determining method. The ANN models proposed using the determination method can provide accurate prediction for the behaviour acquired from load-pull characterizations of the Wolfspeed 10 W packaged GaN device simulation and a dense load-pull measurement of WIN NP12 4x75 um GaN HEMT at 20 GHz, with NMSE levels lower than - 40 dB, and also guarantee a reasonable extrapolation ability for both device output power and efficiency.

List of Publications

[1] M. Tian, J. Bell, R. Quaglia, E. Azad, P.J. Tasker, "Artificial neural network nonlinear transistor behavioral models: Structure and parameter determination process based on the cardiff model," *IEEE Transactions on Microwave Theory and Techniques*, vol. 73, no. 2, pp. 745–759, 2025. DOI: 10.1109/TMTT.2024.3434959.

[2] M. Tian, J. Bell, R. Quaglia, P.J. Tasker, "An Extraction Method Based on Artificial Neural Network Techniques for Novel Cardiff Model With Reasonable Extrapolation Behavior," *IEEE Microwave and Wireless Technology Letters*, vol. 34, no. 1, pp. 5–8, Jan. 2024. DOI: 10.1109/LMWT.2023.3329979.

[3] M. Tian, J.B. Urvoy, J. Powell, et al, "Application of the Cardiff Model for Orthogonal LMBA Response Prediction," in *2024 IEEE Topical Conference on RF/Microwave Power Amplifiers for Radio and Wireless Applications (PAWR)*, San Antonio, TX, USA, Jan. 2024, pp. 17–20. DOI: 10.1109/PAWR59907.2024.10438664.

[4] M. Tian, J. Bell, E. Azad, R. Quaglia, P. Tasker, "A Novel Cardiff Model Coefficients Extraction Process Based on Artificial Neural Network," in *2023 IEEE Topical Conference on RF/Microwave Power Amplifiers for Radio and Wireless Applications*, Las Vegas, NV, USA, Jan. 2023, pp. 1–3. DOI: 10.1109/PAWR56957.2023.10046221.

[5] W. Yuan, M. Tian, J. Bell, "Implementation Efficiency Comparison Between ANN and the Cardiff Model in ADS," in *2023 International Workshop on Integrated Nonlinear Microwave and Millimetre-Wave Circuits (INMMIC)*, Aveiro, Portugal, Nov. 2023, pp. 1–4. DOI: 10.1109/INMMIC57329.2023.10321776.

Acknowledgement

I would like to express my sincere thanks to my supervisor Dr. James Bell. It was James who shared the information with me about the PhD position after the summer school project in 2019. I have never even imagined to become a PhD student before that. James has been supportive through his intellectual supervision of the project and by sharing his wisdom on life matters. He is always by my side and encourages me whenever I was feeling overwhelmed during the adventurous PhD journey.

Also, lots of thanks to my co-supervisors: Prof. Paul Tasker, who has opened up the directions of the project with his knowledge and experience in the field of measurement and modelling of RF devices, and dedicated his time and patience in explaining all his thoughts and ideas to me; and Dr. Roberto Quaglia, who has been monitoring the measurement work of the project, and providing advice and opportunities for both the project and future work.

I am so lucky to have all my supervisors being supportive, encouraging and understanding throughout the time that I spent in Cardiff. It would not be possible for me to come this far without their help.

And my special thanks to Xin Zhang, who was my mentor during undergraduate time back in China. Joy is not only a teacher but also a friend and, in many ways, like family. Without her encouragement, I would not be brave enough to travel all this far to a different country and start a PhD. Also thanks to all my friends for always being there with me.

I also deeply appreciate the financial support provided by the Chinese Scholarship Council (CSC) and Cardiff University. Also, I would like to thank WIN Semiconductors for providing the transistor samples that were used in this work.

Last but not least, I would also like to profoundly thank all the colleagues from the Centre for High Frequency Engineering group. Thanks to Dr. Ehsan Azad for being the first friend and helping a lot from the starting point of the project, and Dr. Kauser Chaudhry, Dr. Aleksander Bogusz, Alexander Baddeley, Seyed Ghozati, Indy van den Heuvel, Aquila Powell, Derek Kozel, Weihao Yuan and Kris Yuan as the PA design group for always having the coffee breaks together. Thanks to Prof. Adrian Porch for arranging all the walks, and Dr. Heungjae Choi for all the photos, Dr. Samuel Hefford, Dr. Jonny Lees, Dr. Michael Barter, Dr. Rob Batson, Angharad Miles, Kai Silver for all the group activities. Starting a PhD during COVID time is not easy, but the group made it warm and welcomed with all the online and offline team building work. Shout out to Team CHFE!

List of Abbreviations

ADS Advanced Design System

ANN Artificial Neuron Network

BP Back Propagation

CAD Computer-Aided Design

CM Cardiff Model

CW Continuous Waveform

DUT Device Under Test

DWLU Direct Waveform Look Up

FCC Fully Connected Cascade

GaN gallium nitride

HEMT High-Electron-Mobility Transistor

KBNN Knowledge-Based Neuron Network

LM Levenberg-Maquart

LMS Least Mean-Squared

LUT Look Up Table

MLP Multilayer Perceptrons

MSE Mean Squared Error

NMSE Normalised Mean Square Error

PDK Process Design Kit

PHD Poly Harmonic Distortion

SPICE Simulation Program with Integrated Circuit Emphasis

VIOMAP Volterra Input Output Map

VNA Vector Network Analyser

Contents

Abstract ii

List of Publications iii

Acknowledgement v

List of Abbreviations vi

List of Figures xii

List of Tables xix

1 Introduction 1

1.1 Transistor Models for RF/Microwave design 2

1.2 Measurement Systems 4

1.3 Thesis Objective 7

1.4 Chapter Summary 8

References 9

2 Literature Review 12

2.1 Development of Behavioural Models 13

2.2 The Cardiff Model (CM) 18

2.2.1 The Polynomial Formulation of the CM 19
2.2.2 CM Extraction with Tailored Datasets 23
2.3 Artificial Neural Network (ANN) Models 24
2.3.1 Model Structure 25
2.3.2 Back-Propagation (BP) Training Algorithm 30
2.3.3 Model Implementation in MATLAB 33
2.4 Conclusion 35
References 35

3 Extrapolation Analysis and Comparison of the Cardiff Model (CM) and the Artificial Neural Network (ANN) Model 42

3.1 Data Acquisition 43
3.2 The CM Robustness Verification 46
3.2.1 CM with Conventional Mixing Theory 47
3.2.2 CM with Tailored Dataset Analysis 50
3.2.3 Discussion on the CM 53
3.3 The ANN Solution 54
3.3.1 ANN Configuration and implementation 54
3.3.2 The Accuracy and Extrapolation Ability of the Selected ANN Configuration 56
3.3.3 Discussion on the ANN Model 62
3.4 Conclusion 63
References 63

4 Artificial Neural Network (ANN) Based Cardiff Model (CM) Coefficients Extraction Approach 66

4.1 Complexity Comparison of the CM and ANN models 67

4.2 Proposed Algorithm Implementation and Verification 69

4.2.1 Algorithm Modification 69

4.2.2 Invented Coefficients Extractor Verification 72

4.3 Models Combination for Extrapolation Ability 81

4.4 Discussion 95

4.5 Conclusion 96

References 97

5 A Discovery of the Artificial Neural Network (ANN) Structure Defining Method 99

5.1 Proposed ANN Determination Procedure Overview 100

5.1.1 Step 1: Cardiff Model (CM) Equations Reformulation 101

5.1.2 Step 2: General ANN Equations Reformulation 106

5.1.3 Step 3: FCC ANN Equations Reformulation 111

5.1.4 Step 4: Equating Formulations and ANN Model Structure Identification 114

5.1.5 Step 5: FCC ANN Model Parameter determination 116

5.2 Method Verification With Simulations 121

5.2.1 Simulation Data Acquisition 122

5.2.2 Method Created Model Analysis with ρ Sweep 124

5.2.3 Repeated Analysis for DC Component 128

5.2.4 Power and Efficiency Contour Plots 131

5.3 Method Verification with Measurement 132

5.3.1 Model Determination 133

5.3.2 Model Extrapolation Ability 138

5.4 Discussion 140

5.5 Conclusion 141

References 142

6 Summary and Future Work **145**

6.1 Summary 146

6.2 Future Work 147

List of Figures

1.1 Generic Load-Pull Setup Diagram with Device Under Test (DUT) . . 4

1.2 load-pull setup in ADS 6

2.1 S-parameters diagram with DUT 14

2.2 The VIOMAP system diagram 15

2.3 Definition of the truth model in frequency domain 18

2.4 Analysis example in [34] for $B_{2,1}$ Fourier Transformed spectrum samples between - 40 dB and - 60 dB error bar on the trajectory computation dataset at each $n.Sp = n.41$ location ($S_a = 2$, $S_p = 41$ with $N = 739$) allows for the identification of the relevant exponent terms for $\left(\frac{Q_{2,1}}{Q_{1,1}}\right)^n$ (a) and $|A_{2,1}|^m$ (b-c). 24

2.5 General MLP ANN structure 26

2.6 Knowledge-Based ANN structure 26

2.7 The **sigmoid** activation plot with x=[-5 5] range 27

2.8 The **tanh** activation plot with x=[-5 5] range 28

2.9 The **ReLU** activation plot with x=[-5 5] range 28

2.10 KBNN structural diagram with activation function setup 29

2.11 Structural diagram with bias added to the setup 30

2.12 MATLAB ANN toolbox interface 34

3.1 A-pull simulation setup with Wolfspeed 10 W in ADS 43

3.2 $A_{2,1}$ sample (a) and its Fourier Transformed spectrum (b) on a trajectory computation. 44

3.3 $B_{2,1}$ sample (a) and its Fourier Transformed spectrum with -60dB error bar (which refers to an expecting 0.1% accuracy of the extracted model) (b) on the trajectory computation. 45

3.4 $\Gamma_{2,1}$ and the correlated power contours on the Smith Chart collected from the simulation measurement setup with 39.5 dBm as maximum output power level. 45

3.5 Dataset with expanded coverage on the Smith Chart for extrapolation verification (blue) and the design-related dataset (red) for model extraction. 46

3.6 $B_{2,1}$ from measurement compare to $B_{2,1}$ CM prediction with conventional mixing theory 48

3.7 Extrapolation performance with CM extracted using conventional mixing theory (original dataset - red and the CM predictions - black). 49

3.8 Predicted output power contours (0.4 dBm/step, black) with coefficients extracted using conventional CM mixing theory compared to the original simulated results (red). 50

3.9 The expected exponents' $|A_{2,1}|^m(\angle A_{2,1})^n$ values of the CM for extracting coefficients in (n,m). 51

3.10 B_{21} from measurement compare to B_{21} CM prediction with analysis on tailored dataset 52

3.11 Extrapolation performance with CM extracted using analysis on tailored dataset(original dataset - red and the CM predictions - blue). . 52

3.12 Predicted output power contours (0.4 dBm/step, blue) with coefficients extracted using the CM extracted by analysing the tailored dataset compared to the original simulated results (red). 53

3.13 The implemented FCC structure. 56

3.14 The model performance (a) and extrapolation ability (b) of the $B_{2,1}$ from measurement compared to $B_{2,1}$ prediction from ANN with 2 hidden neurons. 57

3.15 The model performance (a) and extrapolation ability (b) of the $B_{2,1}$ from measurement compared to $B_{2,1}$ prediction from ANN with 6 hidden neurons. 58

3.16 The model performance (a) and extrapolation ability (b) of the $B_{2,1}$ from measurement compared to $B_{2,1}$ prediction from ANN with 11 hidden neurons. 59

3.17 Extrapolated output power contours (blue) with 11-hidden-neuron ANN structure compared to the original simulated results (red). . . . 59

3.18 The model accuracy and extrapolation performance summary of the ANN structure with different hidden neuron numbers. 60

3.19 The model performance (a) extrapolation ability (b) of the $B_{2,1}$ from measurement compared to $B_{2,1}$ prediction from ANN with 11 hidden neurons and the random number generator seed changed to 15. 61

3.20 Extrapolated output power contours (blue) with CM extracted using the CM extracted by analysing the tailored dataset compared to the original simulated results (red). 62

4.1 Proposed method summarized flow diagram. 70

4.2 One hidden layer FCC feedforward ANN based CM coefficient extractor structure. 73

4.3 The expected exponents' $|A_{2,1}|^m(\angle A_{2,1})^n$ values (b) of the CM for extracting coefficients in (n,m) for the drain DC current $B_{2,0}$ (a) from the Wolfspeed device load-pull simulation. 74

4.4 Linear FCC feedforward ANN based CM coefficient extractor structure for modelling the drain DC current $B_{2,0}$. 75

4.5 Simulated dataset (black) and ANN based coefficient extractor extracted coefficient performance (red) shown with 0.15 dBm output power steps (a) and 2% efficiency steps (b) contours plotted on the Smith Chart. 76

4.6 Measurement setup for the Wolfspeed device [7]. 77

4.7 Measured load point location of the Wolfspeed device on the Smith Chart. 77

4.8 Two hidden layer FCC feedforward ANN based CM coefficient extractor structure. 78

4.9 Output power contours calculated with the extracted coefficients from the ANN based coefficient extractor (red) vs. Measurement (black) of the Wolfspeed device with NMSE levels of - 72 dB. 79

4.10 Efficiency contours calculated with the extracted coefficients from the ANN based coefficient extractor (red) vs. Measurement (black) of the Wolfspeed device with NMSE level of - 53 dB. 81

4.11 Calculated $A_{2,1}$ surrounding the measured dataset of the Wolfspeed device for the ANN the trained A-B wave-based ANN model to generate the artificial set of extrapolated data. 84

4.12 The performance shown with $\Gamma_{2,1}$ points plotted on the Smith Chart and output power of the coefficients extracted invented ANN based CM coefficient extractor (a,c) and the conventional A-B wave based ANN model (b,d) for the Wolfspeed device. 85

4.13 0.4 dBm Output power contours prediction with the extracted coefficients using the proposed combined method (red) vs. Measurement (black) of the Wolfspeed device where the level NMSE of the interpolation region remains - 61 dB. 87

4.14 Linear A-B wave-based ANN model structure. 88

4.15 Predicted efficiency contours (5.6%/step) calculated with the extracted coefficients using the proposed combined method (red) vs. Measurement (black) of the Wolfspeed device, where the level NMSE of the interpolation region remains - 44 dB. 89

4.16 Measured WIN data. 90

4.17 Calculated $A_{2,1}$ surrounding the measured dataset of the WIN device for the ANN the trained A-B wave-based ANN model to generate the artificial set of extrapolated data. 91

4.18 The performance shown with $\Gamma_{2,1}$ points plotted on the Smith Chart and output power of the coefficients extracted invented ANN based CM coefficient extractor (a,c) and the conventional A-B wave based ANN model (b,d) for the WIN device. 92

4.19 The combined method extracted coefficient performance of the WIN device, shown with predicted output power contours (1.3 dBm/step) on the Smith Chart, where the level of NMSE in the interpolation region remains - 51 dB. 94

4.20 The combined method extracted coefficient performance of the WIN device, shown with predicted efficiency contours (6.4%/step) plotted on the Smith Chart, where the level of NMSE in the interpolation region remains - 39.8 dB. 95

5.1 Flow diagram summarizing the procedure used to establish the equivalence between ANN and CM coefficients. 100

5.2 Conventional CM model diagram. 102

5.3 Diagram of the CM model reformulated for Real and Imaginary parts. 105

5.4 Conventional ANN model diagram. 106

5.5 Conventional ANN model diagram in matrix format. 107

5.6 FCC ANN model diagram. 111

5.7 FCC ANN model diagram. 112

5.8 Reformulated FCC ANN model diagram. 114

5.9 Selected bias point (red markers) locations on the $\tanh(x)$ function. Location when 3^{rd} order derivative equals 0 (circle) and location when 2^{nd} order derivative equals 0 (triangle). 118

5.10 Flow diagram summarizing the proposed ANN determining method. . 122

5.11 $A_{2,1}$ sample (a) and its Fourier Transformed spectrum (b) on a trajectory computed using 229 simulated points with the phase modulation rate of Sp = 19. 123

5.12 $B_{2,1}$ sample (b) and its Fourier Transformed spectrum (a) with error bar (red) on the trajectory computation, and the expected exponents' $|A_{2,1}|^m(\angle A_{2,1})^n$ values of the CM for extracting coefficients in (n,m). . 123

5.13 The dataset coverage on the tanh(x) function range without the $3^{rd}/2^{nd}$ order segment (A-B) location after determined weights and biases. The Fourier Transformed spectrum comparison plot (C-D) of the modelled $B_{2,1}$(blue) and the $B_{2,1}$ samples from the simulation (red) and the calculated from the CM (orange) with error bar (red-line) on the trajectory computation. 125

5.14 The FCC ANN performance for $B_{2,1}$ prediction changing trend with ρ sweep from 0 to 3. 126

5.15 The $B_{2,1}$ prediction from the determined FCC ANN (blue stars) and the $B_{2,1}$ acquired from the simulation with complete data complexity (red circles) of the Wolfspeed device. 128

5.16 $B_{2,0}$ sample (a) and its Fourier Transformed spectrum (b) with error bar (red) on the trajectory computation, and the expected exponents' $|A_{2,1}|^m(\angle A_{2,1})^n$ values of the CM for extracting coefficients in (n,m). . 129

5.17 The $B_{2,0}$ prediction from the determined FCC ANN (blue stars) and the $B_{2,0}$ acquired from the simulation with complete data complexity (red circles) of the Wolfspeed device. 130

5.18 The predicted (blue) and simulated (black) output power comparison of the Wolfspeed device. 131

5.19 The predicted (blue) and simulated (black) efficiency contours comparison of the Wolfspeed device. 132

5.20 Selected $A_{2,1}$ samples (a) from the calculation (blue circles)and picked from measurement (red dots) and its Fourier Transformed spectrum comparison (b, calculated shown in red and measured shown in blue) on a trajectory computed using 229 simulated points. of the WIN device measurement 133

5.21 $B_{2,1}$ sample (a) and its Fourier Transformed spectrum (b) with - 60 dB error bar (red) on the trajectory computation, and the expected exponents' $|A_{2,1}|^m(\angle A_{2,1})^n$ values of the CM for extracting coefficients in (n,m) of the WIN device measurement. 133

5.22 The FCC ANN performance for $B_{2,1}$ prediction of the WIN device changing trend with ρ sweep from 0 to 3. 135

5.23 The $B_{2,1}$ prediction of the WIN device from the determined FCC ANN (blue stars) and the $B_{2,1}$ acquired from the measurement with the analyzed data complexity (red circles). 135

5.24 $B_{2,0}$ sample (a) and its Fourier Transformed spectrum (b) with -60 dB error bar (red) on the trajectory computation, and the expected exponents' $|A_{2,1}|^m(\angle A_{2,1})^n$ values of the CM for extracting coefficients in (n,m). 136

5.25 The $B_{2,0}$ prediction of the WIN device from the determined FCC ANN (blue stars) and the $B_{2,0}$ acquired from the measurement with the analyzed data complexity (red circles). 137

5.26 The predicted (blue) and measured (black) output power contours of the WIN device. 137

5.27 The predicted and measured efficiency contours of the WIN device. . 138

5.28 Comparison of CM (red) and ANN (blue) modelling of the output power contours of the WIN device. 139

5.29 Comparison of CM (red) and ANN (blue) modelling of the efficiency contours of the WIN device. 139

5.30 Modeled efficiency vs. output power for the WIN device models, including the extrapolation region. CM (red circles) and ANN (blue line). 140

List of Tables

2.1 Phase and magnitude exponent parameters corresponding to (2.16). . 21

2.2 Phase and magnitude exponent parameters corresponding to (2.17). . 21

3.1 The Extracted CM Coefficients For $B_{2,1}$ using CM with the conventional mixing theory 48

3.2 The Extracted CM Coefficients For $B_{2,1}$ with analysis on Tailored Dataset 51

4.1 The Extracted Coefficients Comparison For Simulated $B_{2,1}$ of the Wolfspeed Device Using Different Techniques 73

4.2 The Extracted Coefficients Comparison For Simulated $B_{2,0}$ of the Wolfspeed Device Using Different Techniques 75

4.3 The Extracted Cardiff Model Coefficients For Measured $B_{2,1}$ of the Wolfspeed Device Using Conventional CM Formulation 78

4.4 The Extracted Cardiff Model Coefficients For Measured $B_{2,1}$ of the Wolfspeed Device Using the invented ANN based Coefficient Extractor 79

4.5 The Extracted Cardiff Model Coefficients For Measured $B_{2,0}$ of the Wolfspeed Device Using Conventional CM Formulation 80

4.6 The Extracted Cardiff Model Coefficients For Measured $B_{2,0}$ of the Wolfspeed Device Using the invented ANN based Coefficient Extractor 80

4.7 The Extracted Coefficients Comparison For Measured $B_{2,1}$ of the Wolfspeed Device Using Different Methods 86

4.8 The Extracted Coefficients Comparison For Measured $B_{2,0}$ of the Wolfspeed Device Using Different Methods 88

4.9 The Extracted Coefficients For Measured $B_{2,0}$ of the WIN Device Using the Invented ANN Based Coefficient Extractor 90

4.10 The Extracted Cardiff Model Coefficients For Measured $B_{2,1}$ of the Wolfspeed Device Using the Combined Method 93

4.11 The Extracted CM Coefficients For Measured $B_{2,0}$ of the WIN Device Using the Combined Method 94

5.1 The Extracted CM Coefficients For $B_{2,1}$ of the Wolfspeed device . . . 124

5.2 The Extracted CM Coefficients For $B_{2,0}$ of the Wolfspeed device . . . 129

5.3 The Extracted CM Coefficients For $B_{2,1}$ of the WIN device measurement 134

5.4 The Extracted CM Coefficients For $B_{2,0}$ of the WIN device 136

Chapter 1

Introduction

With extensive uses of Radio Frequency (RF) and microwaves across wireless communication systems under different scenarios nowadays, there is an increasing demand for better power amplifiers (PAs) to drive the signals because of the reduced noise and distortion target: the longer transmission distances, the lower energy consumption and the heat generation expectations. Transistors are one of the essential components required to operate in the PA design process, with sufficient performance related to many desired targets.

Modelling transistors provides an efficient way to design RF/microwave power components and systems in a Computer-Aided Design (CAD) environment, especially when the technology is not established and so the relevant Process Design Kits (PDKs) are not available. Measurement systems are necessary to extract an accurate transistor model. Different data acquisition criteria are required, e.g., a sufficient number of data points in general or a high-density set when the measurement system is not precisely controllable for a selectable conditioned data pattern.

As the first step into the details of this work, this Chapter briefly illustrates the general development path of transistor behavioural modelling techniques for RF/microwave design. Secondly, it provides a description section of the correlated

load-pull measurement system setups. Then, it follows up with a section explaining the objective of this work. Finally, it concludes with a section of the chapter summary for guidance.

1.1 Transistor Models for RF/Microwave design

In general, based on the model extraction process, transistor models can be separated into three types: Physical models, compact models, and behavioural models. The three types of transistor models have their own application scenarios with strengths and weaknesses.

Both the physical and the compact model types incorporate aspects of the underlying device physics. The extracted models of these two model types are analytical sets of equations or derived coefficients, which can normally be mapped to physical equivalent features of the transistor. The physical models, which highly rely on the transistor design technology, are extracted and mainly used for assisting the fabrication process [1] with priority knowledge about the internal structure of transistors. This type of model can be applied to investigate the behaviour of transistors; however, it can be difficult and time-consuming to use for PA design [2], especially when the device is becoming more complex because of the application demand. Following the explanation given by [3], the compact models allow an accurate mathematical approximation from voltage to current. The directly extracted equations/coefficients of compact models provide a more efficient solution for CAD simulators compared to the physical models, hence occupying an important position in the circuit design process, as well as measurement system applications [4].

For the physical/compact model extraction, the pulsed bias, current/voltage (I/V), and S-parameter measurements are the general used to interpret the transistor characterisation. The pulsed measurement setups, using a Vector Network Analyser (VNA), provide a safe pulsed-IV measurement operation for the transistor at low

risk of damage, as well as coverage on the capacitive and inductive effects [5]. For succeeding in a pulsed model extraction, specific load-pull measurement system setups may be required for data acquisition and extracted model validation.

Different from the other two types of model categories, the behavioural models, also known as empirical models, do not completely rely on the physical parameters. Associated with proper measurement system setups, behavioural models can be divided into more precise divisions according to the level of non-linearity they deal with.

Beginning with linear S-parameter model for small signal conditions [6], the development of behavioural models then moves on to resolve non-linear problems under large signal conditions [7], [8]. By extending the S-parameter model, the Volterra Input Output Map (VIOMAP) [9] is the sequel solution for weak nonlinear to strong nonlinear systems. With similar approaches to the formulation variation, Hot S-parameters [10] are then introduced with the inclusion of a different measurement procedure [11]. The Poly-harmonic Distortion (PHD) modelling technique [12] is subsequently presented with the Hot S-parameter model as its basis. With the distortion effects from harmonics reflecting in a chain to the fundamental non-linear behaviour of the transistor [13], the PHD models then set up the mathematical framework for the Cardiff Model (CM) [14], [15] and the X-parameter [16] model. When there was an increased awareness of the power of Artificial Neural Networks (ANN), it has also been considered to be one of the techniques for generating behavioural models from the 1990s [17].

All types of behavioural models offer the possibility for model extraction without an understanding of the internal device/circuit structure, so can be used as black box models. This can be an advantage to the manufacturer since it can help protect the corresponding Intellectual Property (IP), and be easily utilised for designers in CAD environment [13].

In this work, the behavioural model type is investigated in detail, especially with the CM and the ANN technique, to acquire more efficient models that can enable the direct use of measurement datasets in non-linear RF systems, for the reasons (will be later detailed and illustrated in the literature review) that the CM provides a physics-based mathematically formulated non-linear model, and the ANN technique allows flexible and robust behavioural models.

1.2 Measurement Systems

As mentioned in the previous section, diverse transistor models can be extracted using different measurement setups. Specific measurement category can allow necessary dataset acquisition. The selection of the measurement systems is notable for the model generation procedure. The load-pull measurement can be utilised not only for pulsed model validation but also for large signal behavioural model extraction.

The architecture of the load-pull measurement systems can vary according to specific modelling/design requirements. A general structure diagram is shown in Fig. 1.1.

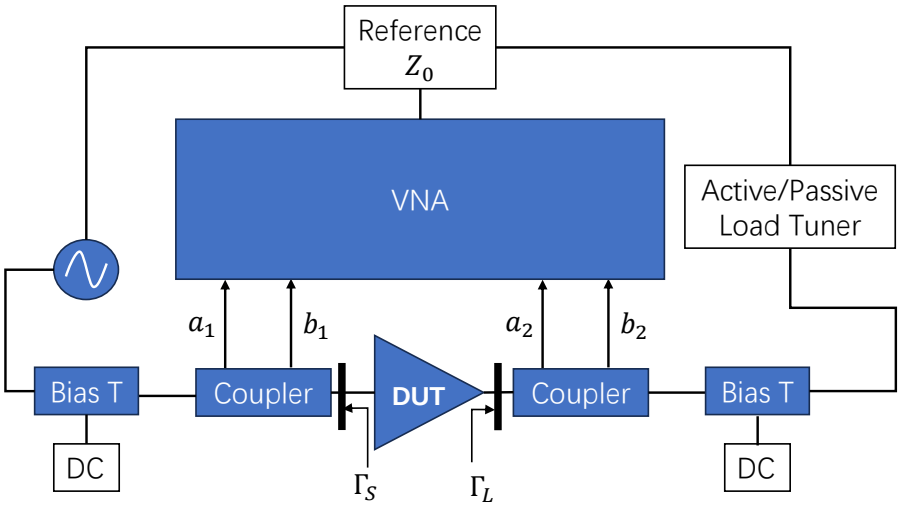

Figure 1.1: Generic Load-Pull Setup Diagram with Device Under Test (DUT)

In assisting the large signal behavioural model, two types of load-pull measurement can be done: a passive load-pull measurement with the load tuner; and an ac-

tive load-pull measurement with a power amplifier controlling the incident signal to the output of the device [18]. Passive load-pull measurements can enable a speedy measurement operation, however, they have the drawback of a slower calibration procedure due to the slow movement of mechanical tuners needed for load termination, especially for high power applications. Though an active setup sometimes requires strong power amplifiers, it provides the possibility for measurements to cover a bigger Γ_L range over the Smith Chart [19] and a faster calibration. Therefore, the active load-pull is more commonly engaged for high reflection coefficient situations, especially when reflection coefficients are required to be matched at the short/open edge of the Smith Chart [19].

The active load-pull measurement injects pseudo Continuous Wave (CW), a_1 and a_2, response with harmonically related response reflected waves b_1 and b_2 correlating to the topology in Fig.1.1. The large signal measurement allows the a/b waves to be converted/calculated from the current/voltage (I/V) signals with the following equations [14], [20]:

$$V = \frac{Z_0^* a + Z_0 b}{\sqrt{\Re(Z_0)}} \tag{1.1}$$

$$I = \frac{a - b}{\sqrt{\Re(Z_0)}} \tag{1.2}$$

$$a = \frac{V + Z_0 I}{2\sqrt{\Re(Z_0)}} \tag{1.3}$$

$$b = \frac{V - Z_0^* I}{2\sqrt{\Re(Z_0)}} \tag{1.4}$$

where Z_0 is the reference impedance shown in Fig.1.1, the default value commonly chosen to be $50\,\Omega$ [21].

The measured scattered waves allow the transistor behaviour to be captured in

the frequency domain, with a fixed input drive level defined by component a_1 at fundamental, hence $a_{1,1}$. Considering the harmonic impacts, a generic formulation set can be listed [21], as the basis for large signal transistor modelling technique:

$$b_{p,h} = F\left(a_{p,h}\right) \tag{1.5}$$

where 'p' and 'h' represent the port number and harmonic index, respectively.

In the pursuit of the requirement of an efficient and low-cost design procedure in CAD environment, such as the Simulation Program with Integrated Circuit Emphasis (SPICE) [22] package, the Applied Wave Research (AWR) Microwave Office [23], and the Keysight Advanced Design System (ADS) [24], simulation of measurements is also a capability. One CAD implementation example in ADS [24] is shown as Fig. 1.2.

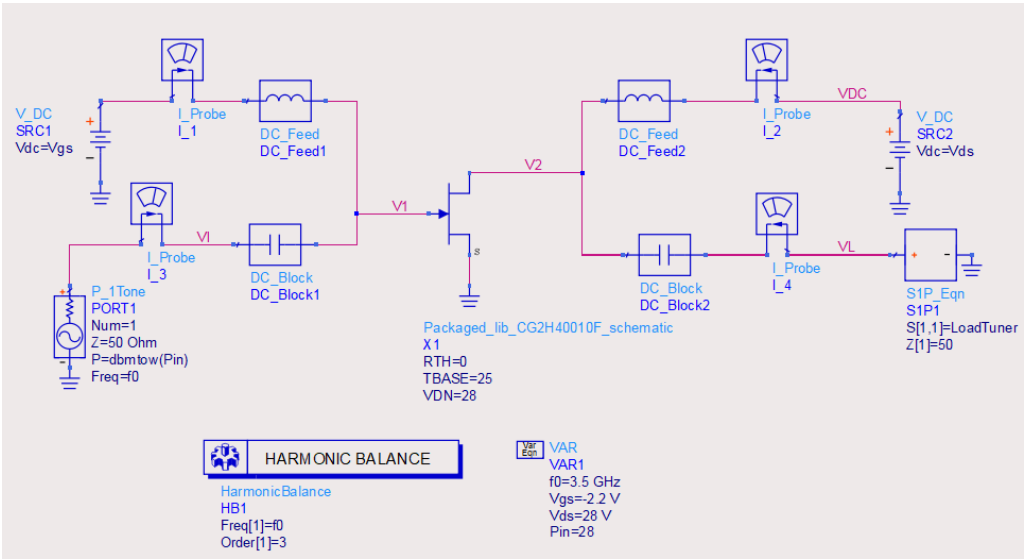

Figure 1.2: load-pull setup in ADS

The '*S1P_Eqn*' block, in Fig.1.2, is used based on parameter sweeps to create load grids in circular or rectangular patterns. The DUT in the middle can be replaced with model implementation through a Frequency-domain Defined Device (FDD) component block for model validation.

1.3 Thesis Objective

Under the present scenario of the RF/microwave CAD design environment, when developing or extracting non-linear behavioural models for transistors, the key concern commonly focuses on shortening the computation time, while simultaneously keeping the model robustness [25]. A speedy modelling procedure with robust predicting ability can save time, and prevent an optimizer converging on an erroneous load point when trying to optimize the matching networks. In this work, the Cardiff Model (CM) and Artificial Neural Network (ANN) based model are selected to be explored for a possible improvement to current modelling solutions that support the designers better.

The CM has been developed and utilised as a reliable behavioural model in CAD over the past few decades. It is commercially widely used based on the fact that it can be extracted regardless of the specific measurement system [11]. The ANN technique has the robustness and efficient modelling capability for complex nonlinear problems, hence, as a reason to be chosen for investigation. In addition, the ANN allows flexible model parameter variation to achieve different types of model performance, irrespective of specific measurement datasets.

Both models are proven accurate within the measurement-referenced region, representing an accurate interpolation ability. However, not much work has been done on engaging the trade-off between interpolation accuracy and extrapolation ability. The objective of this work is to identify potential problems when using the CM and ANN approaches, focusing on the extrapolation robustness of both models, and looking into the practicability of combining the two modelling frameworks, or operating one to help boost the other model for an optimised model extraction process.

1.4 Chapter Summary

Given the thesis objective in the previous section, the thesis is arranged as follows, towards the achievement of the target.

In Chapter 2, the literature review on the CM and the ANN is provided. The development history of both the CM and ANN will be illustrated, with a brief conclusion of the basic formulation of other mainstream modelling techniques. The associating structure categories, parameters and training algorithms to the ANN will also be introduced. In addition, the implementation platform together with the present application discussion will be given to the two models, respectively.

In Chapter 3, a comparison is made on the current existing CM and ANN structure. An ADS load-pull simulation is set up for data acquisition. The extrapolation ability of the two modelling techniques will be compared in detail. In this investigation, different ANN structure performance is also looked inside and compared for future evidence. A conclusion will be proposed as hints into the next step for establishing a novel model procedure with improved characteristics.

In Chapter 4, a novel CM coefficients extracting process assisted by the ANN technique is invented. By modifying the Levernberg-Maquart training algorithm to the ANN model, the CM coefficients can be varied, for a more reasonable extrapolation predicting ability compared to the conventional mixing theory.

In Chapter 5, an alternative ANN determining method is proposed. With the Taylor series approximation analysis, both the CM and selected ANN structure can be reformulated for a matching topology. A set of equations that allows an accurate ANN structure to be defined from the CM coefficients is established.

Finally, in Chapter 6, the conclusion of this work is delivered, followed by a discussion about the potential future work coming out of this thesis.

References

[1] M. Golio, L. Dunleavy, T. Gneiting, "History and state-of-the-art in large signal modeling for RF/microwave power amplifier development," in *2015 IEEE MTT-S International Microwave Symposium*, Phoenix, AZ, USA, May 2015, pp. 1–4. DOI: 10.1109/MWSYM.2015.7166756.

[2] P.H. Aaen, J.A. Plá, J. Wood, *Modeling and characterization of RF and microwave power FETs* (The Cambridge RF and microwave engineering series), eng. Cambridge: Cambridge University Press, 2007, ISBN: 9780511541124.

[3] W.R. Curtice, "A MESFET Model for Use in the Design of GaAs Integrated Circuits," eng, *IEEE transactions on microwave theory and techniques*, vol. 28, no. 5, pp. 448–456, May 1980, ISSN: 0018-9480.

[4] M. Koh, "Geometric and frequency scalable transistor behavioural model for MMIC design," Available at https://orca.cardiff.ac.uk/id/eprint/93365/, Ph.D. dissertation, School of Engineering, Cardiff University, Cardiff, UK, 2016.

[5] Groote, F. D., J.-P. Teyssier, T. Gasseling, J. Verspecht, O. J., "Introduction to measurements for power transistor characterization," *IEEE Microwave Magazine*, vol. 9, no. 3, pp. 70–85, Jun. 2008. DOI: 10.1109/MMM.2008.919928.

[6] A. Khusro, S. Husain, M.S. Hashmi, A.Q. Ansari, "Small signal behavioral modeling technique of GaN high electron mobility transistor using artificial neural network: An accurate, fast, and reliable approach," *International Journal of RF and Microwave Computer-Aided Engineering*, vol. 30, no. 4, e22112, Apr. 2020. DOI: https://doi.org/10.1002/mmce.22112.

[7] S.R. Mazumder, Puije, P. v., "Two-Signal Method of Measuring the Large-Signal S-Parameters of Transistors," *IEEE Transactions on Microwave Theory and Techniques*, vol. 26, no. 6, pp. 417–420, Jun. 1978. DOI: 10.1109/TMTT.1978.1129404.

[8] T. Gasseling, D. Barataud, S. Mons, "Hot small-signal S-parameter measurements of power transistors operating under large-signal conditions in a load-pull environment for the study of nonlinear parametric interactions," *IEEE Transactions on Microwave Theory and Techniques*, vol. 52, no. 3, pp. 805–812, Mar. 2004. DOI: 10.1109/TMTT.2004.823528.

[9] F. Verbeyst, V. Bossche, "VIOMAP, the S-parameter equivalent for weakly nonlinear RF and microwave devices," eng, *IEEE transactions on microwave theory and techniques*, vol. 42, no. 12, pp. 2531–2535, Dec. 1994, ISSN: 0018-9480.

[10] J. Verspecht, D. Barataud, J.-P. Teyssier, J.-M. Nebus, "Hot S-parameter techniques: 6 = 4 + 2," eng, in *2005 66th ARFTG Microwave Measurement Conference (ARFTG)*, Washington, DC, USA: IEEE, Dec. 2005, pp. 1–9, ISBN: 1538672928.

[11] J. Bell, "Input harmonic and mixing behavioral model analysis," Available at `https://orca.cardiff.ac.uk/id/eprint/64151/`, Ph.D. dissertation, School of Engineering, Cardiff University, Cardiff, UK, 2014.

[12] D.E. Root, J. Verspecht, D. Sharrit, J. Wood, A. Cognata, "Broad-band poly-harmonic distortion (PHD) behavioral models from fast automated simulations and large-signal vectorial network measurements," *IEEE Transactions on Microwave Theory and Techniques*, vol. 53, no. 11, pp. 3656–3664, Nov. 2005. DOI: `10.1109/TMTT.2005.855728`.

[13] J. Verspecht, D.E. Root, "Polyharmonic distortion modeling," *IEEE Microwave Magazine*, vol. 7, no. 3, pp. 44–57, Jun. 2006. DOI: `10.1109/MMW.2006.1638289`.

[14] H. Qi, J. Benedikt, P. Tasker, "A Novel Approach for Effective Import of Nonlinear Device Characteristics into CAD for Large Signal Power Amplifier Design," in *2006 IEEE MTT-S International Microwave Symposium Digest*, San Francisco, CA, USA, Jun. 2006, pp. 477–480. DOI: `10.1109/MWSYM.2006.249596`.

[15] P.J. Tasker, J. Benedikt, "Waveform Inspired Models and the Harmonic Balance Emulator," *IEEE Microwave Magazine*, vol. 12, no. 2, pp. 38–54, Apr. 2011. DOI: `10.1109/MMM.2010.940101`.

[16] D.E. Root, J. Verspecht, J. Horn, M. Marcu, *X-parameters : characterization, modeling, and design of nonlinear RF and microwave components* (The Cambridge RF and microwave engineering series), eng. Cambridge: Cambridge University Press, 2013, ISBN: 9780521193238.

[17] W. Fang, Q.J. Zhang, "Knowledge based neural models for microwave design," in *1997 IEEE MTT-S International Microwave Symposium Digest*, vol. 2, Denver, CO, USA, Jun. 1997, 627–630 vol.2. DOI: `10.1109/MWSYM.1997.602870`.

[18] F. Deshours, E. Bergeault, F. Blache, J.-P. Villotte, B. Villeforceix, "Experimental comparison of load-pull measurement systems for nonlinear power transistor characterization," *IEEE Transactions on Instrumentation and Measurement*, vol. 46, no. 6, pp. 1251–1255, Dec. 1997. DOI: 10.1109/19.668266.

[19] M.S. Hashmi, F.M. Ghannouchi, "Introduction to load-pull systems and their applications," *IEEE Instrumentation & Measurement Magazine*, vol. 16, no. 1, pp. 30–36, Feb. 2013. DOI: 10.1109/MIM.2013.6417055.

[20] P.J. Tasker, "Practical waveform engineering," *IEEE Microwave Magazine*, vol. 10, no. 7, pp. 65–76, Dec. 2009. DOI: 10.1109/MMM.2009.934518.

[21] J. Wood, D.E. Root, *Fundamentals of nonlinear behavioral modeling for RF and microwave design* (Artech House microwave library), eng. Boston, Mass. ; Artech House, 2005, ISBN: 9781580537759.

[22] L.W. Nagel, D.O. Pederson, "SPICE (Simulation Program with Integrated Circuit Emphasis)," EECS Department, University of California, Berkeley, Tech. Rep. UCB/ERL M382, Apr. 1973. [Online]. Available: http://www2.eecs.berkeley.edu/Pubs/TechRpts/1973/22871.html.

[23] Office, C. A. M. "AWR Microwave Office Datasheet." (), [Online]. Available: https://www.cadence.com/content/dam/cadence-www/global/en_US/documents/tools/system-analysis/rf-microwave-design/AWR_microwave_office_ds.pdf.

[24] Technologies, K. "Advanced Load Pull DesignGuide." (), [Online]. Available: https://docs.keysight.com/eesofkcads/advanced-load-pull-designguide-645666571.html.

[25] D.E. Root, "Future Device Modeling Trends," *IEEE Microwave Magazine*, vol. 13, no. 7, pp. 45–59, Nov. 2012. DOI: 10.1109/MMM.2012.2216095.

Chapter 2

Literature Review

Modelling techniques can be considerably useful in the Computer-Aided Design (CAD) environment and have been significant to the Radio Frequency (RF) design tasks for reducing time and costs during the prototyping optimisation process. Amongst the transistor modelling categories, there are a variety of large-signal models for High-Electron-Mobility transistors (HEMTs).

Based on transistor physics in the time domain, current-voltage (I-V), and charge-voltage (Q-V), compact models have been applied to measurement systems as industrial standards. Using user-defined closed form mathematical, empirical equations, the Angelov Model [1] for HEMT transistor is one of the examples that forms the basis, from which the modifications for improvements have been made on better model scalability and enhanced model robustness in the recent decade, [2], [3]. Other examples, including the MIT Virtual Source GaN-HEMT (MVSG) [4], the EEHEMT Model [5], and the Advanced Spice Model (ASM) HEMT [6] were also introduced to enable robust circuit simulation with physics-based models. Aside from the mathematical model expressions, the Look Up Table (LUT) type of compact model is also widely utilized, with the Root model [7], [8] as one of the examples.

The scattered wave formalism (related to equations (1.1)-(1.4)) allows nonlinear

behavioural modelling in the frequency domain. This type of transistor model starts by capturing the linear behaviour with S-parameters. Moving on to capturing more complex transistor behaviour, the Volterra Input Output Map (VIOMAP) [9], Hot S-parameters [10] and the Poly-Harmonic Distortion (PHD) Model [11], X-parameters [12] and the Cardiff Model (CM) [13], [14]. Artificial Neural Network (ANN) technique based models [15]–[18] were also been well-developed and widely applied to RF designs [19]–[23].

A robust compact model involves internal device structure, coupled with complex parameter extraction procedures from measurement that may require a long runtime. On the contrary, the behavioural models can be extracted directly and applied to the commercial simulator as a black box. Therefore, the behavioural models can be selected to keep up with the fast-paced changes of emerging device technologies. This Chapter will introduce, firstly, the development of the non-linear transistor behavioural models in general. Since this work aims to combine the CM and the ANN technique based on their benefits and drawbacks, in this Chapter, the theory and the application status of the CM and the ANN will be reviewed in detail.

2.1 Development of Behavioural Models

Scattering parameters [17], also called the S-parameters, form the basis of the behavioural models. It utilises the concept of pseudo Continuous Wave (CW) a/b waves. As mentioned in the previous chapter Fig. 1.1 with the two-port load-pull measurement system, the mathematical relationship between the measured S-parameters is shown in Fig. 2.1. The theoretical formulations are listed as (2.1a)-(2.1b).

$$b_1 = S_{11}a_1 + S_{12}a_2 \tag{2.1a}$$

$$b_2 = S_{21}a_1 + S_{22}a_2 \tag{2.1b}$$

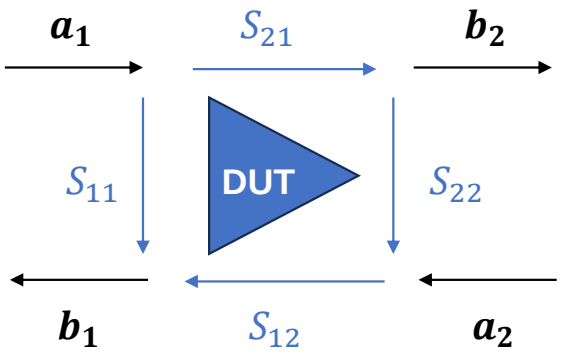

Figure 2.1: S-parameters diagram with DUT

where in (2.1a) and (2.1b), 'a_1', 'a_2', 'b_1', and 'b_2' can be calculated with (1.3) - (1.4) from current/voltage (I/V) measurements.

The S-parameters allow accurate modelling results under linear conditions. However, when a device is operated near/close to saturation under large signal conditions, its performance behaves with more non-linear features. Under this scenario, the conventional S-parameter model is no longer robust enough to capture all non-linear device behaviours. Sets of nonlinear transistor models were then introduced in an order that follows an approximate development timeline, including the Volterra Input Output Map (VIOMAP) [9], [24] model, Hot S-parameters [10], and the Poly-Harmonic Distortion (PHD) Model [11].

By extending the S-parameter model, the VIOMAP model moves from capturing linear device behaviours towards non-linear behaviours. According to the description in [9], [24], the VIOMAP kernel $H_{n,ji_1,i_2...i_n}(f_1, f_2, ..., f_n)$ describes the n_{th} degree of nonlinearity of system 'H' as the setup in Fig. 2.2, equivalent to the 'DUT' as in Fig. 2.1. Here, the frequencies 'f_n' are combined at input terminal 'i_n' into the frequency component '$f_l + f_2 + ... + f_n$' of the output signal at output terminal 'j' [24].

The correlated Volterra formulation is identical to the S-parameter model at the linear level. When incorporating third-order non-linearity generated by a device, the formulations are as follows:

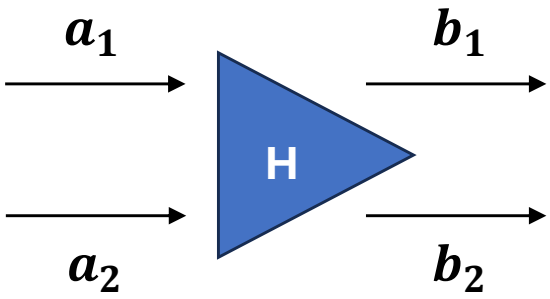

Figure 2.2: The VIOMAP system diagram

$$
\begin{aligned}
b_1(1) =& H_{1,11}(1)a_1(1) \\
&+ H_{1,12}(1)a_2(1) \\
&+ 3H_{3,1111}(1,1,-1)a_1(1)a_1(1)a_1(-1) \\
&+ 3H_{3,1112}(1,1,-1)a_1(1)a_1(1)a_2(-1) \\
&+ 6H_{3,1112}(1,-1,1)a_1(1)a_1(-1)a_2(1) \\
&+ 6H_{3,1122}(1,1,-1)a_1(1)a_2(1)a_2(-1) \\
&+ 3H_{3,1122}(-1,1,1)a_1(-1)a_2(1)a_2(1) \\
&+ 3H_{3,1222}(1,1,-1)a_2(1)a_2(1)a_2(-1)
\end{aligned}
\tag{2.2}
$$

$$
\begin{aligned}
b_1(3) =& H_{3,1111}(1,1,1)a_1(1)a_1(1)a_1(1) \\
&+ 3H_{3,1112}(1,1,1)a_1(1)a_1(1)a_2(1) \\
&+ 3H_{3,1122}(1,1,1)a_1(1)a_2(1)a_2(1) \\
&+ H_{3,1222}(1,1,1)a_2(1)a_2(1)a_2(1)
\end{aligned}
\tag{2.3}
$$

The VIOMAP kernel that relates the a/b waves from the load-pull measurement system will require computing assistant software when a higher polynomial order is required in the model equations, as the device behaviour will obtain higher nonlinearity. Accurately applying VIOMAP is challenging. Hence, it lacks user-friendliness.

Simpler than the VIOMAP kernel theory, the Hot S-parameter model is proposed

with a similar formulation framework to conventional S-parameters. Originally in [25], the Hot S-parameter model is formulated with (2.4).

$$\begin{bmatrix} b_1(f) \\ b_2(f) \end{bmatrix} = \begin{bmatrix} HotS_{11}(f) & HotS_{12}(f) \\ HotS_{21}(f) & HotS_{22}(f) \end{bmatrix} \begin{bmatrix} a_1(f) \\ a_2(f) \end{bmatrix} \tag{2.4}$$

At this stage, the '[***Hot-S***]' parameter matrix depends on the power level, fundamental and harmonic frequencies, and other intermodulation products related to device operating point [25].

Later in (2.5), it is 'f_c' that differs the '[***Hot-S***]' parameter matrix from the conventional '[***S***]' parameters. The large signal variable '$a_1(f_c)$' has an amplitude and frequency that is not perfectly linear anymore [26]. For the consideration of stability, related research work shows that Hot S-parameters, under the large signal domain to deal with non-linear transistor behaviours corresponding to at least 1 dB compression operating condition, is then extended as (2.5) [26].

$$\begin{bmatrix} b_1(f_c) \\ b_2(f_c) \end{bmatrix} = \begin{bmatrix} HotS_{11} & HotS_{12} \\ HotS_{21} & HotS_{22} \end{bmatrix} \begin{bmatrix} a_1(f_c) \\ a_2(f_c) \end{bmatrix} + \begin{bmatrix} T_{12}(f_c) \\ T_{22}(f_c) \end{bmatrix} e^{j2\varphi(a_1(f_c))} \mathrm{conj}(a_2(f_c)) \tag{2.5}$$

here in (2.5), f_c is the large signal carrier frequency that always appears in the injected signal a_1. Extra [$\boldsymbol{T}$] terms were derived from mixer theory [26].

However, the Hot S-parameter system stability is sensitive to the harmonic frequencies from the load-pull measurement [27]. This then directs towards the requirement of preliminary analysis and specific measurement system setup for a set of accurate Hot S-parameters extraction.

The Poly-Harmonic Distortion (PHD) model, proposed in [11], [28], also works with the travelling waves similar to the S-parameters. Different from the Hot S-parameters, the PHD model does not rely on special/complex load-pull measurement system setup. With (2.6), the PHD model is defined to capture the non-linear

transistor behaviour with the input and output of the Device Under Test (DUT), related directly with the mathematical equation.

$$B_{pm} = \sum_{qn} S_{pq,mn}\left(|A_{11}|\right) P^{+m-n} A_{qn} + \sum_{qn} T_{pq,mn}\left(|A_{11}|\right) P^{+m+n} \mathrm{conj}\left(A_{qn}\right) \tag{2.6}$$

where

$$K_{pm}(|A_{11}|) = F_{pm}(|A_{11}|, 0, ...0) \tag{2.7}$$

$$G_{pq,mn}(|A_{11}|) = \left.\frac{F_{pm}}{\mathrm{Re}(A_{qn}P^{-n})}\right|_{|A_{11}|,0,...0} \tag{2.8}$$

$$H_{pq,mn}(|A_{11}|) = \left.\frac{F_{pm}}{\mathrm{Im}(A_{qn}P^{-n})}\right|_{|A_{11}|,0,...0} \tag{2.9}$$

$$\begin{aligned} &S_{P1,M1}(|A_{11}|) = \frac{K_{pm}(|A_{11}|)}{|A_{11}|} \\ &\forall\{q,n\} \neq \{1,1\} : S_{pq,mn}(|A_{11}|) = \frac{G_{pq,mn}(|A_{11}|) - jH_{pq,mn}(|A_{11}|)}{2} \end{aligned} \tag{2.10}$$

$$\begin{aligned} &T_{P1,M1}(|A_{11}|) = 0 \\ &\forall\{q,n\} \neq \{1,1\} : T_{pq,mn}(|A_{11}|) = \frac{G_{pq,mn}(|A_{11}|) + jH_{pq,mn}(|A_{11}|)}{2} \end{aligned} \tag{2.11}$$

with phasor 'P' being defined as:

$$P = e^{+j\varphi(A_{11})} \tag{2.12}$$

and 'q' and 'p' represent the signal port numbers, 'm' and 'n' represent harmonic index.

The PHD model is accurate not only for capturing the non-linear characteristics with the acquired data from the load-pull measurement system, but also extends to other aspects, such as harmonics, compression, AM-PM, and time domain waveforms [29].

In recent decades, the PHD model, with its commercial format as the X-parameters, and the Cardiff Model (CM), which is formulated with the PHD model as the basis,

have all been widely applied to RF design-related hardware and software. Considering the X-parameter processing procedure may rely on large data files since multiple parameter terms '$S_{qp,mn}$' and '$T_{qp,mn}$' correlated to '$K_{q,m}$', '$G_{qp,mn}$' and '$H_{qp,mn}$' are required, the CM is thought to be more efficient in this work. It requires reduced file size by directly extracting equivalent behavioural formulations from the measurement dataset with only one set of coefficient term '$M_{p,h,m,n}$' in the polynomial format. Details for the CM coefficient extraction follow.

2.2 The Cardiff Model (CM)

The CM was first formulated with a Direct Waveform Look-Up Table (DWLU) approach and then a behavioural model as mentioned in [13], [30]–[33]. In 2006, the model was proposed for a better model performance when considering the load impedance [30], compared to the S- and T-parameters proposed in [11].

With the DWLU approach following the given diagram in Fig. 2.3 and equations (2.13)-(2.14), the load impedance corresponding a_n and b_n travelling waves are able to be searched by the simulator through the measurement data [30].

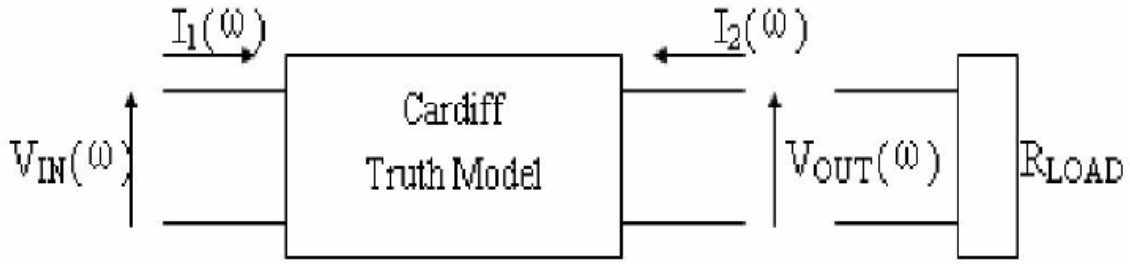

Figure 2.3: Definition of the truth model in frequency domain

$$I_1(\omega) = a_0\delta(\omega) + \sum_{n=1}^{h} a_h V_{IN}^h(\omega)\delta(\omega - 2\pi h f_0) \tag{2.13}$$

$$I_2(\omega) = b_0\delta(\omega) + \sum_{n=1}^{h} b_h V_{IN}^h(\omega)\delta(\omega - 2\pi h f_0) \tag{2.14}$$

where 'n' is the harmonic order index, the V_{IN} is the input CW stimulus, 'f_0' the fundamental frequency. 'a_0' and 'b_0' are the DC components.

The CM DWLU approach, provides a direct link between the measurement system and CAD environment and has been proven to be accurate within the covered measurement space. Thereafter, for a further easier and quicker analysis process, and to ensure the model can be shared simply, the DWLU approach was then developed in a polynomial mathematical formulation expansion [32].

2.2.1 The Polynomial Formulation of the CM

The CM, extracted directly from the DWLU approach in the polynomial expansion format, uses the PHD model as its basis [31]. It provides a robust formulation that can describe the transistor behaviour in response to load-pull measurement. When implemented in CAD tools, the CM is dealing with the device input and output relationship of the frequency relative phase and magnitude matrix elements, with the dataset extracted directly from load-pull measurements [13].

The expansion is formed based on the application of signal mixing with a least-square fit to measurement datasets [14]. Consider the case of modelling fundamental load-pull measurements performed on a two-port non-linear network such as the S-parameter system in 2.1. Two injected Continuous Waveform (CW) pseudo travelling-wave components $A_{1,1}$ and $A_{2,1}$ are used to compute the output frequency related components $B_{p,h}$ algebraically [14]. The output components, $B_{p,h}$, are a mixing sum of elements based on the phase and the magnitude grid that is related to the injected signals. Followed by a user-defined model order, the conventional mixing product and conjugation rules can be used as the reference to truncate the polynomial expansion of the model formulation [34].

The general CM formulation can be shown as below:

$$B_{p,h}\left(|A_{1,1}|\right) = Q_{1,1}^{h}\left(\sum_{r=0}^{r=\frac{(ord-h)}{2}}\sum_{n=-\left(\frac{(ord-h)}{2}-r\right)}^{n=h+\frac{(ord-h)}{2}-r} M_{p,h,m,n}\left(|A_{1,1}|\right)|A_{2,1}|^{m}\left(\frac{Q_{2,1}}{Q_{1,1}}\right)^{n}\right) \tag{2.15}$$

Here in (2.15), 'M' is the symbol of the CM coefficients, 'p' and 'h' represent the port number and harmonic order respectively. The correlated 'Q' parameters, $Q_{2,1}$ and $Q_{1,1}$, are the complex exponential of the phase of $A_{2,1}$ and $A_{1,1}$, and the 'n' and 'm' terms represent the phase and magnitude exponent parameters, respectively.

In general, the phase exponent parameter 'n' can range from $-\infty$ to $+\infty$, and the magnitude exponent parameter 'm' can range from 0 to $+\infty$. However, the values are constrained for the model accuracy in (2.15).

Following the analysis given in [13], the CM DWLU formulation (2.13) and (2.14) can be rearranged as the PHD model theory with (2.16) and (2.17) to the 3^{rd} order expansion.

$$b_1 = Q_{11}\left(T_{12}|a_2|\Phi^{-1} + S_{11}|a_1| + S_{12}|a_2|\Phi + T_{11}|a_1|\Phi^{2}\right) \tag{2.16}$$

$$b_2 = Q_{11}\left(T_{22}|a_2|\Phi^{-1} + S_{21}|a_1| + S_{22}|a_2|\Phi + T_{21}|a_1|\Phi^{2}\right) \tag{2.17}$$

where:

$$\Phi = e^{j(\angle a_{21} - \angle a_{11})} = \frac{Q_{21}}{Q_{11}} \tag{2.18}$$

$$S_{p,h}|a_h| = \frac{1}{n}\sum b_p \frac{1}{Q_{p,1}} \tag{2.19}$$

$$T_{p,h}|a_h| = \frac{1}{n}\sum b_p \frac{Q_{h,1}}{Q_{p,1}^{2}} \tag{2.20}$$

From (2.16) and (2.17), values that are assigned to the phase and magnitude expo-

nent parameters can be summarised and listed in Table 2.1, Table 2.2, and extended to the 5^{th} and 7^{th} order. These tables indicate the interaction of incident waves within a non-linear device and demonstrate the different patterns when analysing a bi-variate mixing process, as in [35].

Table 2.1: Phase and magnitude exponent parameters corresponding to (2.16).

	Φ^{-6}	Φ^{-5}	Φ^{-4}	Φ^{-3}	Φ^{-2}	Φ^{-1}	Φ^{0}	Φ^{1}	Φ^{2}	Φ^{3}	Φ^{4}	Φ^{5}	Φ^{6}	Φ^{7}
$\lvert a_{21}\rvert^0$							1^{st}							
$\lvert a_{21}\rvert^1$						3^{rd}		1^{st}						
$\lvert a_{21}\rvert^2$					3^{rd}		3^{rd}		3^{rd}					
$\lvert a_{21}\rvert^3$				5^{th}		3^{rd}		3^{rd}		3^{rd}				
$\lvert a_{21}\rvert^4$			5^{th}		5^{th}		5^{th}		5^{th}		5^{th}			
$\lvert a_{21}\rvert^5$		7^{th}		5^{th}		5^{th}		5^{th}		5^{th}		5^{th}		
$\lvert a_{21}\rvert^6$	7^{th}		7^{th}		7^{th}		7^{th}		7^{th}		7^{th}		7^{th}	
$\lvert a_{21}\rvert^7$		7^{th}		7^{th}		7^{th}		7^{th}		7^{th}		7^{th}		7^{th}

Table 2.2: Phase and magnitude exponent parameters corresponding to (2.17).

	Φ^{-3}	Φ^{-2}	Φ^{-1}	Φ^{0}	Φ^{1}	Φ^{2}	Φ^{3}	Φ^{4}
$\lvert a_{21}\rvert^0$				1^{st}				
$\lvert a_{21}\rvert^1$			3^{rd}		1^{st}			
$\lvert a_{21}\rvert^2$		5^{th}		3^{rd}		3^{rd}		
$\lvert a_{21}\rvert^3$	7^{th}		5^{th}		3^{rd}		5^{th}	
$\lvert a_{21}\rvert^4$		7^{th}		5^{th}		5^{th}		7^{th}
$\lvert a_{21}\rvert^5$			7^{th}		5^{th}		7^{th}	
$\lvert a_{21}\rvert^6$				7^{th}		7^{th}		
$\lvert a_{21}\rvert^7$					7^{th}			

In [32], [36], the two equations (2.16) and (2.17) are combined and generalized to give:

$$b_p = \sum_{m=0}^{\frac{n-1}{2}} C_{p,m} \left(\frac{Q_{21}}{Q_{11}}\right)^m a_1 + \sum_{m=0}^{\frac{n-1}{2}} U_{p,m} \left(\frac{Q_{11}}{Q_{21}}\right)^m a_2 \tag{2.21}$$

where: 'n' represents the polynomial order, 'C' and 'U' are the common factors related to the magnitude and phase of 'a_1' and 'a_2' extracted from (2.16) and (2.17). Then extended including the harmonic factor as:

$$b_{p,h} = Q_{11}^h \sum_{n=\frac{-(ord-1)}{2}}^{n=\frac{ord+1}{2}} K_{p,h,n} \left(\frac{Q_{21}}{Q_{11}}\right)^n \tag{2.22}$$

where

$$K_{p,h,n} = \sum_{m=0}^{m=q} M_{p,h,n,m} |a_{21}|^m \tag{2.23}$$

Based on the mixing theory and the least squared approximation, the parameters are better defined in [14]: the phase exponent parameter 'n', which can then be defined with the mixing order '*ord*' and the harmonic 'h', ranges from $-\left(\frac{(ord-h)}{2} - r\right)$ to $h + \left(\frac{(ord-h)}{2} - r\right)$. The magnitude exponent parameter 'm' is given by $m = |n| + 2r$ where 'r' is the magnitude restricting terms that can range from 0 to $\frac{(ord-h)}{2}$ for (2.15).

The coefficients $M_{p,h,m,n}$ of the CM can be extracted from the measured datasets using least-squared approximation.

$$[M_{p,h,m,n}] = \left(\left[|A_{2,1}|^m \left(\frac{Q_{2,1}}{Q_{1,1}} \right) \right]^H \left[|A_{2,1}|^m \left(\frac{Q_{2,1}}{Q_{1,1}} \right)^n \right] \right)^{-1} \left[|A_{2,1}|^m \left(\frac{Q_{2,1}}{Q_{1,1}} \right)^n \right]^H [B_{p,h}] \tag{2.24}$$

In specific cases when the dataset is pre-normalised to the complex exponential of the phase of $A_{1,1}$, the formula can be simplified as follows:

$$B_{p,h} = \left(\sum_{0}^{r} \sum_{n=-\left(\frac{(ord-h)}{2} - r\right)}^{n=h+\frac{(ord-h)}{2}-r} M_{p,h,m,n} |A_{2,1}|^m \left(Q_{2,1}\right)^n \right) \tag{2.25}$$

The formulation to extract the coefficients $M_{p,h,m,n}$ will then be:

$$[M_{p,h,m,n}] = \left([\mathbf{A}]^H [\mathbf{A}] \right)^{-1} [\mathbf{A}]^H [B_{p,h}] \tag{2.26}$$

where $[\mathbf{A}]$ is the A-matrix '$|A_{2,1}|^m \left(Q_{2,1}\right)^n$' populate with the (m, n) exponent pairs corresponding to the complex exponential of the magnitude and phase of $A_{2,1}$.

From the definition of the CM in (2.15), the population of the (m, n) exponent pairs is correlated to the mixing order, which needs to be determined by the user in advance. The user-defined model order, which will define the necessary model

complexity, is the key to a proper range of the 'm' and 'n' values. For a practical and accurate CM, the order has to be robustly identified linking with the measurement dataset, which was done through iteration at the beginning of the CM generation.

2.2.2 CM Extraction with Tailored Datasets

Earlier work in [13], [37] applied a repeating parameter sweep process to search for an appropriate model order from the value of 'n' to 'm'. To overcome the challenge and the duplicating process of ensuring a robust CAD implementation of the CM order, the spectrum analysis method in [34] was a recent development, which offers a direct approach to extract the model coefficients with proper polynomial order.

A set of tailored measurement data will be required for a direct model extraction. As mentioned in [34], the computed $A_{2,1}$ value using (2.27) will enable a fundamental load-pull measurement for this direct model extraction.

$$A_{2,1}^{i} = A_{2,1}^{0} + \frac{A_{2,1}^{\Delta}}{2}\left(1+\cos\left(S_a\frac{i}{N}\right)\right)\left(\cos\left(S_p\frac{i}{N}\right)+j\sin\left(S_p\frac{i}{N}\right)\right) \tag{2.27}$$

Here in the equation, $A_{2,1}^{0}$ sets the center referencing point. The provided 'S_a' and 'S_p' represent a rate that allow the emulated Amplitude and Phase Modulation (AM/PM) trajectory, where 'N' counts the total number of points that are defined for the measurement when 'i' is sweeping from 0 to '*N-1*'.

Performing a load-pull measurement using the computed $A_{2,1}$, and with the Fourier Transformed collected device response $B_{p,h}$, analysis on the spectral lines about the Fourier index location can be applied, the CM coefficients can then be extracted with a defined expected model error threshold.

In [34], an example was shown for validation as in Fig. 2.4. The approach has proven to be accurate for directly extracting the CM with observed model complexity.

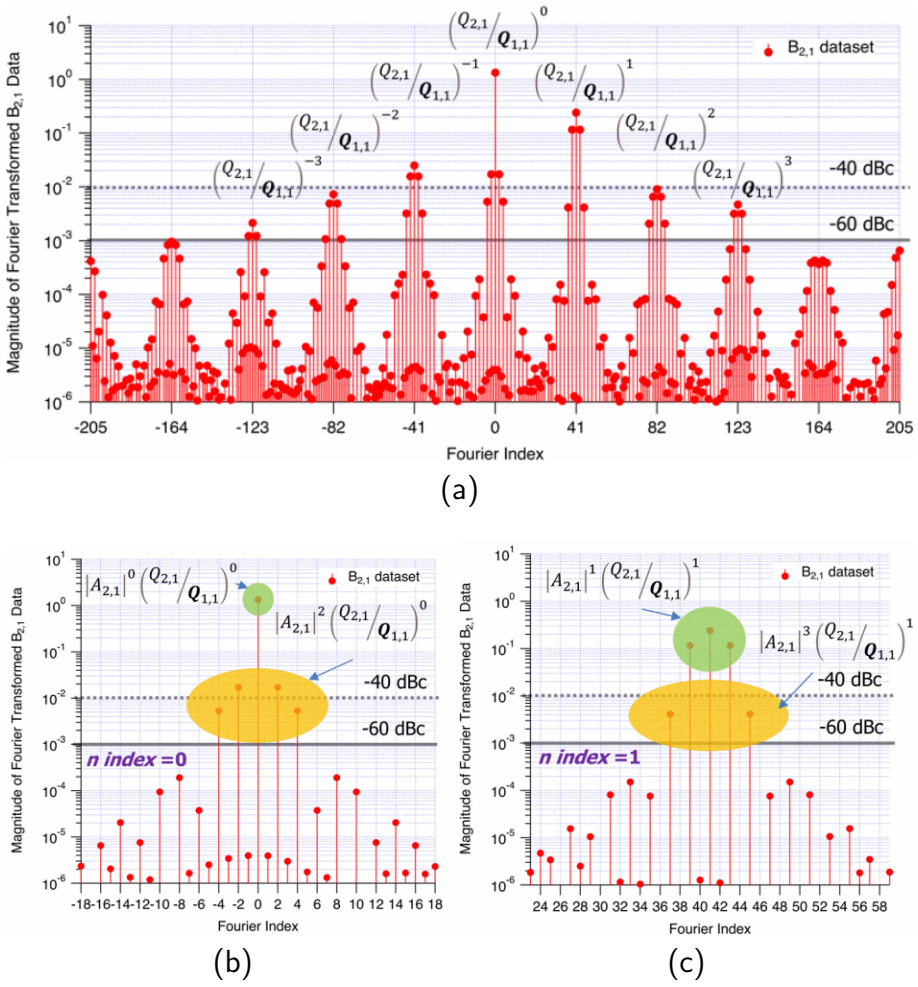

Figure 2.4: Analysis example in [34] for $B_{2,1}$ Fourier Transformed spectrum samples between - 40 dB and - 60 dB error bar on the trajectory computation dataset at each $n.Sp = n.41$ location ($S_a = 2$, $S_p = 41$ with $N = 739$) allows for the identification of the relevant exponent terms for $\left(\frac{Q_{2,1}}{Q_{1,1}}\right)^n$ (a) and $|A_{2,1}|^m$ (b-c).

2.3 Artificial Neural Network (ANN) Models

For decades, the Artificial Neural Networks (ANNs) technique has been one of the research hot-spots for developing transistor non-linear behavioural models used in the design of RF power amplifiers [15], [16], [19], [25], [26]. ANN models have been proven to be accurate in different modelling scenarios with high performance. As a powerful technique, ANNs allow for modelling the input and output relationship for the required internal circuit parameters or the device behaviour in a wide range of design cases [22], providing RF designers with an efficient way to create models for

fitting different measurement datasets [23], [38]–[41].

The accuracy of a model, as one of the main concerns when implementing a model in CAD environment [21], [42], has been the recipe to determine a suitable ANN under various RF design scenarios. Different from the CM, the ANN is not usually formed in a fixed mathematical structure. Varying the internal network structure, activation functions and training algorithms may all lead to a different result for the accuracy of the ANN model [43], [44].

2.3.1 Model Structure

ANN structure selection comes with many options, including the Standard Multilayer Perceptrons (MLP), the Knowledge-Based Neuron Network (KBNN) structure and the Combined Network structure [45]. Generally, by performing a feed-forward operational process based on the selected structure, the network is able to process given input data to approximate expected output data with different neuron topologies for most of the RF-related cases [22], [46].

Standard Multilayer Perceptrons (MLP)

Multilayer Perceptrons (MLP) is one of the most commonly used Feed-forward neural network structures that have been applied for RF designs [22]. A simple diagram of the structure is shown in Fig. 2.5.

As shown in Fig. 2.5, this is the basic structure type of the feed-forward operational process. With a sufficient amount of data, the ANN can be trained for accurate models for transistors and then applied to the design cases [23], [40], [47]. However, since the accuracy an MLP structure relies on a large amount of training data, small measurement datasets can be one of the limitations when developing an ANN using this structure [20].

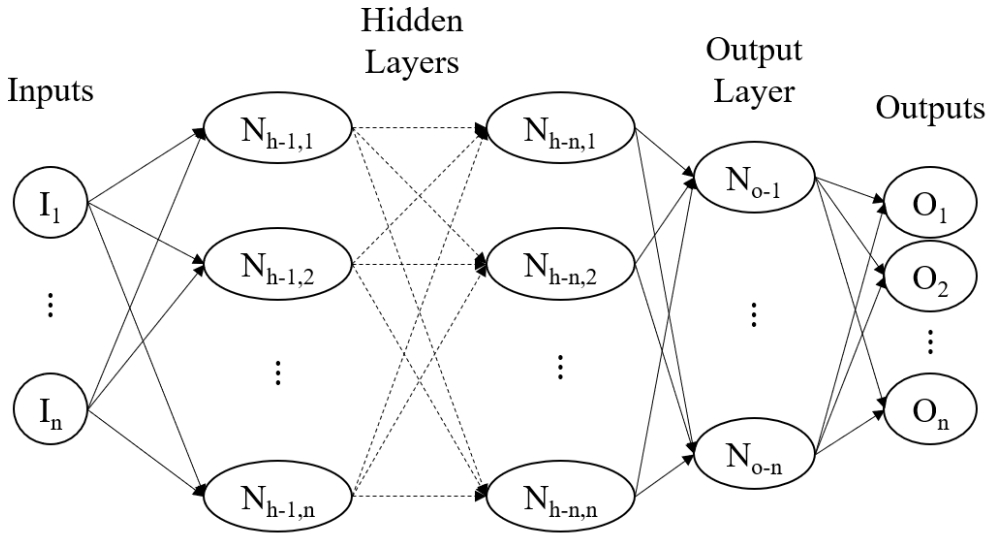

Figure 2.5: General MLP ANN structure

Knowledge-Based Neural Network (KBNN)

Therefore, the KBNN structure was proposed in [20], as the diagram shown in Fig. 2.6.

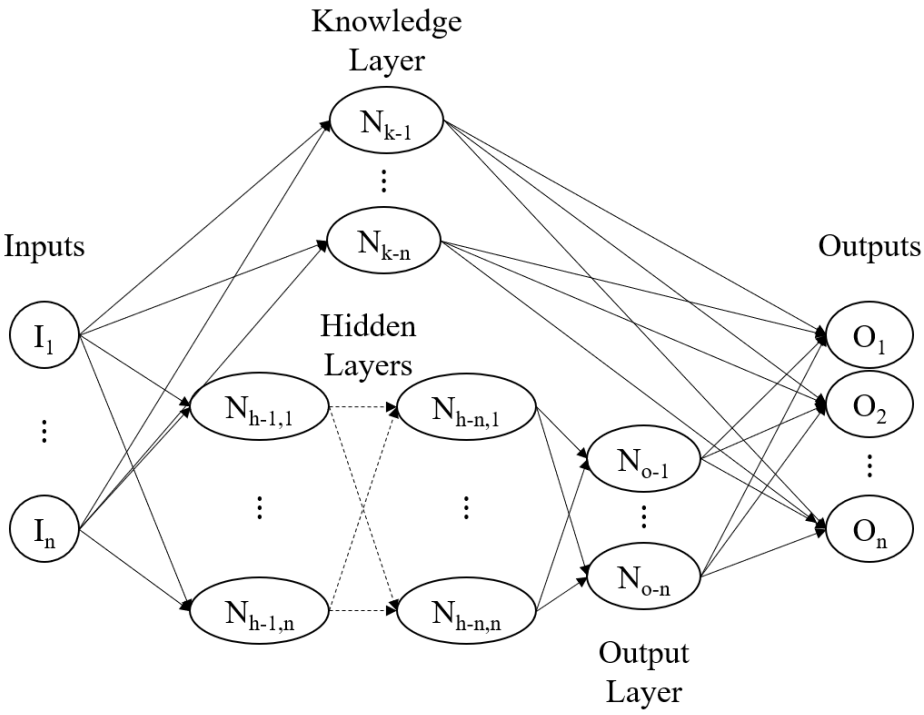

Figure 2.6: Knowledge-Based ANN structure

According to the validation shown in [20], the KBNN structure provides a model

test error that is always lower than given by the standard MLP structured models with different examples. The performance of the KBNN is better than the standard MLP not only within the measurement region, but also at the area where it is outside the model extraction region for extrapolation.

Activation Function

The activation function should be carefully selected since it could make a dramatic difference in the model training process. The selected activation function for different network topologies can be different. In general, it will stay the same between nodes within one hidden layer for one determined model. There are options for activation functions according to the ANN basis, the most popular ones for the RF design-related structures are:

The sigmoid function, formulated as (2.28) and plotted within a data range from -5 to 5 as in Fig. 2.7:

$$\text{sigmoid}(x) = \frac{1}{1 + e^{-x}} \tag{2.28}$$

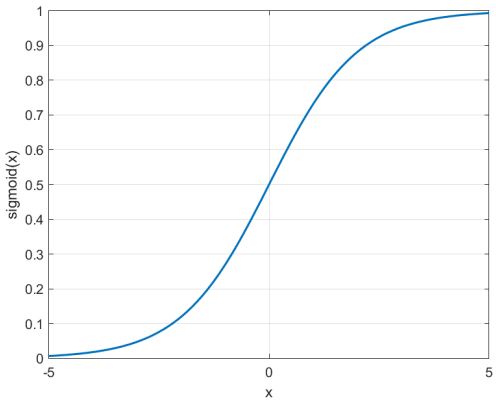

Figure 2.7: The **sigmoid** activation plot with x=[-5 5] range

The hyperbolic-tangent function, also known as the tanh function, is formulated as

(2.29) and plotted as in Fig. 2.8:

$$\tanh(x) = \frac{e^{x} - e^{-x}}{e^{x} + e^{-x}} = \frac{2}{1 + e^{-2x}} - 1 \tag{2.29}$$

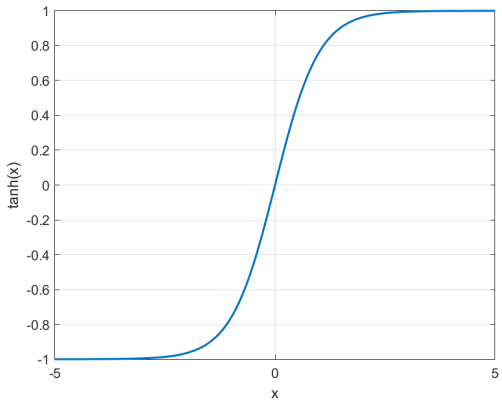

Figure 2.8: The **tanh** activation plot with x=[-5 5] range

And the rectified linear unit function, also known as the ReLU function, is formulated as (2.30) and plotted as in Fig. 2.9:

$$\text{Relu}(x) = \begin{cases} 0 & \text{if } x \leq 0 \\ \gamma & \text{if } x > 0 \end{cases} = \max(0, x) \tag{2.30}$$

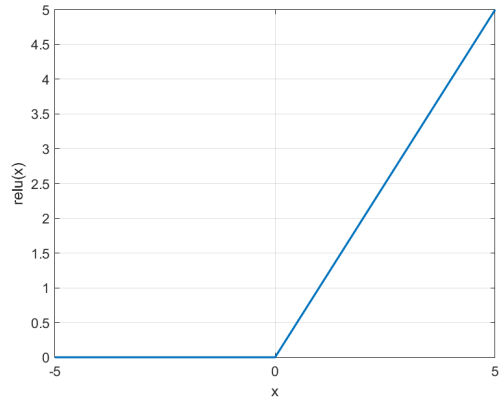

Figure 2.9: The **ReLU** activation plot with x=[-5 5] range

In an MLP process, it is common to have a non-linear relationship for neurons in

between the hidden layers. For a feed-forward network, the activation function is commonly used in between network layers (located as shown in Fig. 2.10 with the 'f' symbol) when processing the input data with hidden or output neurons to the final outputs [22].

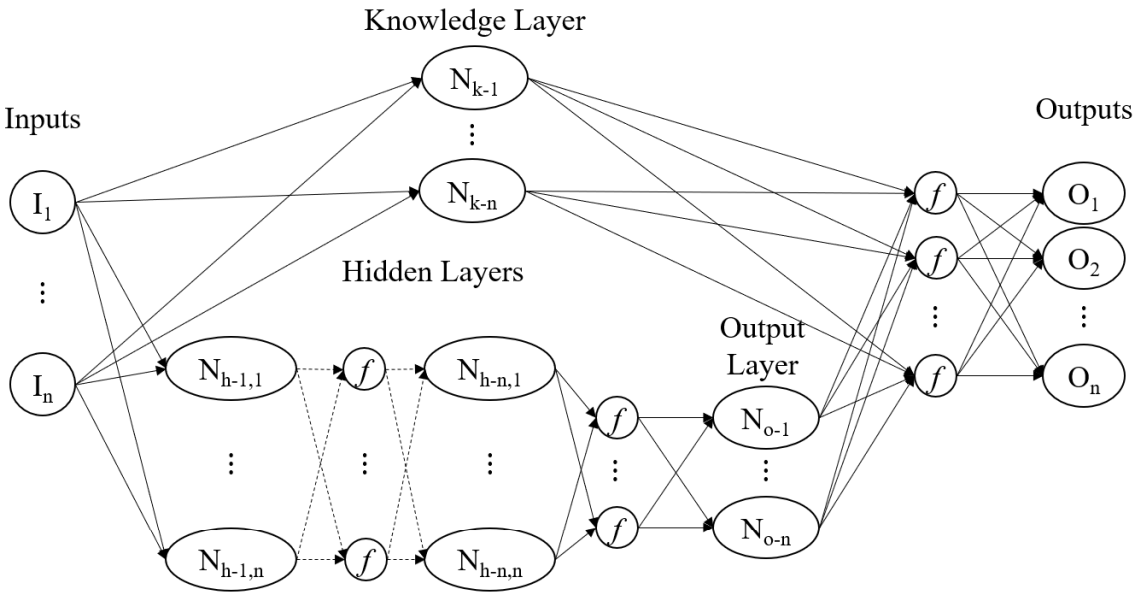

Figure 2.10: KBNN structural diagram with activation function setup

The sigmoid function was recognised as a classical activation function and commonly utilised as a part of the feed-forward data operational process [48]. However, it has also been mentioned in [49], and later with experimental evidence in [43], that the sigmoid function has proven to be slowing down the learning when compared to the tanh function. Hence, the tanh function will be a better choice, especially with a small random value of weight for the model training [43].

The ReLU function, shown with Fig. 2.9 and (2.30), was firstly mentioned in [50] then demonstrated in [51] for better training results compared to the sigmoid and the tanh function under unsupervised learning circumstances.

For the possible function after the output layer, a linear relationship corresponding to the neurons is preferred for regression, since it has been proven able to simplify and speed-up the training process with the chosen error metric, i.e. Mean Squared

Error (MSE) for the ANN model [22].

Adding Bias to the Neural Network

Referring to Fig. 2.7 - 2.9, all activation function lines go across the origin $(0, 0)$ point of the axis. To ensure that the centre given by the activation function does not always fall on zero, which may cause derivative issues for the back-propagation process, the bias point was added to cooperate with each neuron as shown in Fig. 2.11 on the structure diagram. With the added bias, as a trainable value to allow a flexible offset of the model, chances for better fitting results will be possible.

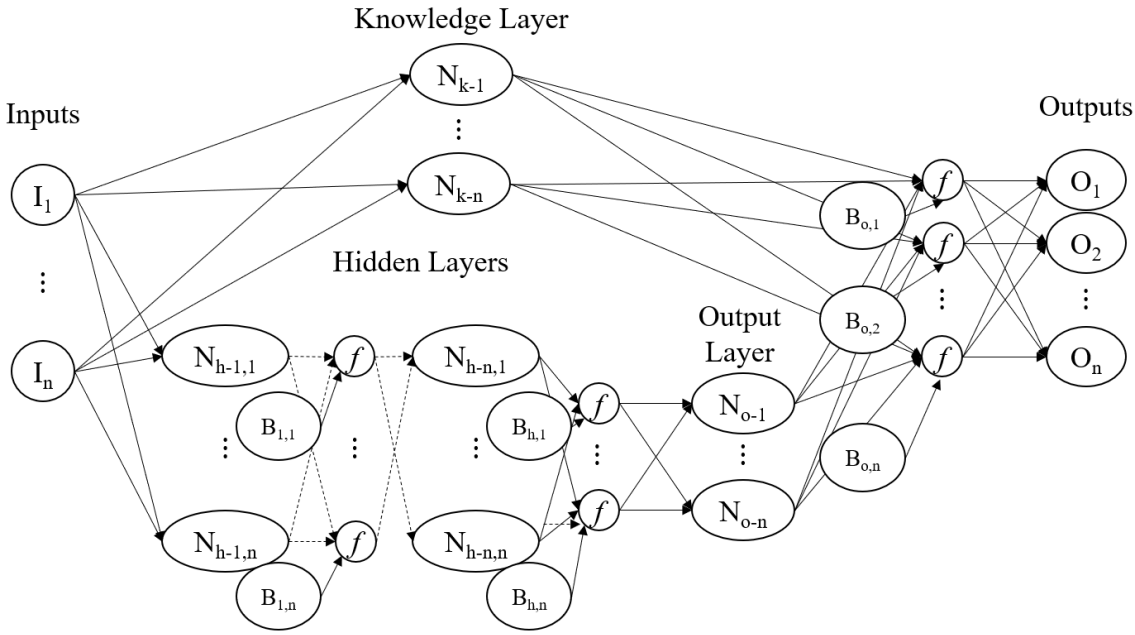

Figure 2.11: Structural diagram with bias added to the setup

2.3.2 Back-Propagation (BP) Training Algorithm

The determined ANN structure will be set up with initialized values of weights and biases. However, the initial values are usually random so not the best option for the model. A training process is then needed for the weights and biases of the ANN to be optimized for an accurate model. Generally, there are three types of training

categories: supervised training, unsupervised training, and reinforcement training.

The Back-Propagation (BP) training, with gradient-based techniques under the supervised learning category, is usually the optimization method used to minimize the prediction error of the model. The error calculation and the gradient descent analysis are the keys to this type of training algorithm. Given the input dataset after processing with the internal weights and biases through the activation function, the network output is compared to the given training output dataset for error calculation, which will then be used as the determined statements to update the initial weights and bias values.

General gradient descent error back-propagation applies partial differentiation to the error calculation for weight and bias updates:

$$W_{i+1} = W_i - \eta \frac{\partial E}{\partial W_i} \tag{2.31}$$

$$b_{i+1} = b_i - \eta \frac{\partial E}{\partial b_i} \tag{2.32}$$

here in (2.31) and (2.32), 'i' represents the index number, 'W' and 'b' represent the weight and bias. The variable 'η' is an adjustable variable called learning rate [52], which can be varied depending on the training algorithm.

Under the gradient descent error back-propagation category, there are the Quasi-Newton [53], the Levenberg-Mquart (LM) [54] and the Bayesian Regularization [55], [56] training algorithms, which are popular for RF related model extraction. Among the back-propagation training algorithms, the LM algorithm allows for the fastest convergence [22]. The algorithm process procedure can be summarised as shown in Algorithm 1 [54].

Algorithm 1 Levenberg-Marquart Algorithm

1: INPUT:$\underline{\mathbf{p}}$, $\underline{\mathbf{t}}$
2: $\underline{a}^0 = \underline{p}$
3: $\underline{a}^{k+1} = \underline{f}^{k+1}\left(W^{k+1}\underline{a}^k + \underline{b}^{k+1}\right)$, $k = 0, 1, \ldots, M-1$
4: $\underline{e}_i = \underline{t}_i - \underline{a}_i^M$, $i = 1, 2, \ldots, N$
5: $V(\underline{x}) = \sum_{k=0}^{N} \underline{e}_i^2(\underline{x})$, $\underline{x} = [W, \ldots, b, \ldots]$
6: *Compute* ***Jacobian*** $J(\underline{x}) = \begin{bmatrix} \frac{\partial e_1(\underline{x})}{\partial x_1} & \frac{\partial e_1(\underline{x})}{\partial x_2} & \cdots & \frac{\partial e_1(\underline{x})}{\partial x_n} \\ \frac{\partial e_2(\underline{x})}{\partial x_1} & \frac{\partial e_2(\underline{x})}{\partial x_2} & \cdots & \frac{\partial e_2(\underline{x})}{\partial x_n} \\ \vdots & \vdots & \ddots & \vdots \\ \frac{\partial e_N(\underline{x})}{\partial x_1} & \frac{\partial e_N(\underline{x})}{\partial x_2} & \cdots & \frac{\partial e_N(\underline{x})}{\partial x_n} \end{bmatrix}$
7: $\Delta\underline{x} = \left[J^T(\underline{x})J(\underline{x}) + \mu I\right]^{-1} J^T(\underline{x})\underline{e}(\underline{x})$
8: *Compute* $V(\underline{x} + \Delta\underline{x})$ *by repeating Step 1 to 4*
9: **if** $V(\underline{x} + \Delta\underline{x}) < V(\underline{x})$ **then**
10: $\mu = \mu \times \beta$
11: **else**
12: **if** $V(\underline{x} + \Delta\underline{x}) \geq V(\underline{x})$ **then**
13: $\mu = \mu \div \beta$
14: **end if**
15: **end if**
16: OUTPUT: $\underline{\mathbf{a}}$

where in the algorithm, 'p' and 't' are the given input data for training the ANN model, 'M' represents the number of layers, 'N' represents the number of samples, and 'a' is the final output produced by the model.

The LM training algorithm, as the basis of the Bayesian Regularization training algorithm, is based on the Quasi-Newton approximation with the Hessian matrix. By varying the value of the learning rate 'μ', the LM algorithm can be as the gradient descent when 'μ' is large, as just Newton's method when 'μ' is 0 [57]. In this instance, an adaptable framework is provided. It is worth noting that its theory base is comparable to the Least Mean-Squared (LMS) algorithm, which is the theory base of the Cardiff Model. The equivalent theory foundation allows increasing feasibility when searching for possibilities combining the ANN technique and the CM. Therefore, the LM training algorithm was selected in this work for further investigation.

In this context, it is essential to consider that ANN training algorithms rely on a random parameters initialisation [43]. Different initial values for hidden neuron numbers, weights and biases may lead to varied model performance. To avoid the phenomena of over-learning, under-learning or even failure for the algorithm to converge, the parameter initialisation procedure may require multiple attempts for a successful ANN training.

2.3.3 Model Implementation in MATLAB

The ANN implementation process can be implemented in various coding languages in different computing environments, such as C, $C++$, and Python, which is popular nowadays, or $C\#$ in some of the measurement systems.

For preliminary ANN testing, MATLAB offers a Neural Network Fitting application in the deep learning toolbox with a user-friendly interface. With the Fitting application, experiments for ANN technique verification can be easily applied, to explore how ANN structures with different combinations of the selected activation functions, weights and biases with numbers and values are linked towards different model performances.

The dataset loading, splitting, the neural number and training algorithm selection before a training section can all be defined through the Fitting app interface. On the final interface page, the Fitting app allows essential parameters and plots of the ANN training to be visualised, as in Fig. 2.12.

The ANN training procedure can be done and saved with the Fitting app. After the training, the dataset or network adjustment for possible retraining requirements and the trained network testing function are also available with the app. Therefore, the Neural Network Fitting app from the MATLAB deep learning toolbox can be a commendable starting point.

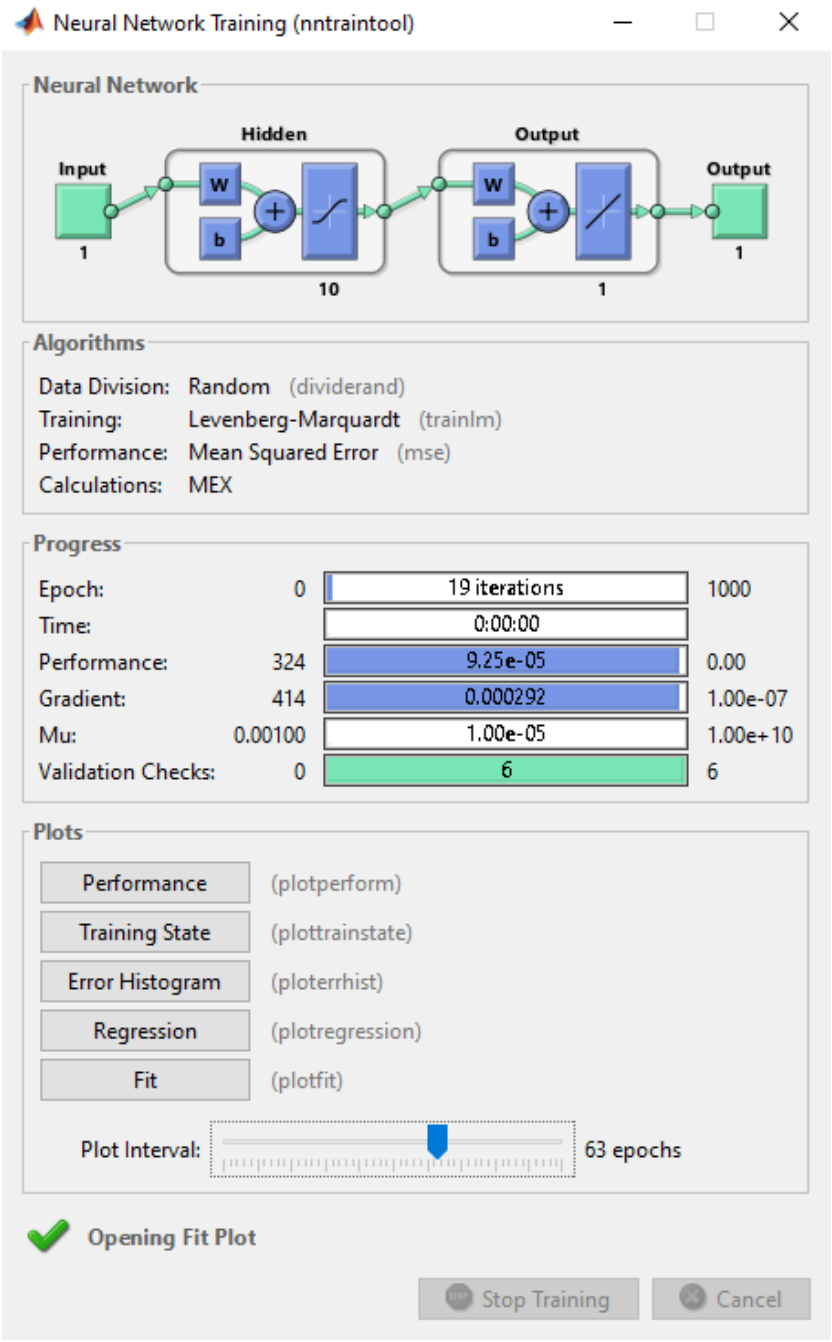

Figure 2.12: MATLAB ANN toolbox interface

However, when applying the ANN technique for model extraction with RF design tasks, parameters and plots that represent the training procedure are not sufficient anymore. More RF-related parameters and plots, such as the output power, efficiency, waveforms and contours on the Smith Chart will be required to be implemented via MATLAB script manually for a successful ANN model extraction determination.

In addition, if moving towards the detailed internal parameters of the ANN, the Fitting app limits the flexibility of adjusting the preset configurations, especially for the training algorithms. Hence, for further investigation about how the ANN setup will impact the model performance, independent implementation of the ANN structure and the training procedure will be a better choice. This can enable a systematic breakdown, proceeding step by step into the ANN model interactions.

2.4 Conclusion

In this chapter, a brief summary about the development of the RF transistor behavioural modelling technique is delivered, including the theory foundation of S-parameters, VIOMAP, Hot S-parameter model and PHD model. The CM and the ANN model are thoroughly addressed with the theoretical framework and their practical implementation. The concluded reviews given to the CM and the ANN model, e.g., the model extraction determining methods, and critical parameters for consideration, set the stage for the subsequent analysis of the model extrapolation ability verification and comparison.

References

[1] I. Angelov, H. Zirath, N. Rosman, "A new empirical nonlinear model for HEMT and MESFET devices," *IEEE Trans. Microw. Theory Techn.*, vol. 40, no. 12, pp. 2258–2266, Dec. 1992. DOI: 10.1109/22.179888.

[2] A. Belmecheri, M. Djebari, "A Large Signal GaN HEMT Transistor Based on the Angelov Model Parameters Extraction Applied to Single Stage Low Noise Amplifier," *Transactions on Electrical and Electronic Materials*, vol. 23, pp. 595–608, Dec. 2022. DOI: 10.1007/s42341-022-00390-z.

[3] Luo, H., Hu, W., Guo, Y., "On large-signal modeling of GaN HEMTs: past, development and future," *Chip*, vol. 2, no. 3, p. 100 052, 2023, ISSN: 2709-4723. DOI: https://doi.org/10.1016/j.chip.2023.100052. [Online].

Available: https://www.sciencedirect.com/science/article/pii/S2709472323000151.

[4] U. Radhakrishna, T. Imada, T. Palacios, D. Antoniadis, "MIT virtual source GaNFET-high voltage (MVSG-HV) model: A physics based compact model for HV-GaN HEMTs," *physica status solidi c*, vol. 11, no. 3-4, pp. 848–852, Mar. 2014. DOI: https://doi.org/10.1002/pssc.201300392. eprint: https://onlinelibrary.wiley.com/doi/pdf/10.1002/pssc.201300392. [Online]. Available: https://onlinelibrary.wiley.com/doi/abs/10.1002/pssc.201300392.

[5] A.A. Kokolov, L.I. Babak, "Methodology of built and verification of non-linear EEHEMT model for GaN HEMT transistor," *Radioelectron.Commun.Syst.*, vol. 58, no. 10, pp. 3–14, Oct. 2015. DOI: https://doi.org/10.3103/S0735272715100015.

[6] S. Khandelwal, Y.S. Chauhan, T.A. Fjeldly, "ASM GaN: Industry Standard Model for GaN RF and Power Devices—Part 1: DC, CV, and RF Model," *IEEE Trans. Electron Devices*, vol. 66, no. 1, pp. 80–86, Jan. 2019. DOI: 10.1109/TED.2018.2867874.

[7] D. Root, "Technology-independent large-signal FET models: A measurement-based approach to active device modeling," in *15 ARMMS Conf., Bath*, Sep. 1991, pp. 1, 21.

[8] D.E. Root, J. Xu, J. Horn, M. Iwamoto, "The large-signal model: theoretical foundations, practical considerations, and recent trends," in *Nonlinear Transistor Model Parameter Extraction Techniques* (The Cambridge RF and Microwave Engineering Series), M. Rudolph, C. Fager, and D. E. Root, Eds., The Cambridge RF and Microwave Engineering Series. Cambridge: Cambridge University Press, 2011, pp. 123–170.

[9] F. Verbeyst, M.V. Bossche, "VIOMAP, 16QAM and Spectral Regrowth: Enhanced Prediction and Predistortion based on Two-Tone Black-Box Model Extraction," in *45th ARFTG Conference Digest*, vol. 27, Orlando, FL, USA, May 1995, pp. 19–28. DOI: 10.1109/ARFTG.1995.327101.

[10] S.R. Mazumder, Puije, P. v., "Two-Signal Method of Measuring the Large-Signal S-Parameters of Transistors," *IEEE Transactions on Microwave Theory and Techniques*, vol. 26, no. 6, pp. 417–420, Jun. 1978. DOI: 10.1109/TMTT.1978.1129404.

[11] J. Verspecht, "Large-signal network analysis," *IEEE Microwave Magazine*, vol. 6, no. 4, pp. 82–92, Dec. 2005. DOI: 10.1109/MMW.2005.1580340.

[12] D.E. Root, J. Verspecht, J. Horn, M. Marcu, *X-parameters : characterization, modeling, and design of nonlinear RF and microwave components* (The Cambridge RF and microwave engineering series), eng. Cambridge: Cambridge University Press, 2013, ISBN: 9780521193238.

[13] S. Woodington, T. Williams, H. Qi, "A novel measurement based method enabling rapid extraction of a RF Waveform Look-Up table based behavioral model," in *2008 IEEE MTT-S International Microwave Symposium Digest*, Atlanta, GA, USA, Jun. 2008, pp. 1453–1456. DOI: 10.1109/MWSYM.2008.4633053.

[14] P.J. Tasker, J. Benedikt, "Waveform Inspired Models and the Harmonic Balance Emulator," *IEEE Microwave Magazine*, vol. 12, no. 2, pp. 38–54, Apr. 2011. DOI: 10.1109/MMM.2010.940101.

[15] F. Güne, F. Gürgen, H. Torpi, "Signal-noise neural network model for active microwave devices," *IEE Proceedings: Circuits, Devices and Systems*, vol. 143, pp. 1–8, 1 Feb. 1996, ISSN: 13502409. DOI: 10.1049/ip-cds:19960150.

[16] K. Shirakawa, M. Shimiz, N. Okubo, Y. Daido, "A Large-Signal Characterization of an HEMT Using a Multilayered Neural Network," *IEEE Transactions on Microwave Theory and Techniques*, vol. 45, pp. 1630–1633, 9 Sep. 1997, ISSN: 00189480. DOI: 10.1109/22.622932.

[17] J. Wood, D.E. Root, *Fundamentals of Nonlinear Behavioral Modeling for RF and Microwave Design*. Norwood,MA: Artech House, May 2005, ISBN: 1-58053-775-8.

[18] J. Xu, R. Jones, S.A. Harris, T. Nielsen, D.E. Root, "Dynamic FET model - DynaFET - for GaN transistors from NVNA active source injection measurements," in *IEEE MTT-S International Microwave Symposium (IMS2014)*, Tampa, FL, USA, Jun. 2014, pp. 1–3. DOI: 10.1109/MWSYM.2014.6848293.

[19] V.B. Litovski, J.I. Radjenovic, C.M. Mrcarica, S.Lj. Milenkovic, "MOS transistor modelung using neural network," *Electronics Letters*, vol. 28, 18 Aug. 1992, ISSN: 00135194. DOI: 10.1049/el:19921124.

[20] W. Fang, Q.J. Zhang, "Knowledge based neural models for microwave design," in *1997 IEEE MTT-S International Microwave Symposium Digest*, vol. 2, Denver, CO, USA, Jun. 1997, 627–630 vol.2. DOI: 10.1109/MWSYM.1997.602870.

[21] K.C. Gupta, "Emerging trends in millimeter-wave CAD," *IEEE Transactions on Microwave Theory and Techniques*, vol. 46, no. 6, pp. 747–755, Jun. 1998. DOI: 10.1109/22.681196.

[22] Q. -J. Zhang, K. C. Gupta, *Neural Networks for RF and Microwave Design*. Boston, MS, USA: Artech House, 2000.

[23] J. Louro, C. Belchior, D.R. Barros, "New Transistor Behavioral Model Formulation Suitable for Doherty PA Design," *IEEE Transactions on Microwave Theory and Techniques*, vol. 69, no. 4, pp. 2138–2147, Apr. 2021. DOI: 10.1109/TMTT.2021.3054645.

[24] F. Verbeyst, V. Bossche, "VIOMAP, the S-parameter equivalent for weakly nonlinear RF and microwave devices," eng, *IEEE transactions on microwave theory and techniques*, vol. 42, no. 12, pp. 2531–2535, Dec. 1994, ISSN: 0018-9480.

[25] T. Gasseling, D. Barataud, S. Mons, "Hot small-signal S-parameter measurements of power transistors operating under large-signal conditions in a load-pull environment for the study of nonlinear parametric interactions," *IEEE Transactions on Microwave Theory and Techniques*, vol. 52, no. 3, pp. 805–812, Mar. 2004. DOI: 10.1109/TMTT.2004.823528.

[26] J. Verspecht, D. Barataud, J.-P. Teyssier, J.-M. Nebus, "Hot S-parameter techniques: 6 = 4 + 2," eng, in *2005 66th ARFTG Microwave Measurement Conference (ARFTG)*, Washington, DC, USA: IEEE, Dec. 2005, pp. 1–9, ISBN: 1538672928.

[27] J. Verspecht, M.V. Bossche, F. Verbeyst, "Characterizing Components Under Large Signal Excitation: Defining Sensible "Large Signal S-Parameters"?!" In *49th ARFTG Conference Digest*, vol. 31, Denver, CO, USA, Jun. 1997, pp. 109–117. DOI: 10.1109/ARFTG.1997.327217.

[28] D.E. Root, J. Verspecht, D. Sharrit, J. Wood, A. Cognata, "Broad-band polyharmonic distortion (PHD) behavioral models from fast automated simulations and large-signal vectorial network measurements," *IEEE Transactions on Microwave Theory and Techniques*, vol. 53, no. 11, pp. 3656–3664, Nov. 2005. DOI: 10.1109/TMTT.2005.855728.

[29] J. Verspecht, D.E. Root, "Polyharmonic distortion modeling," *IEEE Microwave Magazine*, vol. 7, no. 3, pp. 44–57, Jun. 2006. DOI: 10.1109/MMW.2006.1638289.

[30] H. Qi, J. Benedikt, P. Tasker, "A Novel Approach for Effective Import of Nonlinear Device Characteristics into CAD for Large Signal Power Amplifier Design," in *2006 IEEE MTT-S International Microwave Symposium Digest*, San Francisco, CA, USA, Jun. 2006, pp. 477–480. DOI: 10.1109/MWSYM.2006.249596.

[31] H. Qi, J. Benedikt, P.J. Tasker, "Novel Nonlinear Model for Rapid Waveform-based Extraction Enabling Accurate High Power PA Design," in *2007 IEEE/MTT-S International Microwave Symposium*, Honolulu, HI, USA, Jun. 2007, pp. 2019–2022. DOI: 10.1109/MWSYM.2007.380246.

[32] H. Qi, J. Benedikt, P.J. Tasker, "Nonlinear Data Utilization: From Direct Data Lookup to Behavioral Modeling," *IEEE Transactions on Microwave Theory and Techniques*, vol. 57, no. 6, pp. 1425–1432, Jun. 2009. DOI: 10.1109/TMTT.2009.2019996.

[33] P.J. Tasker, "Practical waveform engineering," *IEEE Microwave Magazine*, vol. 10, no. 7, pp. 65–76, Dec. 2009. DOI: 10.1109/MMM.2009.934518.

[34] P.J. Tasker, "Robust Extraction of Cardiff Model Parameters from Appropriately Tailored Measured Load-Pull Data," in *2020 IEEE BiCMOS and Compound Semiconductor Integrated Circuits and Technology Symposium (BCICTS)*, Monterey, CA, USA, Nov. 2020, pp. 1–5. DOI: 10.1109/BCICTS48439.2020.9392942.

[35] S. Woodington, "Behavioural model analysis of active harmonic load-pull measurements," eng, Ph.D. dissertation, School of Engineering, Cardiff University, 2011.

[36] S. Woodington, R. Saini, D. Williams, J. Lees, J. Benedikt, P.J. Tasker, "Behavioral model analysis of active harmonic load-pull measurements," in *2010 IEEE MTT-S International Microwave Symposium*, Anaheim, CA, USA, May 2010, pp. 1688–1691. DOI: 10.1109/MWSYM.2010.5517261.

[37] J.J. Bell, R. Saini, S. Woodington, "Behavioral model analysis using simultaneous active fundamental load-pull and harmonic source-pull measurements at X-band," in *2011 IEEE MTT-S International Microwave Symposium*, Baltimore, MD, USA, Jun. 2011, pp. 1–4. DOI: 10.1109/MWSYM.2011.5972803.

[38] V.K. Devabhaktuni, C. Xi, F. Wang, Q.J. Zhang, "Robust training of microwave neural models," in *1999 IEEE MTT-S International Microwave Symposium Digest (Cat. No.99CH36282)*, vol. 1, Anaheim, CA, USA, Jun. 1999, 145–148 vol.1. DOI: 10.1109/MWSYM.1999.779444.

[39] J. Wood, D.E. Root, *Fundamentals of nonlinear behavioral modeling for RF and microwave design* (Artech House microwave library), eng. Boston, Mass. ; Artech House, 2005, ISBN: 9781580537759.

[40] J. Cai, J. Wang, C. Yu, H. Lu, J. Liu, L. Sun, "An artificial neural network based nonlinear behavioral model for RF power transistors," in *2017 IEEE Asia Pacific Microwave Conference (APMC)*, Kuala Lumpur, Malaysia, Nov. 2017, pp. 600–603. DOI: 10.1109/APMC.2017.8251517.

[41] F. Feng, W. Na, J. Jin, J. Zhang, W. Zhang, Q.-J. Zhang, "Artificial Neural Networks for Microwave Computer-Aided Design: The State of the Art," *IEEE Transactions on Microwave Theory and Techniques*, vol. 70, no. 11, pp. 4597–4619, Nov. 2022. DOI: 10.1109/TMTT.2022.3197751.

[42] M.R. Moure, M. Casbon, M. Fernández-Barciela, P.J. Tasker, "A Systematic Investigation of Behavioural Model Complexity Requirements," in *2018 13th European Microwave Integrated Circuits Conference (EuMIC)*, Madrid, Spain, Sep. 2018, pp. 77–80. DOI: 10.23919/EuMIC.2018.8539950.

[43] X. Glorot, Y. Bengio, "Understanding the difficulty of training deep feedforward neural networks," in *Proceedings of the Thirteenth International Conference on Artificial Intelligence and Statistics*, Y. W. Teh and M. Titterington, Eds., ser. Proceedings of Machine Learning Research, vol. 9, Chia Laguna Resort, Sardinia, Italy: PMLR, May 2010, pp. 249–256. [Online]. Available: https://proceedings.mlr.press/v9/glorot10a.html.

[44] D. Hunter, H. Yu, M.S. Pukish, I., J. Kolbusz, B.M. Wilamowski, "Selection of Proper Neural Network Sizes and Architectures—A Comparative Study," *IEEE Transactions on Industrial Informatics*, vol. 8, no. 2, pp. 228–240, Feb. 2012. DOI: 10.1109/TII.2012.2187914.

[45] F. Wang, V.K. Devabhaktuni, C. Xi, Q.J. Zhang, "Neural network structures and training algorithms for RF and microwave applications," *International Journal of RF and Microwave Computer-Aided Engineering*, vol. 9, no. 3, pp. 216–240, Mar. 1999. DOI: https://doi.org/10.1002/(SICI)1099-047X(199905)9:3<216::AID-MMCE7>3.0.CO;2-W.

[46] F. Scarselli, C.T. Ah, "Universal Approximation Using Feedforward Neural Networks: A Survey of Some Existing Methods, and Some New Results," *Neural Networks*, vol. 11, no. 1, pp. 15–37, Jan. 1998, ISSN: 0893-6080. DOI: https://doi.org/10.1016/S0893-6080(97)00097-X. [Online]. Available: https://www.sciencedirect.com/science/article/pii/S089360809700097X.

[47] A. Khusro, S. Husain, M.S. Hashmi, A.Q. Ansari, "Small signal behavioral modeling technique of GaN high electron mobility transistor using artificial neural network: An accurate, fast, and reliable approach," *International Journal of RF and Microwave Computer-Aided Engineering*, vol. 30, no. 4, e22112, Apr. 2020. DOI: https://doi.org/10.1002/mmce.22112.

[48] M.H. Bakr, M.H. Negm, "Chapter Three - Modeling and Design of High-Frequency Structures Using Artificial Neural Networks and Space Mapping," in *Silicon-Based Millimeter-wave Technology*, ser. Advances in Imaging and Electron Physics, M. J. Deen, Ed., vol. 174, Elsevier, 2012, pp. 223–260. DOI:

https://doi.org/10.1016/B978-0-12-394298-2.00003-X. [Online]. Available: https://www.sciencedirect.com/science/article/pii/B978012394298200003X.

[49] B.L. Kalman, S.C. Kwasny, "Why tanh: choosing a sigmoidal function," in *[Proceedings 1992] IJCNN International Joint Conference on Neural Networks*, vol. 4, Baltimore, MD, USA, Jun. 1992, 578–581 vol.4. DOI: 10.1109/IJCNN.1992.227257.

[50] R.H.R. Hahnloser, R. Sarpeshkar, M.A. Mahowald, R.J. Douglas, H.S. Seung, "Digital selection and analogue amplification coexist in a cortex-inspired silicon circuit," *Nature (London)*, vol. 405, no. 6789, pp. 947–951, Dec. 2000, ISSN: 0028-0836.

[51] X. Glorot, A. Bordes, Y. Bengio, "Deep sparse rectifier neural networks," eng, *Journal of machine learning research*, vol. 15, pp. 315–323, Jun. 2011, ISSN: 1532-4435.

[52] R.A. Jacobs, "Increased rates of convergence through learning rate adaptation," *Neural Networks*, vol. 1, no. 4, pp. 295–307, 1988, ISSN: 0893-6080. DOI: https://doi.org/10.1016/0893-6080(88)90003-2. [Online]. Available: https://www.sciencedirect.com/science/article/pii/0893608088900032.

[53] A. Antoniou, W. Lu, *Practical Optimization Algorithms and Engineering Applications* (Texts in Computer Science), eng, 2nd ed. 2021. New York, NY: Springer US, 2021, ISBN: 1-0716-0843-6.

[54] M.T. Hagan, M.B. Menhaj, "Training feedforward networks with the Marquardt algorithm," *IEEE Transactions on Neural Networks*, vol. 5, no. 6, pp. 989–993, Jun. 1994. DOI: 10.1109/72.329697.

[55] F.D. Foresee, M.T. Hagan, "Gauss-Newton approximation to Bayesian learning," in *Proceedings of International Conference on Neural Networks (ICNN'97)*, vol. 3, Houston, TX, USA, Jun. 1997, 1930–1935 vol.3. DOI: 10.1109/ICNN.1997.614194.

[56] F. Burden, D. Winkler, "Bayesian Regularization of Neural Networks," eng, *Artificial Neural Networks*, vol. 458, pp. 23–42, 2008, ISSN: 1064-3745.

[57] Inc. T. M., *Levenberg-Marquardt backpropagation*, Natick, Massachusetts, United States, 2006. [Online]. Available: https://uk.mathworks.com/help/deeplearning/ref/trainlm.html.

Chapter 3

Extrapolation Analysis and Comparison of the Cardiff Model (CM) and the Artificial Neural Network (ANN) Model

Load-pull measurements for obtaining large datasets from RF devices for model extraction can be expensive and time-consuming. Hence, a robust behavioural model requires not only an accurate interpolation predicting ability, but also a reasonable extrapolation predicting ability. The unrealistic optimum power or efficiency variations, produced by a model with poor extrapolation ability, may lead to the possibility for an optimiser not to converge or converge on non-physical solutions. A robust model can prevent the appearance of non-physical behaviour when used in Computer-Aided Design (CAD) simulation for RF design optimisation procedures.

In this chapter, a comparison of extrapolation ability is made between the Cardiff Model (CM) and Artificial Neural Network (ANN) based behavioural models. A Keysight Advanced Design System (ADS) schematic is created for an active load-pull

measurement simulation to provide a design-related dataset for model extraction, and an expanded dataset that covers the whole Smith Chart for reference on the model extrapolation analysis. Two ways of extracting the CM will be presented, one with the formal CM definition [1] and the other one using spectral line analysis [2]. The potential extrapolation problem from the two CM extraction methods will be analysed. Then, the ANN models, with selected structure and training technique, are also tested for their extrapolation ability. The model extraction procedures are implemented and processed in the MATLAB environment. The discussions on all the model performances are given respectively at the end.

3.1 Data Acquisition

The load-pull setup, implemented in ADS, is used to acquire pseudo-wave datasets of the Wolfspeed 10 W gallium nitride (GaN) transistor as in Fig.3.1. The device is measured with a constant input drive corresponding to 1 dB compression at the optimum load, biased at $V_{gs} = -2.2\,\text{V}$, $V_{ds} = 28\,\text{V}$.

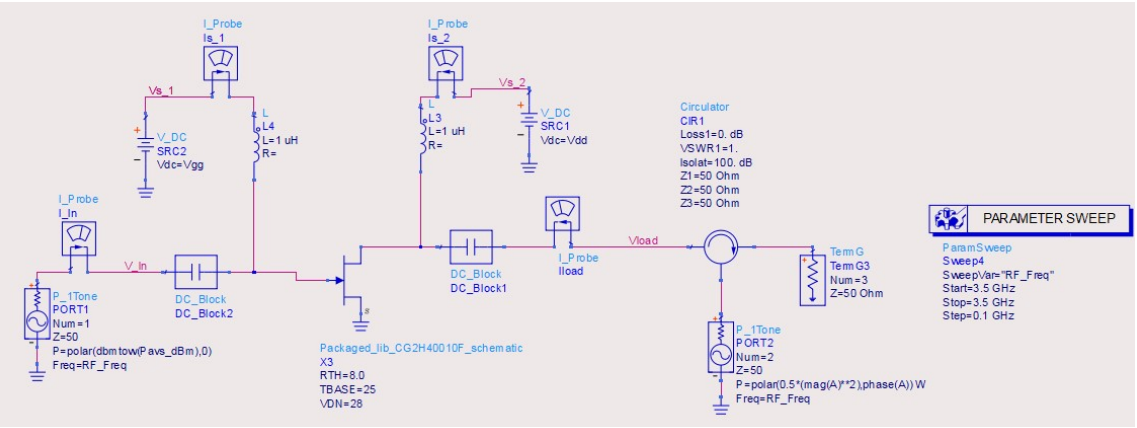

Figure 3.1: A-pull simulation setup with Wolfspeed 10 W in ADS

Note that for acquiring a tailored dataset to follow the spectrum analysis in [2], an extra circulator is added to present the active load-pull. A set of modulated 'A' waves for the source is generated using (3.1). The value of 'S_a' is chosen as 1, 'S_p' is chosen as 19, and 'k' is chosen as 6 for the impact of aliasing with a total number

of data points, '$N = (2 \cdot k \cdot S_p) + 1$', equals 229 are used for the tailored '$A^i_{2,1}$' to be calculated. $A^0_{2,1}$ and $A^\Delta_{2,1}$ are selected as $-2 + 0i$ and $0.8 + 1i$ respectively for a reasonable design-related coverage on the Smith Chart (will be shown later in Fig. 3.4).

$$A^i_{2,1} = A^0_{2,1} + \frac{A^\Delta_{2,1}}{2}\left(1 + \cos\left(S_a \frac{i}{N}\right)\right)\left(\cos\left(S_p \frac{i}{N}\right) + j\sin\left(S_p \frac{i}{N}\right)\right) \tag{3.1}$$

Using the following (3.2) and (3.3) equations, the A-B wave data can be calculated with the measured voltage and current. In Fig. 3.2-3.3, the acquired $A_{2,1}$ and $B_{2,1}$ and the Fourier Transformed spectrum are plotted for later model analysis. Here, Z_R, the impedance reference is $50\,\Omega$.

$$A_{p,h} = \frac{V_p + 50I_{In}}{2\sqrt{50}} \tag{3.2}$$

$$B_{p,h} = \frac{V_p - 50I_{load}}{2\sqrt{50}} \tag{3.3}$$

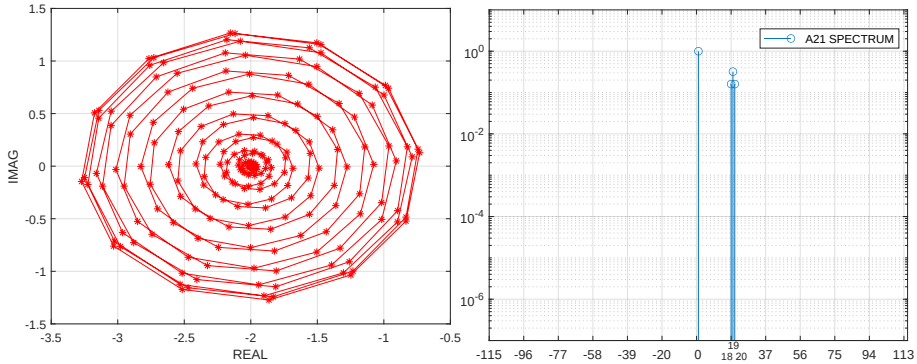

Figure 3.2: $A_{2,1}$ sample (a) and its Fourier Transformed spectrum (b) on a trajectory computation.

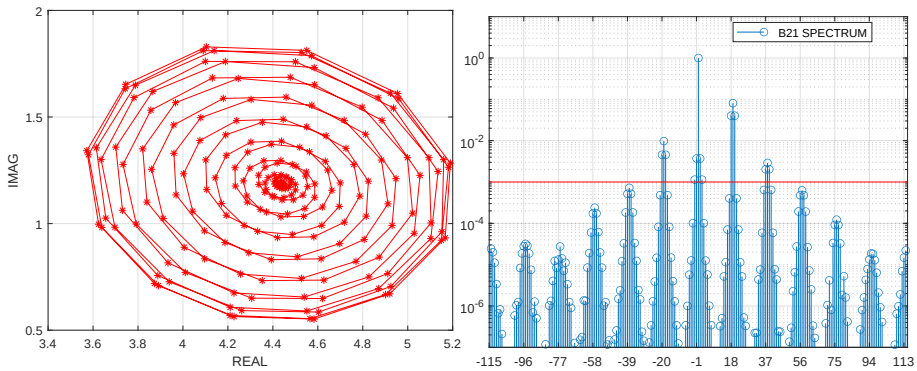

Figure 3.3: $B_{2,1}$ sample (a) and its Fourier Transformed spectrum with -60dB error bar (which refers to an expecting 0.1% accuracy of the extracted model) (b) on the trajectory computation.

The correlated reflection coefficient (Γ) is calculated with (3.4) and plotted in Fig. 3.4.

$$\Gamma_{p,h} = \frac{A_{p,h}}{B_{p,h}} \tag{3.4}$$

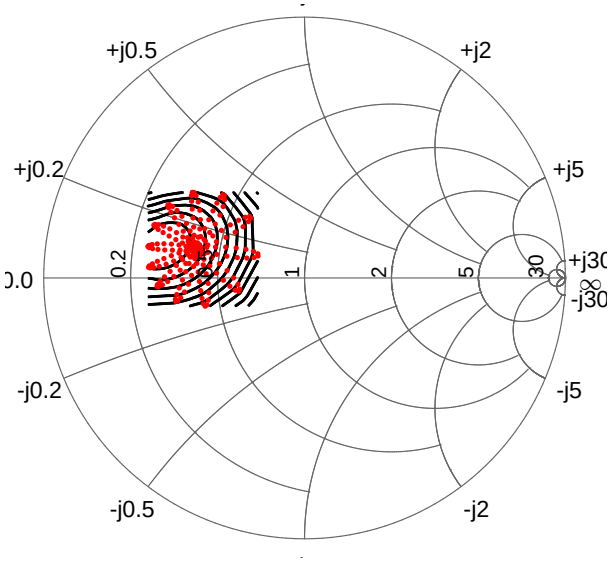

Figure 3.4: $\Gamma_{2,1}$ and the correlated power contours on the Smith Chart collected from the simulation measurement setup with 39.5 dBm as maximum output power level.

For the extrapolation ability verification, another load-pull simulation without the circulator is also performed with the same setup in Fig.3.1, to acquire a larger dataset that covers the whole Smith Chart. The collected data location for extrapolation, compared to the design-related dataset, is plotted in Fig. 3.5.

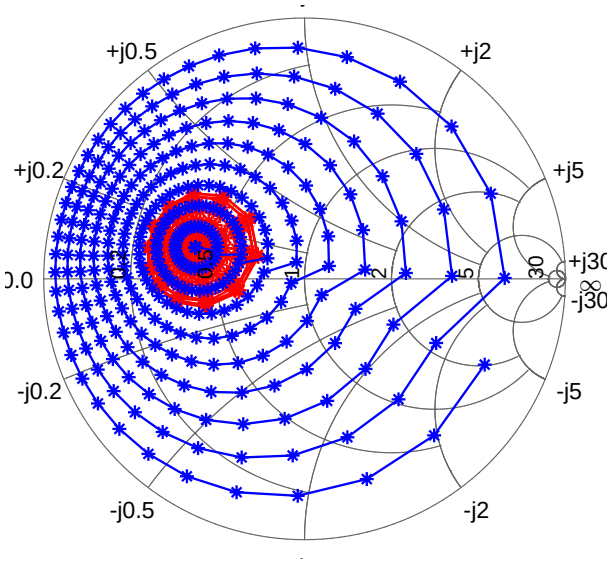

Figure 3.5: Dataset with expanded coverage on the Smith Chart for extrapolation verification (blue) and the design-related dataset (red) for model extraction.

3.2 The CM Robustness Verification

Two methods are introduced in works of literature to extract the CM coefficient: utilising user-defined model mixing order with the formal CM definition [1], and defining the model order by analysing the data complexity when a tailored dataset is available [2]. Although both methods have proven to be accurate for modelling transistor behaviour in publications, the extracted model coefficients' extrapolation ability remains to be conclusively proven. In this section, the accuracy of extracted coefficients will be presented first to ensure a correct model extraction. In addition to robustness verification, the extrapolation performance of the two methods will also be investigated.

3.2.1 CM with Conventional Mixing Theory

The formal fundamental CM equation [3], [4] is as follows in (3.5).

$$B_{p,h}\left(|A_{1,1}|\right) = Q_{1,1}^{h}\left(\sum_{r=0}^{r=\frac{(ord-h)}{2}}\sum_{n=-\left(\frac{(ord-h)}{2}-r\right)}^{n=h+\frac{(ord-h)}{2}-r} M_{p,h,m,n}\left(|A_{1,1}|\right)|A_{2,1}|^{m}\left(\frac{Q_{2,1}}{Q_{1,1}}\right)^{n}\right) \tag{3.5}$$

As explained in the literature review section for (2.15), the phase exponent parameter 'n', the magnitude restricting terms 'r', and the magnitude exponent parameter 'm' are related to the definition of $m = |n| + 2r$. 'r' indicates the magnitude restricting term, which is varied with integer steps. It is usually limited up to 1 for fundamental measurement cases [5]. '*ord*' presents the model order. '$Q_{1,1}$' and '$Q_{2,1}$' are the complex exponential of the phase of $A_{1,1}$ and $A_{2,1}$, respectively.

Following the mixing theory, the CM with the appropriate user-defined mixing order can provide accurate interpolation predictions for measurement data. According to the analysis from the study presented in [1], [6], for a set of fundamental data, a 5^{th} order CM is generally accurate enough for simulation data. Hence, in (3.5), the value of '*ord*' here is selected to be 5. The value of 'r' is restricted from 0 to 1 in integral form for the fundamental situation, 'n' and 'm' can then be calculated and listed as in Table 3.1.

The listed 'n', 'm' values are used to populate the $\left[|A_{2,1}|^{m}\left(\frac{Q_{2,1}}{Q_{1,1}}\right)^{n}\right]$ matrix in (3.6) for model coefficient extraction. The extracted CM coefficients are listed in Table 3.1 align with the related'r', 'n', and 'm' values.

$$[M_{p,h,m,n}] = \left(\left[|A_{2,1}|^{m}\left(\frac{Q_{2,1}}{Q_{1,1}}\right)^{n}\right]^{H}\left[|A_{2,1}|^{m}\left(\frac{Q_{2,1}}{Q_{1,1}}\right)^{n}\right]\right)^{-1}\left[|A_{2,1}|^{m}\left(\frac{Q_{2,1}}{Q_{1,1}}\right)^{n}\right]^{H}[B_{2,1}] \tag{3.6}$$

Table 3.1: The Extracted CM Coefficients For $B_{2,1}$ using CM with the conventional mixing theory

				$M_{2,1,m,n}$	
index	r	n	m	*Real*	*Imag.*
1	0	-2	2	0.0151	-0.0182
2	0	-1	1	-0.0462	-0.0433
3	0	0	0	3.1395	0.8942
4	0	1	1	-0.5626	-0.2590
5	0	2	2	0.0200	-0.0457
6	0	3	3	0.0009	-0.0080
7	1	-1	3	0.0049	-0.0100
8	1	0	2	0.0246	-0.0590
9	1	1	3	0.0187	-0.0108
10	1	2	4	0.0025	-0.0032

The listed CM coefficients in Table 3.1, extracted with a user-defined model order based on the conventional mixing theory, perform a Normalised Mean Square Error (NMSE) level of - 65.32 dB, which is proven accurate enough as a behavioural model [1]. The predicted results compared to the original simulated measurement data are as shown in Fig.3.6.

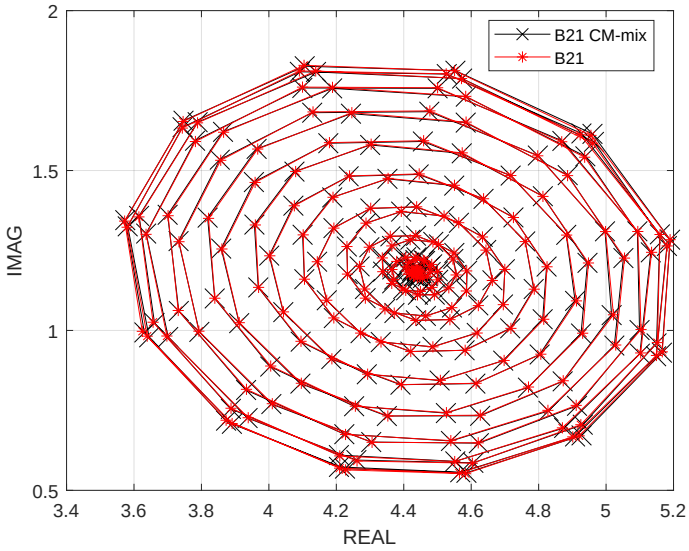

Figure 3.6: $B_{2,1}$ from measurement compare to $B_{2,1}$ CM prediction with conventional mixing theory

The expanded dataset shown in Fig. 3.5, is then applied for the extrapolation verification. The performance of the CM coefficients is presented in Fig. 3.7. Compared

to the simulation reference (Fig. 3.7-red stars), it is obvious that the extrapolation performance (Fig. 3.7-black stars) is not as accurate as the interpolated ones. An obvious distortion appears at the edge when comparing the extrapolated $B_{2,1}$ data points to the simulation results.

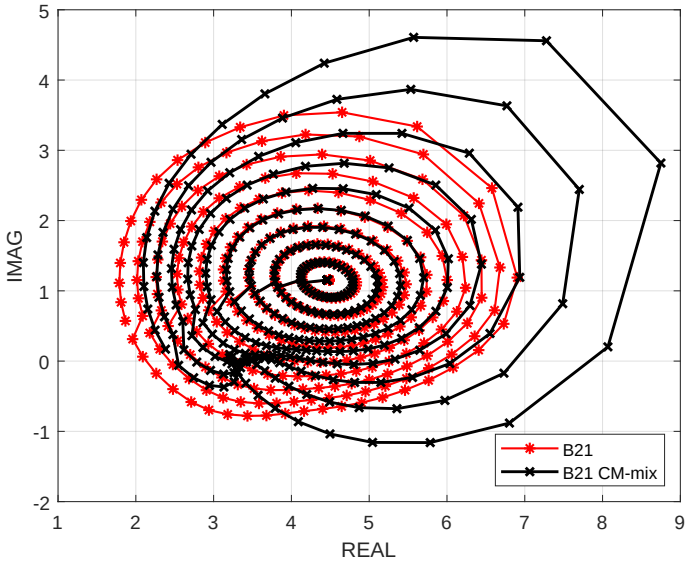

Figure 3.7: Extrapolation performance with CM extracted using conventional mixing theory (original dataset - red and the CM predictions - black).

With the response travelling wave $B_{2,1}$, the device output power can be calculated with (3.7).

$$P_{out}(dBm) = 30 + 10\log_{10}\left(\frac{1}{2}\left(|B_{2,1}|^2 - |A_{2,1}|^2\right)\right) \tag{3.7}$$

The distortion shown with the $B_{2,1}$ data points may lead to a wrong output power prediction. As shown in Fig. 3.8, the predicted power contours in black introduce a different optimum, which does not match up with the simulated reference in red. This may result in an optimizer converging on an erroneous load point when trying to optimize the matching network line parameters.

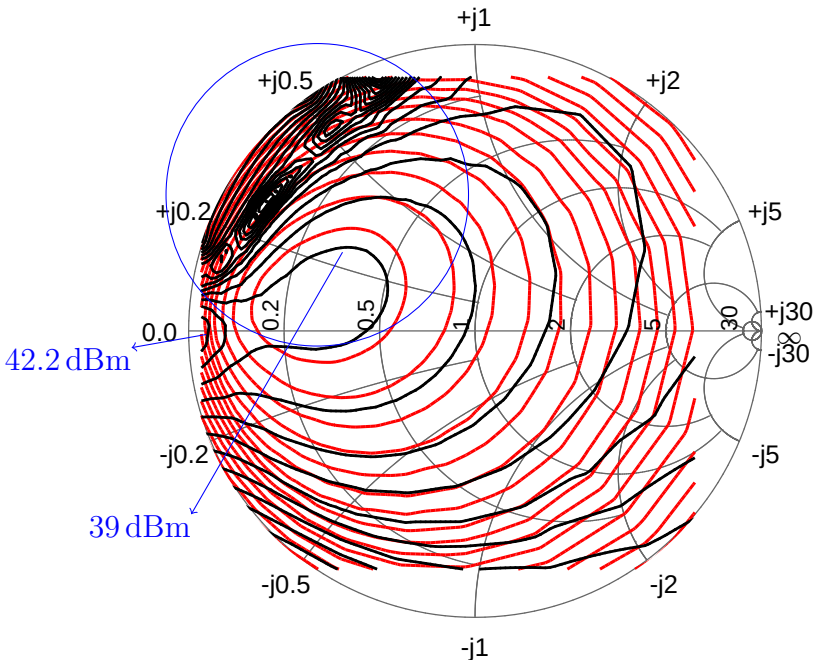

Figure 3.8: Predicted output power contours (0.4 dBm/step, black) with coefficients extracted using conventional CM mixing theory compared to the original simulated results (red).

3.2.2 CM with Tailored Dataset Analysis

In this section, the data spectrum analysis for a proper truncated CM will be implemented, together with the extrapolation ability of the extracted CM coefficients.

The user-defined CM given in the previous subsection presents with extrapolation challenge. However, this does not mean that the CM will present issues when extrapolating in general. It can be stated that a high user-defined order model allows a high model accuracy within the interpolation region, but it is very likely to cause poor extrapolation results. Further data is required out towards the edge of the Smith Chart if expecting more reasonable extrapolation predictions. This is then pointing out that a set of reasonable extrapolation results from the CM may require a properly defined mixing order. A further truncation to the polynomial formulation can be conducted by analysing the Fourier Transformed spectrum plots given by specific datasets. Under this scenario, the analysis done on tailored datasets,

explained in [2], can be helpful.

The CM can be extracted with a different procedure, where the value of the phase exponent parameter 'n', the magnitude restricting terms 'r', and the magnitude exponent parameter 'm' are defined. According to the explanation in [2], the collected $B_{2,1}$ Fourier Transformed spectrum, plotted in Fig. 3.5, can now be utilised. For a further truncated CM, as the spectrum analysis given in Fig. 3.9, 5 coefficients should be extracted here for an accurate model with the - 60 dB error threshold. With the selected exponents' value, a different CM is extracted with (3.6), and the value of the coefficients, align with the related 'r', 'n', and 'm' values, are listed in Table 3.2.

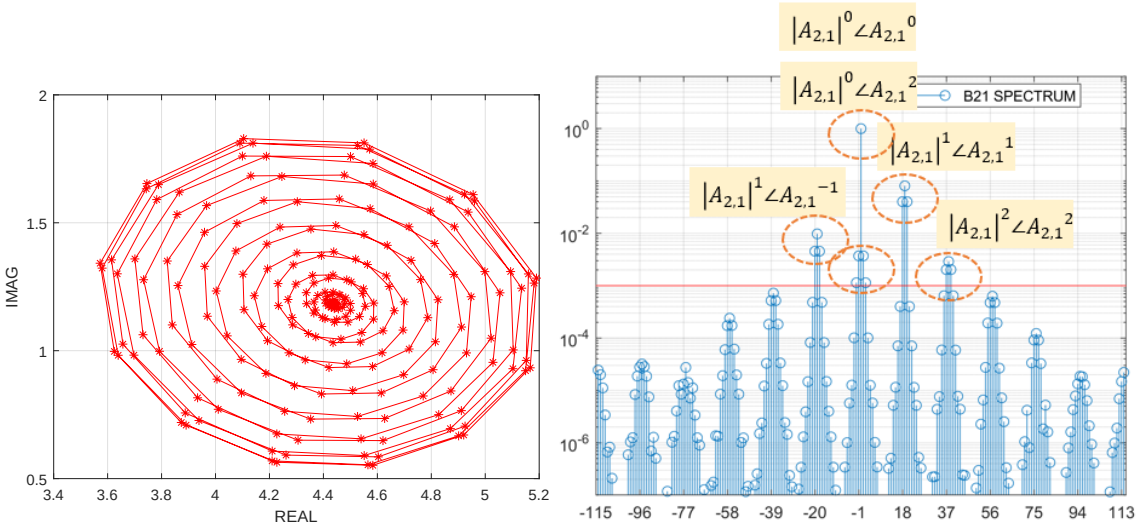

Figure 3.9: The expected exponents' $|A_{2,1}|^m(\angle A_{2,1})^n$ values of the CM for extracting coefficients in (n,m).

Table 3.2: The Extracted CM Coefficients For $B_{2,1}$ with analysis on Tailored Dataset

				$M_{2,1,m,n}$	
index	r	n	m	*Real*	*Imag.*
1	0	0	0	3.0776	0.9414
2	0	1	1	-0.6033	-0.1992
3	0	-1	1	-0.1350	0.0091
4	0	2	2	0.0108	-0.0194
5	1	0	2	-0.0393	-0.0146

The performance of the CM extracted with the tailored dataset spectrum analysis can then be visualised, an NMSE level of - 54.54 dB[1] is shown in Fig.3.10, when

comparing the predicted results to the simulation data in the measured area.

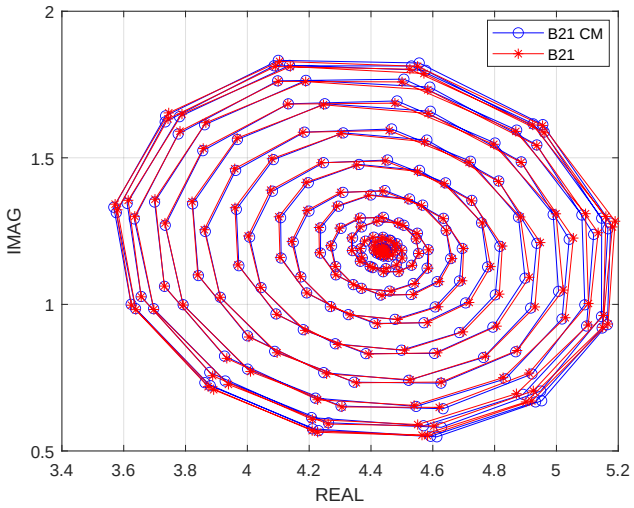

Figure 3.10: B_{21} from measurement compare to B_{21} CM prediction with analysis on tailored dataset

The values of the extracted CM coefficients are recorded then for the extrapolation verification. With the expanded dataset in Fig.3.5, the extrapolation prediction results from the CM coefficients are plotted in blue and presented in Fig. 3.11-3.12. The extrapolation performance shown with the $B_{2,1}$ data points in Fig. 3.11 has been improved, where the distortion features and erroneous predictions are not presented compared to the results shown in Fig. 3.7.

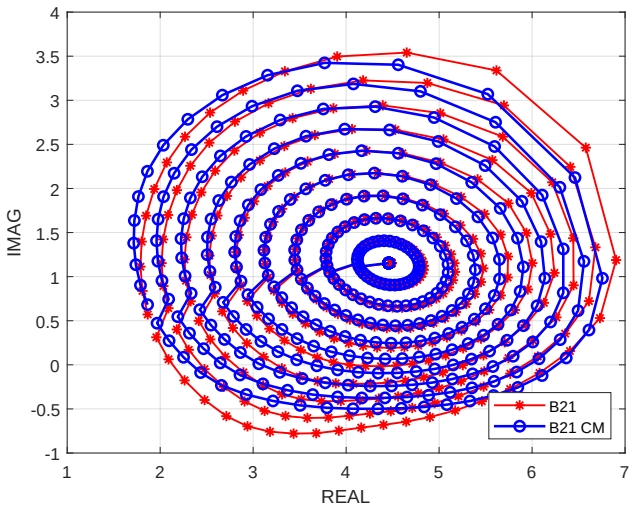

Figure 3.11: Extrapolation performance with CM extracted using analysis on tailored dataset(original dataset - red and the CM predictions - blue).

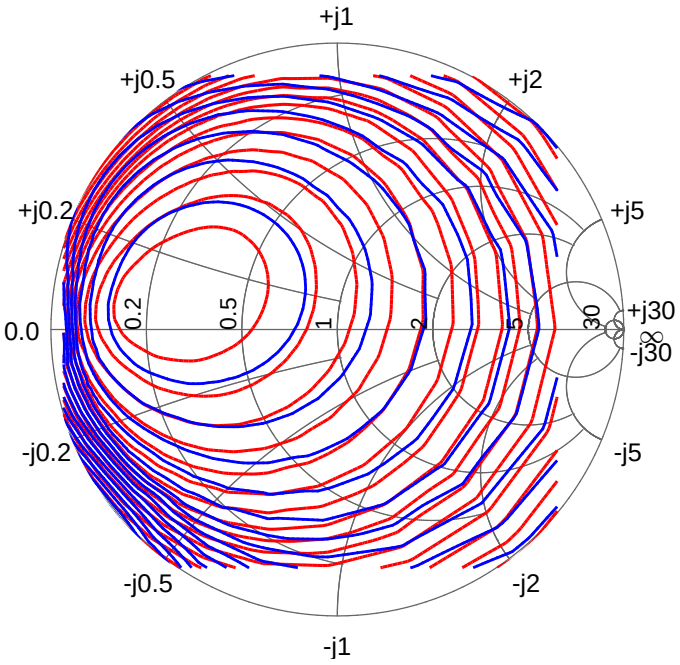

Figure 3.12: Predicted output power contours (0.4 dBm/step, blue) with coefficients extracted using the CM extracted by analysing the tailored dataset compared to the original simulated results (red).

Also, in Fig. 3.12, the erroneous contours appear to be on the short edge on the Smith Chart shown in Fig. 3.8 do not exist anymore. In reality, it is uncommon to have a good accuracy rating for the model extrapolation ability, but the simulation environment provides the possibility here for reference. The NMSE level calculated from the predicted power level compared to the simulated results is - 31.3 dB with the extracted CM coefficients.

3.2.3 Discussion on the CM

Based on the published literature, the CM presented in this section is extracted with its formal fundamental formulation in two ways: the conventional way of using user-defined order [4]; and a more robust way of using the spectral line analysis with tailored load-pull datasets [2]. It has been proven that both ways of getting the list of exponents/defining the order of the CM offer good model accuracy, when interpolating within the model extraction data range.

As a general understanding, it is reasonable to assume that higher interpolation accuracy will require a higher user-defined mixing order. However, this is not the case for model extrapolation ability. With the results shown previously, it has been proven that the extrapolation performance of the CM can be improved by properly truncating the model order according to the data complexity.

Here, a noteworthy point is that the load-pull measurement is generally restricted due to the limitations imposed by the measurement system and the constraints of transistor operation. A tailored dataset can be easily obtained from simulation, but in reality, it is not a commonly applied function to the actual measurement systems. This means that a user-defined model order will still be the trend for general CM coefficient extraction.

3.3 The ANN Solution

Literature shows that the ANN based behavioural models also provide RF designers with an efficient way to create models for assisting different design cases [7]–[11]. However, there are options for configuring a proper ANN based behavioural model under different application scenarios.

In this section, an ANN structure will be selected and illustrated first. A configured ANN model accuracy and the possibility for reasonable extrapolation performance are explored with different determined values for the parameters that are required for the selected ANN structure.

3.3.1 ANN Configuration and implementation

Previous work has shown that the Knowledge-Based Neuron Network (KBNN) structured model with the knowledge layer allows built-in knowledge to give more infor-

mation and deteriorates slowly in the model extrapolation region [12], therefore, provides a chance for the model to obtain better extrapolation results [13] compared to other feed-forward structures without the knowledge layer. When expecting an ANN model with reasonable extrapolation ability, a Fully Connected Cascaded (FCC) feed-forward neural network, can be a choice for easier implementation to start with, as a simpler version of the KBNN model when only one hidden layer is used in the neural network structure. For a complete ANN configuration, the Levenberg-Maquart training algorithm illustrated in the literature review (Algorithm 1), which achieves faster convergence compared to other gradient descent algorithms [12], is also selected to be implemented.

The implementation is done manually, without using the provided ANN toolboxes in MATLAB. In the same way as the CM, the ANN can be set to predict the pseudo-wave travelling wave from $A_{2,1}$ to $B_{2,1}$ for modelling transistor behaviour. Hence, for the ANN model, the given input is $A_{2,1}$, and the target output is $B_{2,1}$. Since the common ANN implementations do not deal with datasets in complex number format to simplify the derivative calculation, both the $A_{2,1}$ and $B_{2,1}$ are separated in real and imaginary parts in vector matrices as the input and target output of the ANN.

Fig. 3.13 presents a basic one-hidden-layer structure, where in the diagram block, the knowledge layer of the KBNN is called the cascaded layer for the FCC ANN model. '*[HN]*', '*[CN]*' and '*[ON]*' indicate the neurons in the hidden layer, cascaded layer and the output layer, respectively. '*[HW]*' and '*[HB]*' represent the hidden weight and bias matrices respectively, '*[OB]*' stands for the output bias matrix, '*[OW]*' stands for the output weight matrix, and '*[CW]*' is the cascaded weight matrix. The subscript 'N' represents the number of hidden neurons utilised in the structure. The structure can be adjusted by increasing the number of nodes or layers if necessary for the dataset during the experiment.

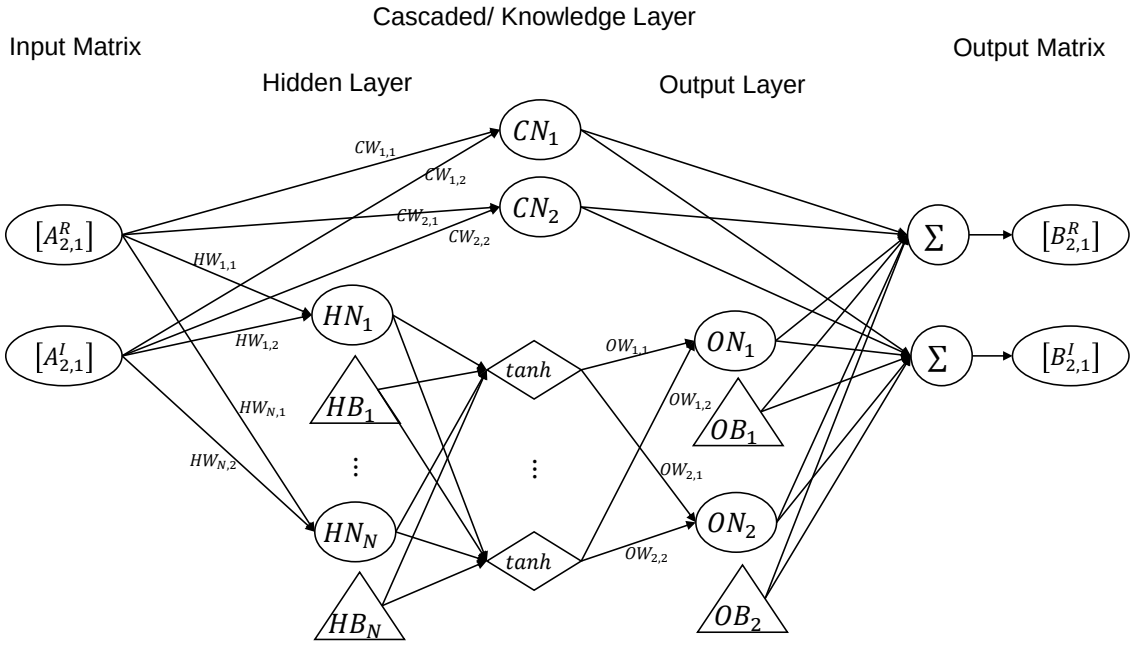

Figure 3.13: The implemented FCC structure.

The performance of the presented ANN structure can be tested by varying the correlated internal parameters,e.g., the hidden neuron numbers and the initial values of the determined weights and biases, and the predicted ANN extrapolation ability will be verified and compared.

3.3.2 The Accuracy and Extrapolation Ability of the Selected ANN Configuration

The accuracy and extrapolation ability of the selected ANN configuration are explored by varying the hidden neuron numbers and the initial weights and biases values to the backpropagation training algorithm in this section.

The datasets presented in Section 3.1, utilised for the CMs verification, are applied to evaluate the ANN model performance as well. The dataset shown in Fig. 3.2 - 3.4, which is used for the CM coefficient extraction, is applied for ANN training. The expanded dataset is shown in Fig. 3.5, blue markers, and is used for ANN extrapolation ability verification. The design-related dataset located as in Fig. 3.4

is normalised between -1 and 1 before feeding into the network training process. The scaling factor from the normalisation process of the design-related dataset is then utilised for preprocessing the expanded dataset plotted with blue markers in Fig. 3.5.

Impact of Variant Hidden Neuron Number

The value of the hidden neuron number, the subscript 'N' in Fig. 3.13, is varied between 1 to 15 for the fundamental data prediction. The model error level begins to degrade with the NMSE level falling below - 40 dB [1] at the point where the hidden neuron number equals 2. The results shown in Fig. 3.14(a) prove that it is now an accurate model, however, the extrapolation ability of the ANN with 2 hidden neurons shown in (b) is not yet satisfactory.

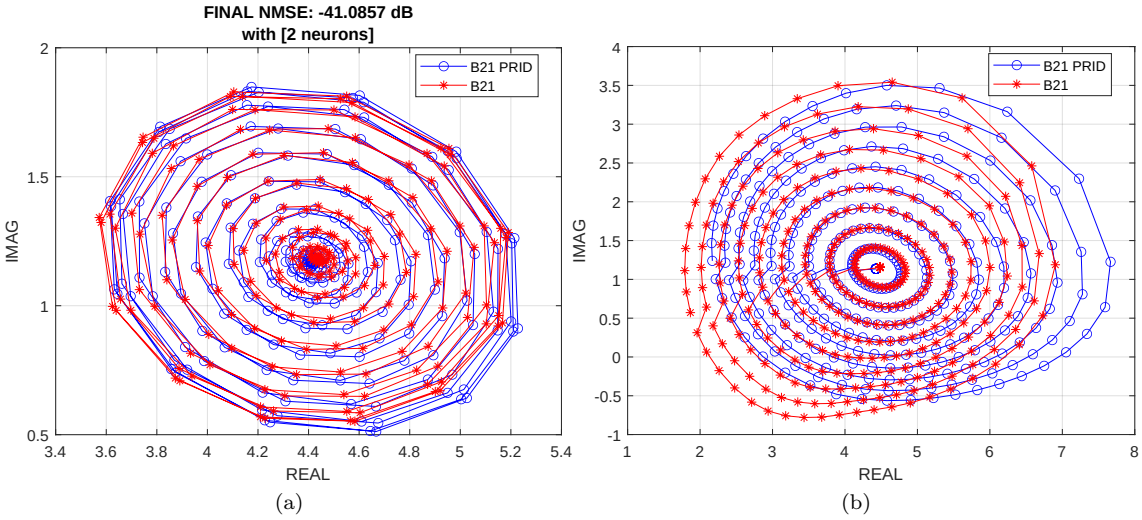

Figure 3.14: The model performance (a) and extrapolation ability (b) of the $B_{2,1}$ from measurement compared to $B_{2,1}$ prediction from ANN with 2 hidden neurons.

Experiment results show that when the hidden neuron number is varied, the model accuracy varies. Another example is shown here with the model prediction results when the hidden neuron number equals to 6 in Fig. 3.15. Here, the model accuracy (Fig. 3.15 (a)) is improved compared to the structure with 2 hidden neurons (Fig. 3.14), with the extrapolation ability also appearing marginally enhanced (Fig. 3.15

(b)).

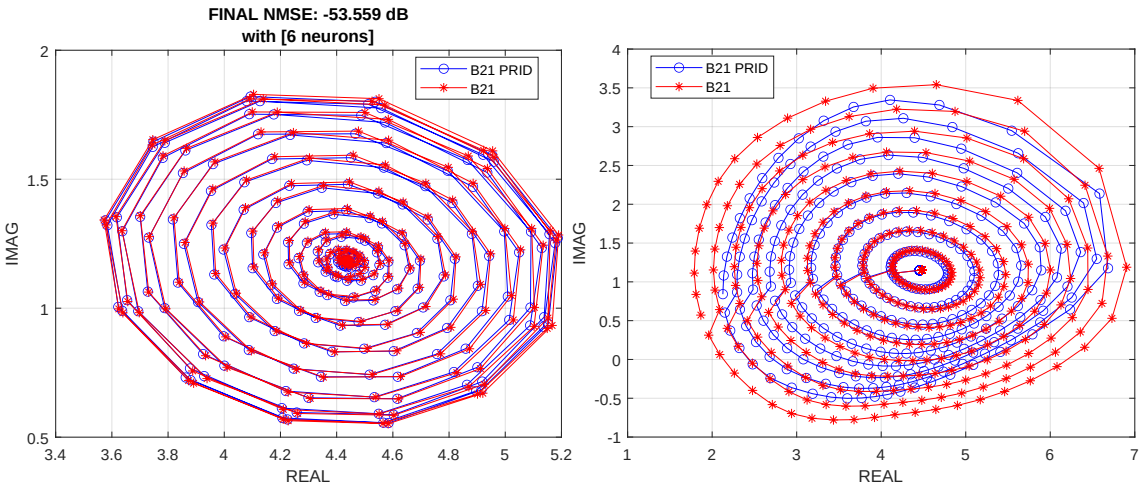

(a) (b)

Figure 3.15: The model performance (a) and extrapolation ability (b) of the $B_{2,1}$ from measurement compared to $B_{2,1}$ prediction from ANN with 6 hidden neurons.

If drawing a step-wise conclusion at this stage, it appears that the results confirm that when the hidden neuron number increases, the model performance will improve.

Alternatively, when the hidden neuron number is increased to 11, it can be seen from Fig. 3.16 that the model accuracy decreases compared to the structure with 6 hidden neurons. However, a better extrapolation is presented when matching the extrapolated $B_{2,1}$ predictions to the simulation. Given that apart from the hidden neuron number, there are still other internal parameters to be varied in the ANN configuration process, the reason for the decrease of model accuracy is not considered at this stage.

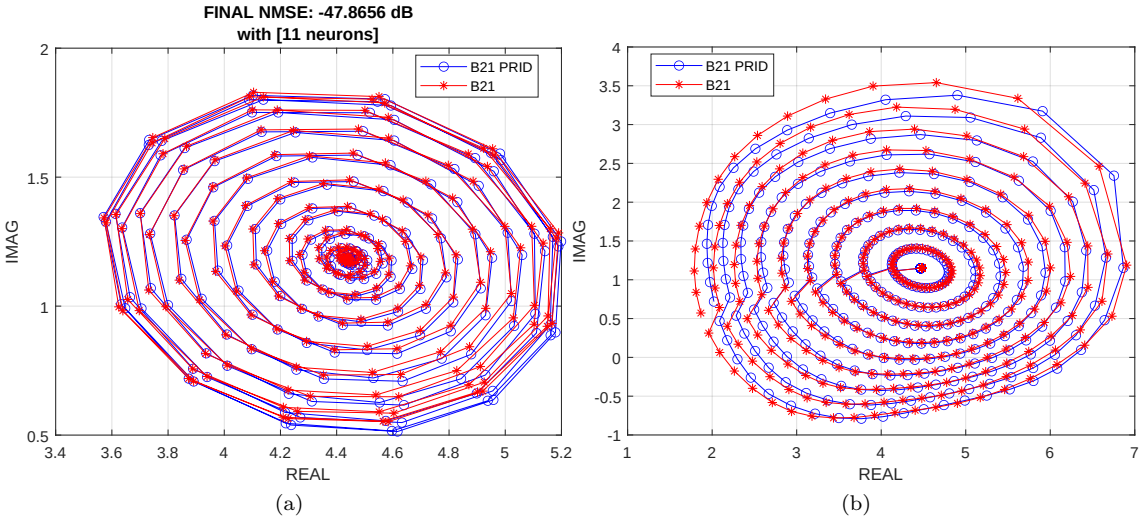

Figure 3.16: The model performance (a) and extrapolation ability (b) of the $B_{2,1}$ from measurement compared to $B_{2,1}$ prediction from ANN with 11 hidden neurons.

The improved extrapolation prediction can also be visualised in Fig. 3.17, where the predicted power contours are well presented with no erroneous features shown on the edge of the Smith Chart. The NMSE level provided by the ANN model compared to the simulation is - 37 dB with 11 hidden neurons. It is an accurate extrapolation [1], even better than the results given by the CM extracted with the tailored dataset shown in the previous section (Fig. 3.12).

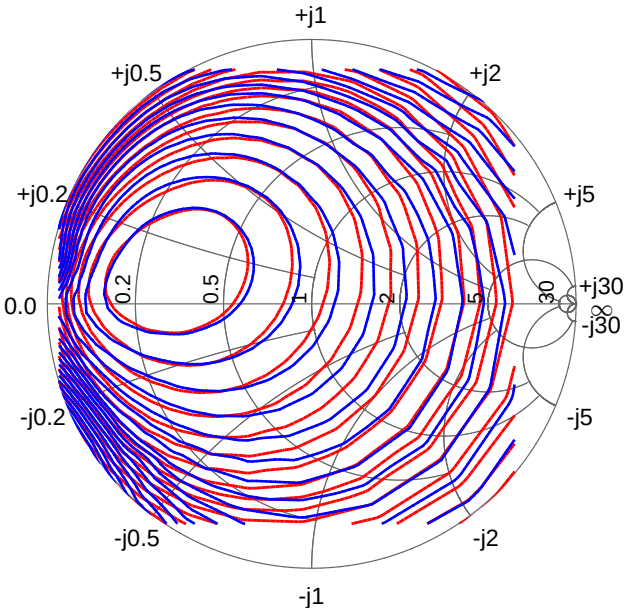

Figure 3.17: Extrapolated output power contours (blue) with 11-hidden-neuron ANN structure compared to the original simulated results (red).

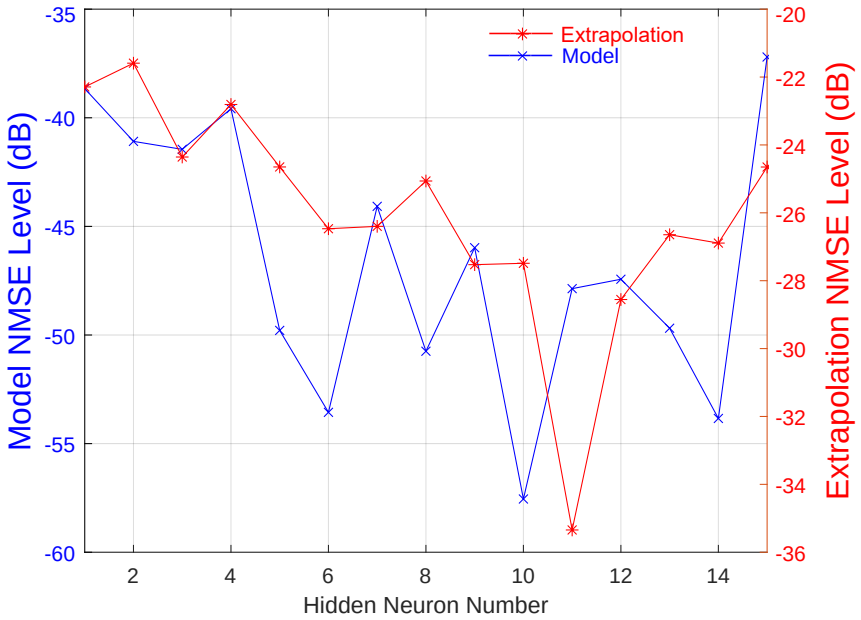

Figure 3.18: The model accuracy and extrapolation performance summary of the ANN structure with different hidden neuron numbers.

A summary plot is provided for an overview of the relationship between the model accuracy and extrapolation ability when the hidden neuron number is varied. As shown in Fig. 3.18, when sweeping the hidden neuron numbers from 1 to 15, the accuracy varies. The levels of the calculated NMSE, when the model predictions are compared to the simulation data, mainly remain around - 40 dB, which is a sufficiently accurate level for RF design requirements [1]. However, the extrapolation performance also varies, and is not correlated to the model accuracy. It can be seen that, for instance, even when the accuracy increases, the performance of the extrapolation does not always increase to the same degree.

Impact of Weights and Biases Initialisation

It is mentioned in [12] that the LM training algorithm performance depends on the initial estimation of weights and biases values of the ANN. The testing experiment started with a random number generator, and the initial values of all the weights and biases are assigned randomly.

Given the results from the previous section that show how 11 hidden neurons enable

an ANN model that allows both accurate interpolation and reasonable extrapolation prediction, here, the ANN model with 1 hidden layer and 11 hidden neurons is tested under different initial weights and biases values scenarios.

In the implemented LM training algorithm, the initial values for the weights and biases are generated with a Mersenne Twister random number generator [14]–[16]. Previously for testing the impact of different hidden neuron numbers, the seed of the random number generator is given as 10 (default setting in MATLAB) to initialise the values of the weights and biases. Here, the value of the random number generator seed is changed from 10 to 15 (a randomly selected number) for a different set of initial weights and biases values, to show how the ANN will perform with different starting points. The results shown in Fig. 3.19 indicate a similar model accuracy, however, a significantly different extrapolation result.

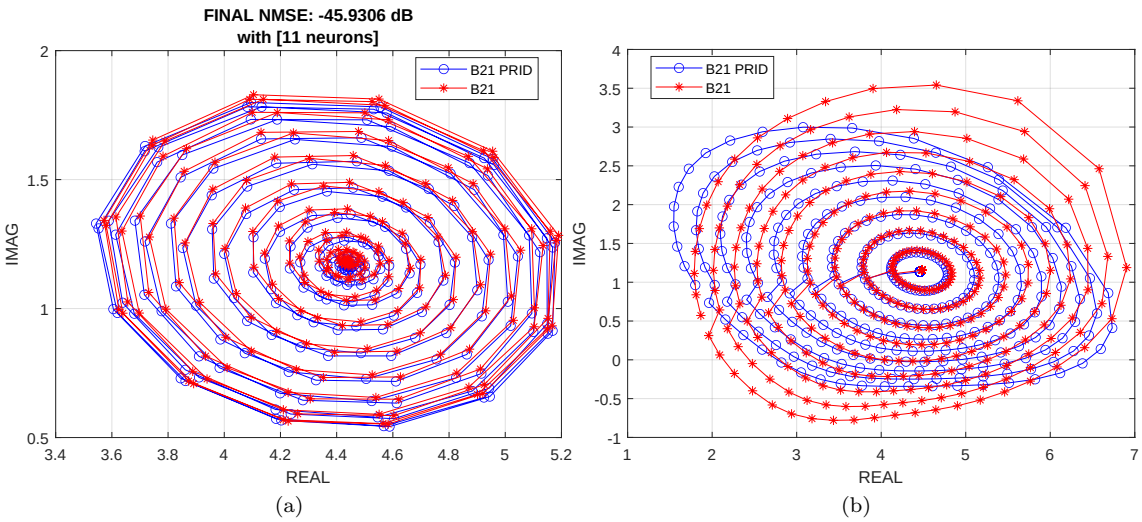

Figure 3.19: The model performance (a) extrapolation ability (b) of the $B_{2,1}$ from measurement compared to $B_{2,1}$ prediction from ANN with 11 hidden neurons and the random number generator seed changed to 15.

The extrapolation performance can be more easily visualised in Fig. 3.20. Different from the prediction results offered by the ANN model trained with the random initial number generator using 10 as the value of the seed, shown in the previous section, the erroneous features on the short edge of the Smith Chart appear again when the value of the seed is changed to 15.

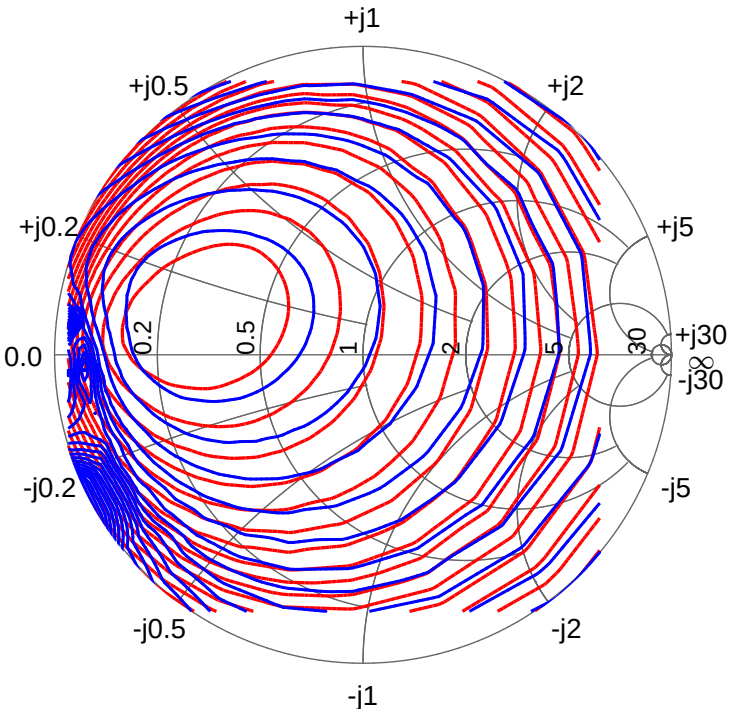

Figure 3.20: Extrapolated output power contours (blue) with CM extracted using the CM extracted by analysing the tailored dataset compared to the original simulated results (red).

3.3.3 Discussion on the ANN Model

The results indicate that the ANN model accuracy can be independent of specific measurement datasets, and a properly defined ANN model can provide reasonable extrapolation results. When changing the number of hidden neurons and the initial weights and bias values, both will make differences to the ANN model performance. This happens not only to the interpolation accuracy but also to the extrapolation ability. However, the correlation between the two factors and the model performance seems irregular. Increasing the number of hidden neurons does not guarantee a more accurate model. Simultaneously, an ANN model that is accurate for interpolation does not always result in comparable extrapolation ability. Therefore, a procedure to define a proper ANN structure that forms an accurate model with acceptable extrapolation ability is demanding.

On the other hand, the ANN offers more flexibility in model structure correlating

to the model accuracy when compared to the CM. However, it may require multiple attempts or potentially rely on experience for a properly defined structure, such as a proper number of hidden neurons, and proper initial values of the weights and biases, which can potentially be time-consuming.

3.4 Conclusion

In the first part of this Chapter, two CMs, extracted using different order definitions, are illustrated, verified, and compared. It is proven that the tailored dataset provides a proper truncation method to the polynomial order, which then helps improve the model extrapolation ability.

The second part presents an implementation and analysis of the selected FCC ANN structure with the LM training algorithm. An ANN based one-hidden-layer model is able to capture the nonlinear relationships between the input and output under fundamental frequency and provide an accurate model with good extrapolation ability, with proper hidden neuron numbers and initial weights and bias values.

Both the CM and the ANN models allow accurate behavioural models with reasonable extrapolation ability when required model parameters are properly defined. This can then enable further experiments to explore the possibility for models with reasonable extrapolation ability that can be extracted and utilised efficiently.

References

[1] M.R. Moure, M. Casbon, M. Fernández-Barciela, P.J. Tasker, "A Systematic Investigation of Behavioural Model Complexity Requirements," in *2018 13th European Microwave Integrated Circuits Conference (EuMIC)*, Madrid, Spain, Sep. 2018, pp. 77–80. DOI: 10.23919/EuMIC.2018.8539950.

[2] P.J. Tasker, "Robust Extraction of Cardiff Model Parameters from Appropriately Tailored Measured Load-Pull Data," in *2020 IEEE BiCMOS and Compound Semiconductor Integrated Circuits and Technology Symposium (BCICTS)*, Monterey, CA, USA, Nov. 2020, pp. 1–5. DOI: 10.1109/BCICTS48439.2020.9392942.

[3] H. Qi, J. Benedikt, P.J. Tasker, "Nonlinear Data Utilization: From Direct Data Lookup to Behavioral Modeling," *IEEE Transactions on Microwave Theory and Techniques*, vol. 57, no. 6, pp. 1425–1432, Jun. 2009. DOI: 10.1109/TMTT.2009.2019996.

[4] P.J. Tasker, "Practical waveform engineering," *IEEE Microwave Magazine*, vol. 10, no. 7, pp. 65–76, Dec. 2009. DOI: 10.1109/MMM.2009.934518.

[5] P.J. Tasker, J. Benedikt, "Waveform Inspired Models and the Harmonic Balance Emulator," *IEEE Microwave Magazine*, vol. 12, no. 2, pp. 38–54, Apr. 2011. DOI: 10.1109/MMM.2010.940101.

[6] M.R. Moure, M. Casbon, M. Fernández-Barciela, P.J. Tasker, "Direct extraction of an admittance domain behavioral model from large-signal load-pull measurements," in *2017 IEEE MTT-S International Microwave Symposium (IMS)*, Honololu, HI, USA, Jun. 2017, pp. 1057–1060. DOI: 10.1109/MWSYM.2017.8058775.

[7] V.K. Devabhaktuni, C. Xi, F. Wang, Q.J. Zhang, "Robust training of microwave neural models," in *1999 IEEE MTT-S International Microwave Symposium Digest (Cat. No.99CH36282)*, vol. 1, Anaheim, CA, USA, Jun. 1999, 145–148 vol.1. DOI: 10.1109/MWSYM.1999.779444.

[8] J. Wood, D.E. Root, *Fundamentals of nonlinear behavioral modeling for RF and microwave design* (Artech House microwave library), eng. Boston, Mass. ; Artech House, 2005, ISBN: 9781580537759.

[9] J. Cai, J. Wang, C. Yu, H. Lu, J. Liu, L. Sun, "An artificial neural network based nonlinear behavioral model for RF power transistors," in *2017 IEEE Asia Pacific Microwave Conference (APMC)*, Kuala Lumpur, Malaysia, Nov. 2017, pp. 600–603. DOI: 10.1109/APMC.2017.8251517.

[10] J. Louro, C. Belchior, D.R. Barros, "New Transistor Behavioral Model Formulation Suitable for Doherty PA Design," *IEEE Transactions on Microwave Theory and Techniques*, vol. 69, no. 4, pp. 2138–2147, Apr. 2021. DOI: 10.1109/TMTT.2021.3054645.

[11] F. Feng, W. Na, J. Jin, J. Zhang, W. Zhang, Q.-J. Zhang, "Artificial Neural Networks for Microwave Computer-Aided Design: The State of the Art," *IEEE Transactions on Microwave Theory and Techniques*, vol. 70, no. 11, pp. 4597–4619, Nov. 2022. DOI: 10.1109/TMTT.2022.3197751.

[12] Q. -J. Zhang, K. C. Gupta, *Neural Networks for RF and Microwave Design*. Boston, MS, USA: Artech House, 2000.

[13] W. Fang, Q.J. Zhang, "Knowledge based neural models for microwave design," in *1997 IEEE MTT-S International Microwave Symposium Digest*, vol. 2, Denver, CO, USA, Jun. 1997, 627–630 vol.2. DOI: 10.1109/MWSYM.1997.602870.

[14] M. Matsumoto, T. Nishimura, "Mersenne twister: a 623-dimensionally equidistributed uniform pseudo-random number generator," *ACM Transactions on Modeling and Computer Simulation (TOMACS)*, vol. 8, no. 1, pp. 3–30, Jan. 1998, ISSN: 1049-3301. DOI: 10.1145/272991.272995. [Online]. Available: https://doi.org/10.1145/272991.272995.

[15] G. Marsaglia, W.W. Tsang, "The Ziggurat Method for Generating Random Variables," *Journal of Statistical Software*, vol. 5, no. 8, pp. 1–7, Aug. 2000. DOI: 10.18637/jss.v005.i08. [Online]. Available: https://www.jstatsoft.org/index.php/jss/article/view/v005i08.

[16] Inc. T. M., *Creating and Controlling a Random Number Stream*, Natick, Massachusetts, United States. [Online]. Available: https://uk.mathworks.com/help/matlab/math/creating-and-controlling-a-random-number-stream.html.

Chapter 4

Artificial Neural Network (ANN) Based Cardiff Model (CM) Coefficients Extraction Approach

According to the analysis shown in the previous chapter, the Artificial Neural Network (ANN) model provides better extrapolation ability and flexibility for varying model accuracy than the Cardiff Model (CM), regardless of specific measurement datasets. However, the CM without redundant calculations in commercial RF design-related software can take less runtime than that of the ANN model [1]. Therefore, the advantages of the two models, the CM and the ANN technique, can be combined for an accurate behavioural model to be efficiently processed in CAD environment with enhanced extrapolation ability.

This chapter will present an ANN-based CM coefficients extractor, and a method that combines the conventional ANN behavioural model and the coefficient extractor, to ensure reasonable extrapolation behaviour for highly user-defined CM coefficients. The reason that the decision is made to extract a set of CM coefficients with the aid of an ANN structure when combining the two modelling techniques

is illustrated first. A modified Levenberg–Marquardt (LM) algorithm that enables the combination of the CM coefficients extraction process with ANN technique is implemented. The accuracy of the modified LM algorithm applied with different FCC feedforward ANN structures for different datasets will be verified, under both simulation and practical scenarios. For high user-defined order CM coefficients that allow reasonable extrapolation ability, the combination method for the conventional A-B wave-based ANN model (explored in Chapter 3) and the ANN-based CM coefficients extractor is explained. The prediction results from the proposed method are expected to provide novel sets of extracted high-order CM coefficients with both accurate interpolation and reasonable extrapolation ability. Two sets of measurement data will be applied to the verification process, for proving robustness in the proposed coefficient extraction method.

4.1 Complexity Comparison of the CM and ANN models

The statement that is given in [1] about the CM implementation in the CAD environment is more efficient than the ANN can be further justified with the model complexity comparison with the required number of coefficients.

The results shown in Chapter 3 proved that the Fully Connected Cascade (FCC) ANN structure allows accurate models for the RF device in an ideal simulation environment, and simultaneously, enables reasonable extrapolation prediction when the ANN is properly structured. The mathematical expression of the one-hidden-layer FCC feedforward ANN structure in Fig. 3.13, can be presented in the following implementation formula (4.1) when utilising in CAD environment.

$$\begin{bmatrix} B^R_{p,h} \\ B^I_{p,h} \end{bmatrix} = [OB(2\times 1)] + [CW(2\times 2)] \begin{bmatrix} A^R_{2,1} \\ A^I_{2,1} \end{bmatrix} + [OW(2\times 2)] \tanh \left([HW(N\times 2)] \begin{bmatrix} A^R_{2,1} \\ A^I_{2,1} \end{bmatrix} + [HB(N\times 1)] \right) \tag{4.1}$$

where 'R' and 'I' are the abbreviations of real and imaginary complex data components. The subscript 'HN' represents the number of hidden neurons, while 'HW', 'HB', 'CW', 'OW', and 'OB' are representing the number of hidden weights, hidden biases, cascade weights, output weights, and output biases respectively, and the tanh function is presented with (2.29).

To evaluate the equation (4.1) with the given two inputs and two outputs network, the weights and biases matrices dimension are given to the matrices in the equation as: '$[HW(N\times 2)]$', '$[HB(N\times 1)]$', '$[OW(2\times 2)]$', '$[CW(2\times 2)]$' and '$[OB(2\times 1)]$', where 'N' represents the hidden neuron number. At least 13 coefficients will be required for a complete FCC ANN structure when the number of hidden neurons is chosen to be 1, regardless of the model accuracy. Increasing the number of neurons and layers in the ANN structure will be required to achieve an accurate model depending on the complexity of the dataset. For a system with stronger non-linearity, the number of hidden neurons or layers will need to be increased, which will then greatly increase the complexity of the structure.

Comparing the number of coefficients to the Cardiff model, the changes will only be required on the value and the number of the coefficients with a defined process. Generally for an accurate CM, 5^{th} order model complexity will be sufficient [2], which will then refer to 10 coefficients in total.

The relationship between the runtime and the number of coefficients is illustrated in [1]. As the number of coefficients increases, the runtime for both models rises. A direct linear relationship is presented between the runtime and the number of hidden neurons for the ANN structure. Differing from a direct linear relationship,

the runtime of the CM demonstrates a step-shaped kind of growth correlated to the increase of polynomial order. When the system complexity increases, the CM takes less runtime compared to the ANN structure. Therefore, when combining the CM and ANN technique for an efficient model, the CM is considered to be the extracted model structure rather than the ANN, which can then be efficiently processed in CAD, while also retaining extraction flexibility.

4.2 Proposed Algorithm Implementation and Verification

If choosing the CM as the extracted model combined with the ANN technique, instead of having the model input and output as the injected $A_{p,h}$ waves and the response travelling wave $B_{p,h}$ of the ANN model, the model input and output need to be both the A and B waves and the CM coefficients. However, under the supervised learning category, the ANN model requests target outputs for the error backpropagation to update the weights and biases. When the CM coefficients are the expected output from the ANN model, the target output that is required for the ANN training procedure as a reference is not available. Therefore, modification of the training algorithm will be necessary.

4.2.1 Algorithm Modification

The conventional Levenberg-Marquardt algorithm flows as in Fig.4.1 [3], according to the summarised algorithm process procedure as shown in Algorithm 1 illustrated in Chapter 2. The given target output to the ANN training process will be utilised in the error calculation for MSE_1, absolute error and MSE_2 in the back-propagation flow. When target output is not available, in this case, modifications that combine with the CM for the error calculation are required.

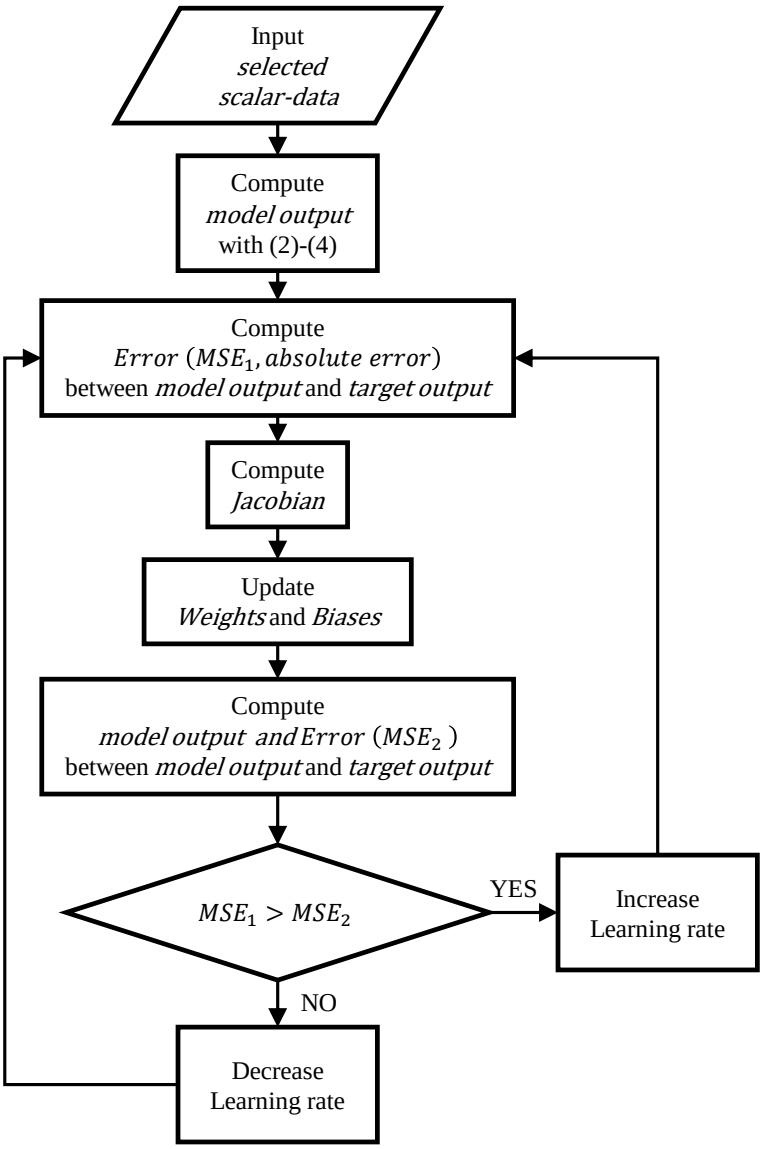

Figure 4.1: Proposed method summarized flow diagram.

According to the CM coefficient extraction formulation, the response travelling wave $B_{2,1}$ can alternatively be the intermediate variable, which is available. Hence, the error calculation for the half sum of mean square error MSE_1, MSE_2 and the internal absolute error can be modified as in (4.2) - (4.4). Then, when the target and model output in Fig.4.1 is going to be a set of coefficients, which is unknown from the starting point of the back-propagation, the required error factors can be calculated through the modelled $B_{2,1}$ with the CM formulation.

$$\boldsymbol{B}_{p,h\_\mathbf{Error}} = \boldsymbol{B}_{p,h\_Modelled} - \boldsymbol{B}_{p,h\_Measured} \tag{4.2}$$

$$\boldsymbol{B}_{p,h\_\mathbf{Modelled}} = \sum_{\mathbf{r}} \sum_{\mathbf{n}} M_{p,h,m,n} \times [\boldsymbol{A}] \tag{4.3}$$

$$\boldsymbol{M}_{p,h,m,n\_Error} = \left([\boldsymbol{A}]^H [\boldsymbol{A}] \right)^{-\mathbf{1}} [\boldsymbol{A}]^H [\boldsymbol{B}_{p,h\_\mathbf{Error}}] \tag{4.4}$$

$$\mathbf{MSE} = \frac{\mathbf{1}}{\mathbf{2}} \sum_{\mathbf{i=1}}^{\mathbf{N}} (\boldsymbol{M}_{p,h,m,n\_Error})^{\mathbf{2}} \tag{4.5}$$

where in (4.3) and (4.4), the '$[\boldsymbol{A}]$' matrix is '$|A_{2,1}|^m (Q_{2,1})^n$' populate with the (m, n) exponent pairs corresponding to the complex exponential of the magnitude and phase of $A_{2,1}$, provided by the CM normalised to the phase of $A_{1,1}$ as in follows:

$$B_{p,h} = \left(\sum_{0}^{r} \sum_{n=-\left(\frac{(ord-h)}{2}-r\right)}^{n=h+\frac{(ord-h)}{2}-r} M_{p,h,m,n} |A_{2,1}|^m (Q_{2,1})^n \right) \tag{4.6}$$

The values of coefficients '$\boldsymbol{M}_{p,h,m,n}$' can be generated by random number generators initially, and the '$\boldsymbol{M}_{p,h,m,n\_Error}$' represents the inferred error matrix of the coefficients with 'p' and 'h' denoting the respective port, harmonic; 'm' and 'n' are the magnitude and phase exponents related as $m = |n| + 2r$, 'r' is the magnitude indexing term. With the modified error calculation steps, the user-defined input matrix of the ANN model has been replaced by a matrix made up of the real and imaginary parts of both $A_{2,1}$ and $B_{2,1}$, instead of $A_{2,1}$ only.

Details of the modified back-propagation Levenberg-Marquart Algorithm [3], [4] used for the ANN based CM coefficient extractor is written as Algorithm 2.

Algorithm 2 Modified Steps of Levenberg-Marquart Algorithm for CM Coefficients Extractor

INPUT: $\boldsymbol{A}_{2,1\_Measured}, \boldsymbol{B}_{p,h\_Measured}$
  $[\boldsymbol{A}] = (\angle \boldsymbol{A}_{1,1})^h \left|\boldsymbol{A}_{2,1\_Calculated}\right|^m \left(\frac{\angle \boldsymbol{A}_{2,1}}{\angle \boldsymbol{A}_{1,1}}\right)^n$
  Initialise: $[\boldsymbol{W}_i], [\boldsymbol{B}_i] \leftarrow rand[-1, 1]$
  for *epoch* $= 1$
  $\boldsymbol{M}_{p,h,m,n} = [\boldsymbol{W}_i][\boldsymbol{A}_{\mathbf{2,1}\_Measured}, \boldsymbol{B}_{p,h\_Measured}] + [\boldsymbol{B}_i]$
  $\boldsymbol{B}_{p,h\_\mathbf{Modelled}} = \sum_{\mathbf{r}} \sum_{\mathbf{n}} M_{p,h,m,n} \times [\boldsymbol{A}]$
  $\boldsymbol{B}_{p,h\_\mathbf{Error}} = \boldsymbol{B}_{p,h\_\mathbf{Modelled}} - \boldsymbol{B}_{p,h\_Measured}$
  $\boldsymbol{M}_{p,h,m,n\_Error} = \left([\boldsymbol{A}]^H [\boldsymbol{A}]\right)^{-\mathbf{1}} [\boldsymbol{A}]^H [\boldsymbol{B}_{p,h\_\mathbf{Error}}]$
  Compute ***Jacobian***
  Update: $[\boldsymbol{W}_i]$ *and* $[\boldsymbol{B}_i]$ *till required error level met*
  end for
OUTPUT: $\boldsymbol{M}_{p,h,m,n}$

where $[\mathbf{W_i}]$ and $[\mathbf{B_i}]$ represent the weight and bias matrices that are required in the ANN model structure.

4.2.2 Invented Coefficients Extractor Verification

The modified LM training algorithm can be applied with the selected FCC ANN structure, as an invented CM coefficient extractor. Before exploring the possible utilisation of the invented extractor, it is firstly verified with the simulated load-pull measurement data acquired from the Wolfspeed 10 W gallium nitride (GaN) device. Then, a practical load-pull measurement is set up for the same device, for acquiring datasets for verifying the invented coefficient extractor in the practical scenarios. The performance of the invented extractor will be presented with both the output power and efficiency contours on the Smith Chart in this section.

Knowing from the analysis given in Fig. 3.9, 5 coefficients are required for the simulated load-pull data of the Wolfspeed 10 W GaN device. For this dataset, one hidden layer FCC ANN with a 3-hidden-neuron structure is selected and applied With the modified LM training algorithm (Algorithm 2). According to the matrix dimension required from the algorithm, the input and output matrix for extracting coefficients is different from the conventional A-B wave-based ANN model structure as Fig. 3.13.

When the input matrix is modified for a coefficient extractor, the diagram complexity dramatically increases. Hence, the ANN structure in Fig. 4.2 is generated based on the matrices format.

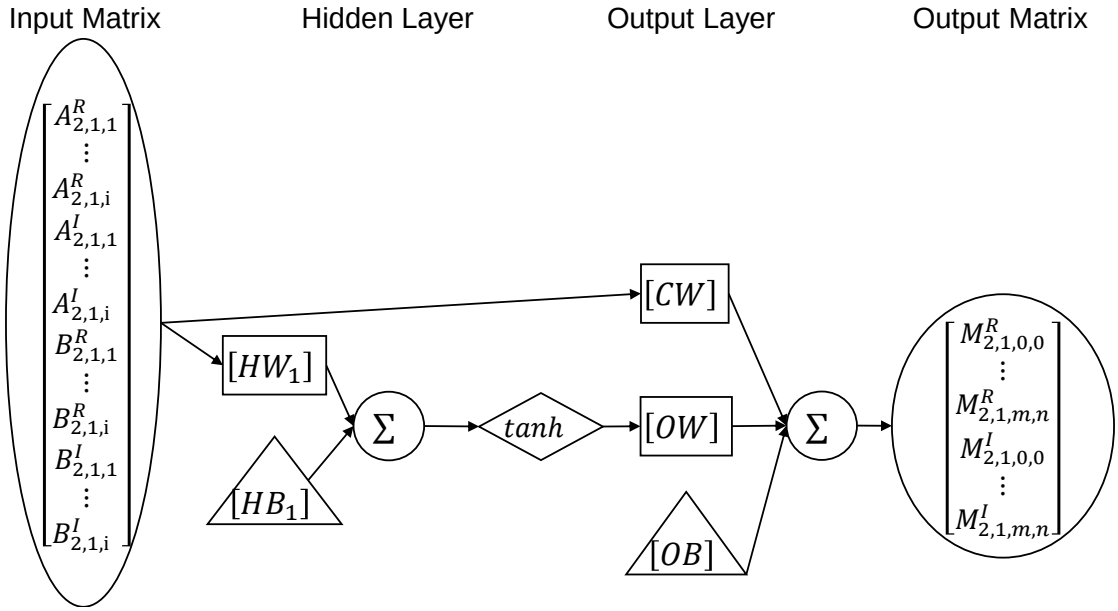

Figure 4.2: One hidden layer FCC feedforward ANN based CM coefficient extractor structure.

Here in the diagram, 'i' indicates the total number of measurement points.

The coefficients extracted by the invented ANN based coefficient extractor are listed alongside the original CM coefficients in Table 4.1. With the extracted coefficients,

Table 4.1: The Extracted Coefficients Comparison For Simulated $B_{2,1}$ of the Wolfspeed Device Using Different Techniques

				$M_{2,1,m,n}$			
				Conventional CM		ANN Extractor	
index	*r*	*n*	*m*	*Real*	*Imag.*	*Real*	*Imag.*
1	0	0	0	3.0776	0.9414	3.0776	0.9414
2	0	1	1	-0.6033	-0.1992	-0.6033	-0.1993
3	0	-1	1	-0.1350	0.0091	-0.1350	0.0090
4	0	2	2	0.0108	-0.0194	0.0108	-0.0194
5	1	0	2	-0.0393	-0.0146	-0.0393	-0.0147

$B_{2,1}$ predictions can be calculated with the CM formulation, and the output power predictions can also be calculated from correlated $A_{2,1}$ and $B_{2,1}$ predictions with (3.7).

The experiments done in Chapter 3 did not contain the analysis of the device DC response. This is because, when $B_{2,1}$ predictions come with erroneous features, the subsequent efficiency predictions will inevitably encounter problems. However, as a first step in verifying an invented method, the accuracy should be validated for all the possible prediction requirements.

The $B_{2,0}$ wave, which is the drain DC current from the same Wolfspeed device load-pull simulation, is utilised here to obtain the efficiency contours for the invented coefficient extractor accuracy verification. Analysis of the $B_{2,0}$ Fourier Transformed spectrum [5] is done for the required exponent values of the CM coefficients extraction process. As shown in Fig. 4.3(b), 6 coefficients will be required for this level of data complexity to obtain an accurate model.

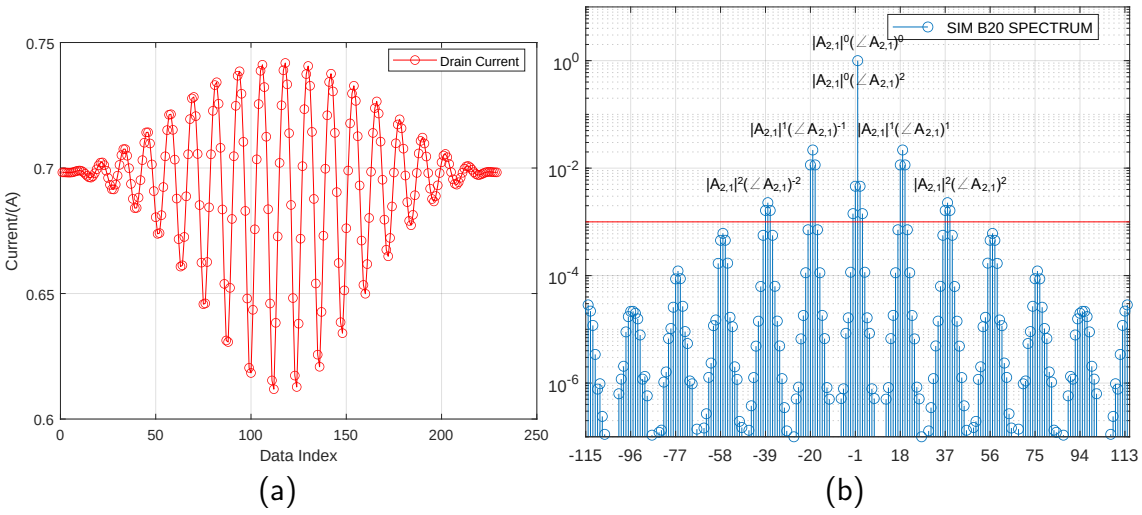

Figure 4.3: The expected exponents' $|A_{2,1}|^m(\angle A_{2,1})^n$ values (b) of the CM for extracting coefficients in (n,m) for the drain DC current $B_{2,0}$ (a) from the Wolfspeed device load-pull simulation.

Here, a linear ANN structure (as in Fig. 4.4) without hidden layers is implemented, for modelling the DC characteristic. The coefficients extracted by the invented ANN based coefficient extractor are listed alongside the original CM coefficients in Table 4.2.

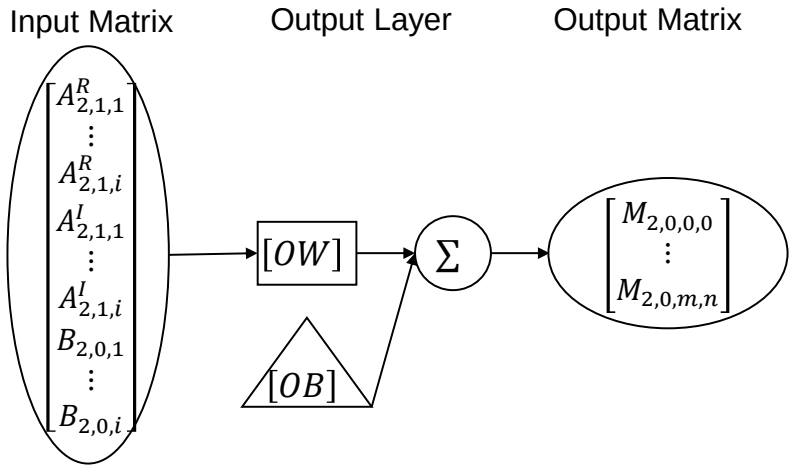

Figure 4.4: Linear FCC feedforward ANN based CM coefficient extractor structure for modelling the drain DC current $B_{2,0}$.

Table 4.2: The Extracted Coefficients Comparison For Simulated $B_{2,0}$ of the Wolfspeed Device Using Different Techniques

				$M_{2,0,m,n}$			
				Conventional CM		ANN Extractor	
index	*r*	*n*	*m*	*Real*	*Imag.*	*Real*	*Imag.*
1	0	0	0	0.7255	0	0.7255	0
2	0	1	1	0.0028	0.0141	0.0028	0.0141
3	0	-1	1	0.0028	-0.0141	0.0029	-0.0141
4	0	2	2	0.0020	-0.0018	0.0019	-0.0018
5	1	0	2	-0.0079	0	-0.0079	0
4	0	-2	2	0.0020	0.0018	0.0020	0.0019

The values of the extracted coefficients, listed in Table 4.2 and 4.1, extracted using the invented ANN based coefficient extractor are close enough to those extracted with the conventional CM formulation. It can be stated that the invented ANN based CM coefficients extractor can extract sets of coefficients that can achieve the same functionality as the CM formulation under the ideal simulation environment.

The extracted coefficients from the ANN based coefficient extractor can be utilised to calculate the predicted output power and efficiency. With the modelled $B_{p,h}$ responses, the device output power and efficiency can be calculated with the following formulations:

$$P_{out}(dBm) = 30 + 10\log_{10}\left(\frac{1}{2}\left(|B_{2,1}|^2 - |A_{2,1}|^2\right)\right) \tag{4.7}$$

$$Efficiency = \frac{P_{out}}{|V_{ds} \times B_{2,0}|} \times 100\% \tag{4.8}$$

The performance of the extracted coefficients, with the device output power and efficiency contours, are shown in Fig. 4.5, and compared to the simulation results. According to the comparison, - 66 dB and - 51 dBm levels of Normalised Mean Square Error (NMSE) are achieved for the Wolfspeed device output power and efficiency contours respectively. This level of accuracy is proven sufficient for RF modelling techniques[6].

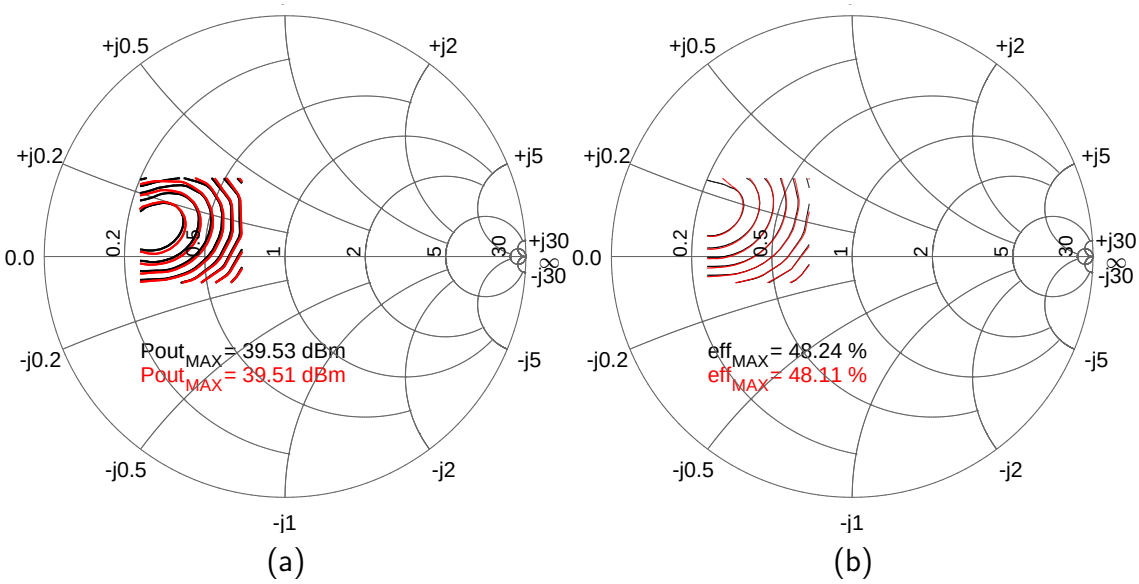

Figure 4.5: Simulated dataset (black) and ANN based coefficient extractor extracted coefficient performance (red) shown with 0.15 dBm output power steps (a) and 2% efficiency steps (b) contours plotted on the Smith Chart.

Then, a load-pull measurement is set up for the Wolfspeed 10 W device, to verify the invented coefficient extractor in practical situations. The measurement is done at 3.5 GHz, biased at $V_{DS} = 28$ V, $I_{Dq} = 59$ mA. The measurement is done with the Agilent N5242A PNAx with external sources, set up as in Fig. 4.6 [7]. The data in Fig. 4.7 is collected with a constant input drive corresponding to 1 dB compression

at the optimum load.

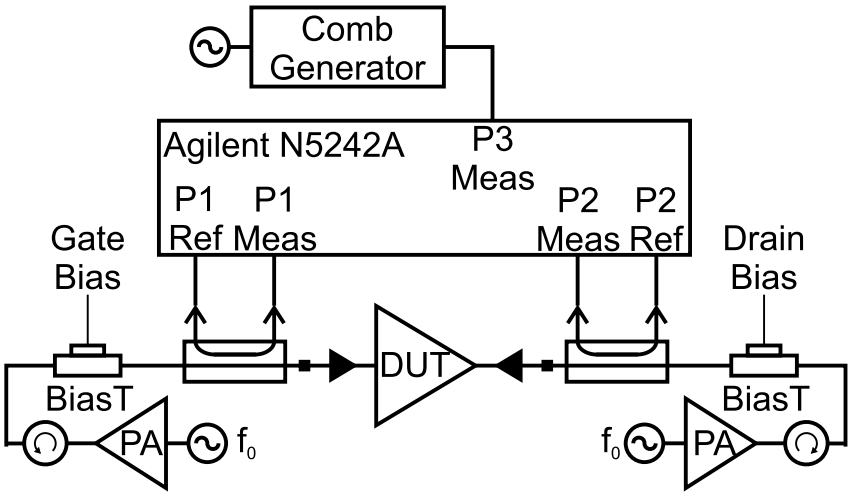

Figure 4.6: Measurement setup for the Wolfspeed device [7].

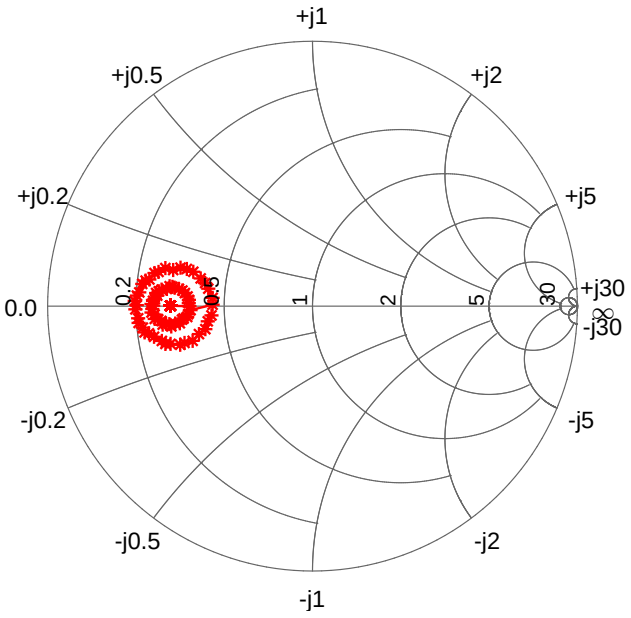

Figure 4.7: Measured load point location of the Wolfspeed device on the Smith Chart.

Here with the practical measurement setup, the tailored dataset for the CM model order determining spectrum analysis is not available. With the conventional CM formulation (2.15), a 5^{th} model order, which refers to the 10 coefficients listed in Table 4.3, are extracted to ensure an accurate model [2]. According to the verification done with the simulated load-pull measurement dataset previously, the listed coefficient values should also be the expected results from the ANN based coefficient extractor.

Table 4.3: The Extracted Cardiff Model Coefficients For Measured $B_{2,1}$ of the Wolfspeed Device Using Conventional CM Formulation

				$M_{2,1,m,n}$	
index	r	n	m	*Real*	*Imag.*
1	0	-2	2	0.0086	-0.0036
2	0	-1	1	0.1483	0.1056
3	0	0	0	3.8870	1.4159
4	0	1	1	-0.1093	0.0448
5	0	2	2	0.1528	-0.0006
6	0	3	3	0.0163	-0.0026
7	1	-1	3	0.0015	-0.0007
8	1	0	2	0.1300	0.1225
9	1	1	3	0.0561	0.0354
10	1	2	4	0.0070	0.0023

An FCC feedforward ANN structure that has been structured (as in Fig. 4.8) with two hidden layers, containing 3 and 2 neurons in the first and second hidden layer respectively, is selected to the measured data from the Wolfspeed device to extract 10 coefficients.

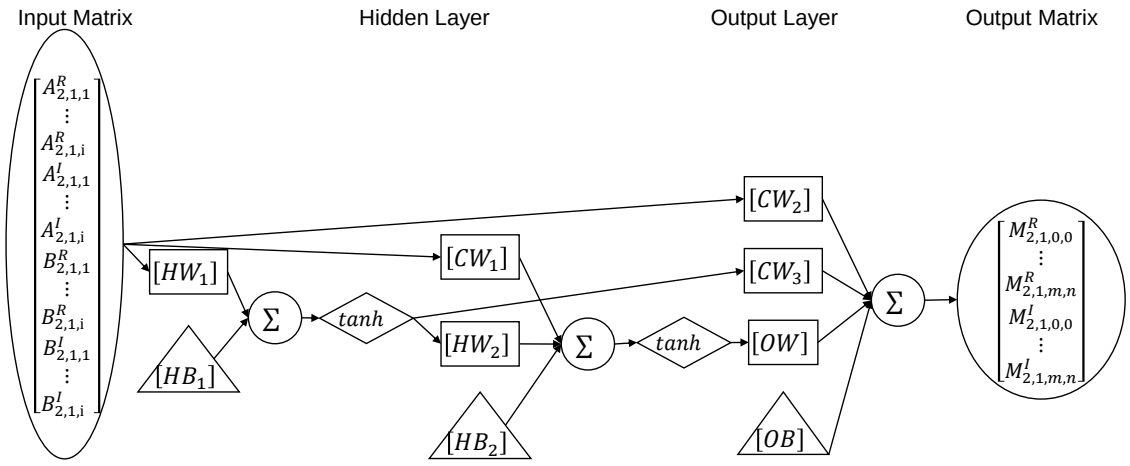

Figure 4.8: Two hidden layer FCC feedforward ANN based CM coefficient extractor structure.

The extracted coefficients from the ANN based CM coefficient extractor are listed in Table 4.4. The coefficient values are close enough to the extracted results given by the conventional CM formulation in Table 4.3. With the listed coefficients, the predicted $B_{2,1}$ can be calculated and so the device output power can be performed with contours on the Smith Chart as shown in Fig. 4.9.

Table 4.4: The Extracted Cardiff Model Coefficients For Measured $B_{2,1}$ of the Wolfspeed Device Using the invented ANN based Coefficient Extractor

				$M_{2,1,m,n}$	
index	r	n	m	*Real*	*Imag.*
1	0	-2	2	0.0086	-0.0036
2	0	-1	1	0.1483	0.1056
3	0	0	0	3.8870	1.4159
4	0	1	1	-0.1093	0.0447
5	0	2	2	0.1528	-0.0006
6	0	3	3	0.0163	-0.0026
7	1	-1	3	0.0015	-0.0007
8	1	0	2	0.1300	0.1225
9	1	1	3	0.0561	0.0354
10	1	2	4	0.0071	0.0023

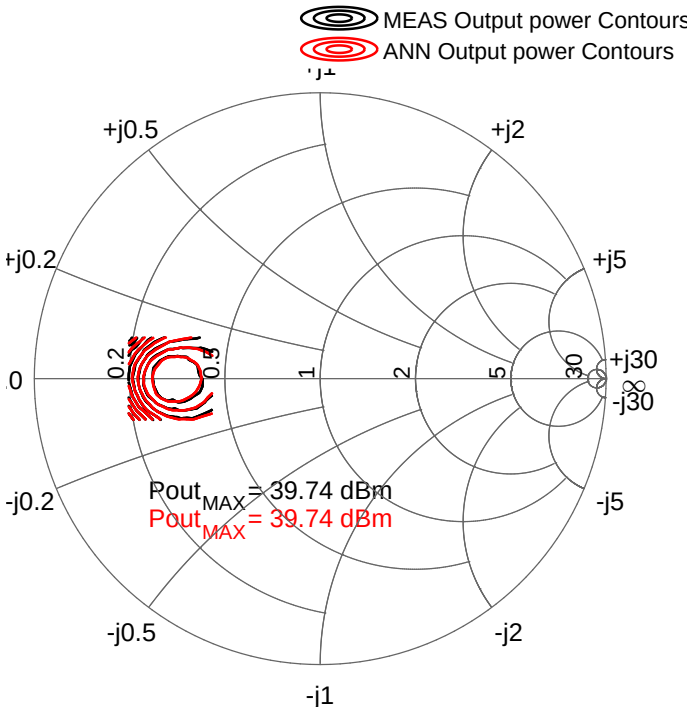

Figure 4.9: Output power contours calculated with the extracted coefficients from the ANN based coefficient extractor (red) vs. Measurement (black) of the Wolfspeed device with NMSE levels of - 72 dB.

For DC response $B_{2,0}$, which is the drain DC current, the extracted coefficients using the conventional CM formulation are listed in Table 4.5.

The same ANN structure as in Fig. 4.4 is utilised for extracting the DC correlated coefficients. The extracted coefficients from the ANN based coefficient extractor are listed in Table 4.6.

Table 4.5: The Extracted Cardiff Model Coefficients For Measured $B_{2,0}$ of the Wolfspeed Device Using Conventional CM Formulation

				$M_{2,0,m,n}$	
index	*r*	*n*	*m*	*Real*	*Imag.*
1	0	-2	2	0.0044	0.0074
2	0	-1	1	0.0669	-0.0138
3	0	0	0	0.7842	-0.0095
4	0	1	1	0.0521	0.0088
5	0	2	2	-0.0034	-0.0040
6	0	3	3	-0.0007	0.0008
7	1	-1	3	0.0023	0.0016
8	1	0	2	0.0154	-0.0005
9	1	1	3	-0.0009	-0.0003
10	1	2	4	-0.0003	0.0003

Table 4.6: The Extracted Cardiff Model Coefficients For Measured $B_{2,0}$ of the Wolfspeed Device Using the invented ANN based Coefficient Extractor

				$M_{2,0,m,n}$	
index	*r*	*n*	*m*	*Real*	*Imag.*
1	0	-2	2	0.0044	0.0074
2	0	-1	1	0.0670	-0.0138
3	0	0	0	0.7843	-0.0095
4	0	1	1	0.0522	0.0088
5	0	2	2	-0.0034	-0.0040
6	0	3	3	-0.0007	0.0008
7	1	-1	3	0.0023	0.0016
8	1	0	2	0.0154	-0.0005
9	1	1	3	-0.0009	-0.0002
10	1	2	4	-0.0003	0.0003

Compared with the results of the conventional CM coefficients in Table 4.5, the values of the two sets of extracted coefficients are close enough, as it was performed with the fundamental travelling wave response $B_{2,1}$. With the extracted coefficients correlated to the DC and fundamental response, the device efficiency contours on the Smith Chart can be calculated and performed as shown in Fig.4.10.

It can be seen from the results that the ANN extractor can work out sets of coefficients similar to the standard least square algorithm with the conventional CM formulation, and provide accurate results with the device output power and efficiency contours compared to load-pull measurement results under both simulation

and practical scenarios. Hence, the invented ANN based CM coefficient extractor is verified as an accurate coefficient extraction method.

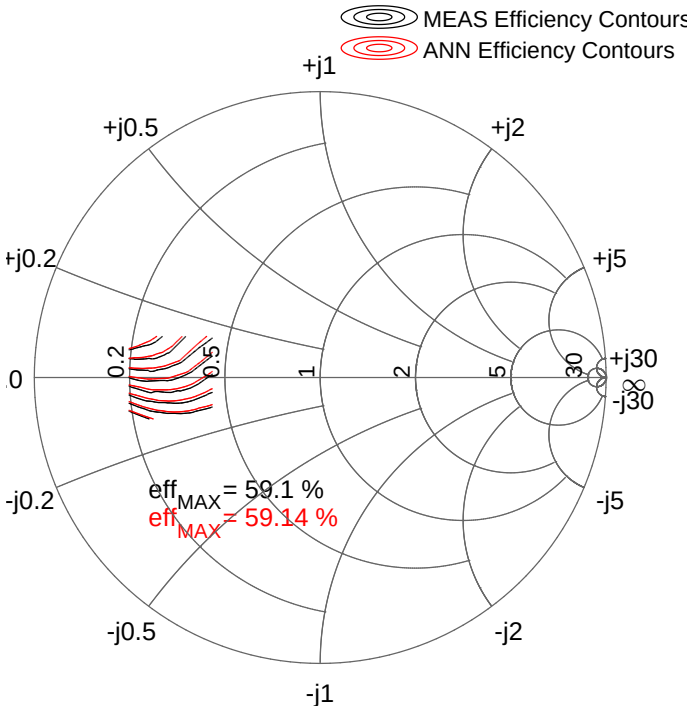

Figure 4.10: Efficiency contours calculated with the extracted coefficients from the ANN based coefficient extractor (red) vs. Measurement (black) of the Wolfspeed device with NMSE level of - 53 dB.

4.3 Models Combination for Extrapolation Ability

The invented ANN based coefficient extractor is proved accurate for extracting the CM coefficients in the previous section. The values of the extracted coefficients can be identical to those extracted with the conventional CM formulation. However, based on the analysis presented in Chapter 3, the coefficients extracted using the conventional CM formulation with user-defined model order can potentially provide erroneous prediction results when extrapolating. When the tailored dataset is unavailable in practical load-pull measurement scenarios, the required CM mixing order will still be the user-defined model order. In this case, the invented ANN

based CM coefficient extractor is not robust enough to guarantee the expected reasonable extrapolation prediction, since the extracted coefficients are still identical to the conventional CM.

It is also proven in Chapter 3 that a trained conventional A-B wave-based ANN behavioural model, with properly defined number of hidden neurons and initial values of weights and biases, can provide reasonable extrapolation predictions as an accurate behavioural model. Therefore, the trained A-B wave-based ANN model can be considered and utilised for obtaining reasonable extrapolation predictions outside the load-pull measurement covered region.

When combining the conventional A-B wave-based ANN behavioural model with the invented coefficient extractor, the A-B wave-based ANN model extrapolated data can be easily applied to the coefficient extractor by varying the targets given to the modified LM training algorithm. Different CM coefficient sets will then be extracted using both the load-pull measured A-B wave datasets and the A-B wave-based ANN model predicted B wave datasets, instead of the load-pull measured data only. Hence, reasonable extrapolation ability can be expected from the extracted coefficient sets, even for the CM with high user-defined model order.

For applying an artificial set of extrapolated data predicted by the conventional A-B wave-based ANN behavioural model to the coefficient extractor, here, step 7 in Algorithm 2 is changed from: $\boldsymbol{B}_{p,h\_\mathbf{Error}} = \boldsymbol{B}_{p,h\_\mathbf{Modelled}} - \boldsymbol{B}_{p,h\_Measured}$ to the highlighted step as shown in Algorithm 3 below.

Algorithm 3 Modified Steps of Levenberg-Marquart Algorithm for CM Coefficients Extractor

1: INPUT: $\boldsymbol{A}_{2,1\_Measured}, \boldsymbol{B}_{p,h\_Measured}$
2: $[\boldsymbol{A}] = (\angle \boldsymbol{A}_{1,1})^{h} \left|\boldsymbol{A}_{2,1\_Calculated}\right|^{m} \left(\frac{\angle \boldsymbol{A}_{2,1}}{\angle \boldsymbol{A}_{1,1}}\right)^{n}$
3: *Initialise:* $[\boldsymbol{W}_i], [\boldsymbol{B}_i] \leftarrow rand[-1, 1]$
4: **for** *epoch* $= 1$
5: $\boldsymbol{M}_{p,h,m,n} = [\boldsymbol{W}_i][\boldsymbol{A}_{\mathbf{2,1}\_Measured}, \boldsymbol{B}_{p,h\_Measured}] + [\boldsymbol{B}_i]$
6: $\boldsymbol{B}_{p,h\_\mathbf{Modelled}} = \sum_{\mathbf{r}} \sum_{\mathbf{n}} M_{p,h,m,n} \times [\boldsymbol{A}]$
7: $\boldsymbol{B}_{p,h\_\mathbf{Error}} = \boldsymbol{B}_{p,h\_\mathbf{Modelled}} - \boldsymbol{B}_{p,h\_ANNpredicted}$
8: $\boldsymbol{M}_{p,h,m,n\_Error} = \left([\boldsymbol{A}]^{H}[\boldsymbol{A}]\right)^{-1} \left([\boldsymbol{A}]^{H}[\boldsymbol{B}_{p,h\_\mathbf{Error}}]\right)$
9: *Compute* ***Jacobian***
10: *Update:* $[\boldsymbol{W}_i]$ *and* $[\boldsymbol{B}_i]$ *till required error level met*
11: **end for**
12: OUTPUT: $\boldsymbol{M}_{p,h,m,n}$

Two sets of measured data, from the Wolfspeed 10 W packaged device and a WIN NP12 4x25 um GaN on-wafer device measurements, acquired under different operating scenarios, located in the different regions on the Smith Chart, are utilised for troubleshooting and proving the robustness of the proposed method.

The coefficients extracted with the 5^{th} model order using the invented CM coefficient extractor for the Wolfspeed device load-pull measurement data, presented in the coefficient extractor accuracy verification section in Fig 4.7, Table 4.4, can be applied for verifying the model extrapolation ability.

A set of manually generated stimulus $A_{2,1}$ circles are populated for model coefficients' extrapolation ability testing under practical scenarios, where a load-pull measurement with large coverage on the Smith Chart is time-consuming and expensive to obtain. The formulation for generating the stimulus $A_{2,1}$ circles is shown as follows:

$$A^{i}_{2,1} = A^{0}_{2,1} + A^{\Delta}_{2,1}(\cos(2\pi\frac{i}{N}) + j\sin(2\pi\frac{i}{N})) \tag{4.9a}$$

$$A^{\Delta}_{2,1} = ac + bi \tag{4.9b}$$

here, $A^{0}_{2,1}$ is setting up the centre. $A^{\Delta}_{2,1}$ is defining the data extended coverage range, where 'a' and 'b' represent a user-defined real and imaginary parts with a sweeping

index 'c' determined to the magnitude term. The index 'i' can be varied from 0 to $N-1$, 'N' is the total number of points.

To get the maximum coverage within the whole Smith Chart based on the measurement data coverage as shown in Fig. 4.7, the sweeping index c has been determined from 1 to 6 in this case. The calculated stimulus $A_{2,1}$ circles are plotted as in Fig. 4.11, together with the $A_{2,1}$ values acquired from the load-pull measurement.

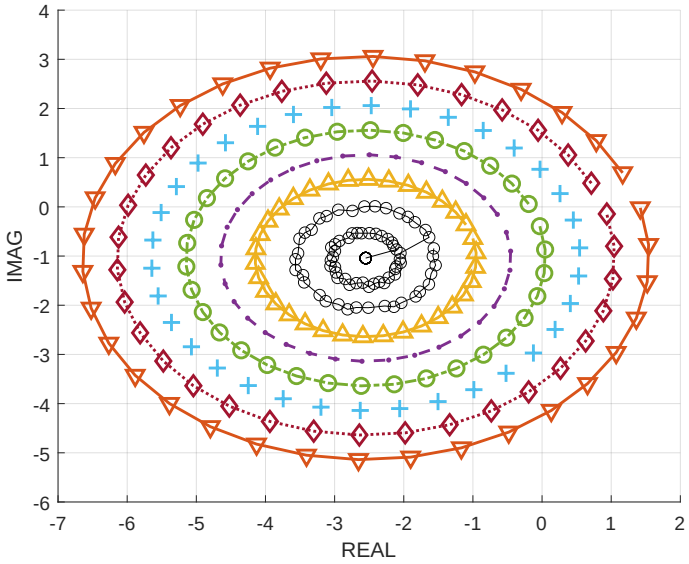

Figure 4.11: Calculated $A_{2,1}$ surrounding the measured dataset of the Wolfspeed device for the ANN the trained A-B wave-based ANN model to generate the artificial set of extrapolated data.

With the colour-coded calculated $A_{2,1}$ in Fig.4.11, the extrapolation results provided by the coefficients extracted using the measurement data and the invented coefficient extractor, listed in Table 4.4, are shown in Fig. 4.12 (a,c). Then, the load-pull measurement data of the Wolfspeed device, in Fig 4.7, is normalised with a scale to $[-1, 1]$ for conventional A-B wave-based ANN model training. The same feedforward structure shown in Fig. 3.13 is used here for the A-B wave-based ANN model, with 7 hidden neurons in the hidden layer. After the ANN model training, applied the measurement data scale factor to the calculated stimulus $A_{2,1}$ in Fig. 4.11, the normalised $A_{2,1}$ can then be fed into the trained A-B wave ANN model to obtain an artificial set of extrapolated data. The extrapolated data performance is shown

in Fig. 4.12 (b,d).

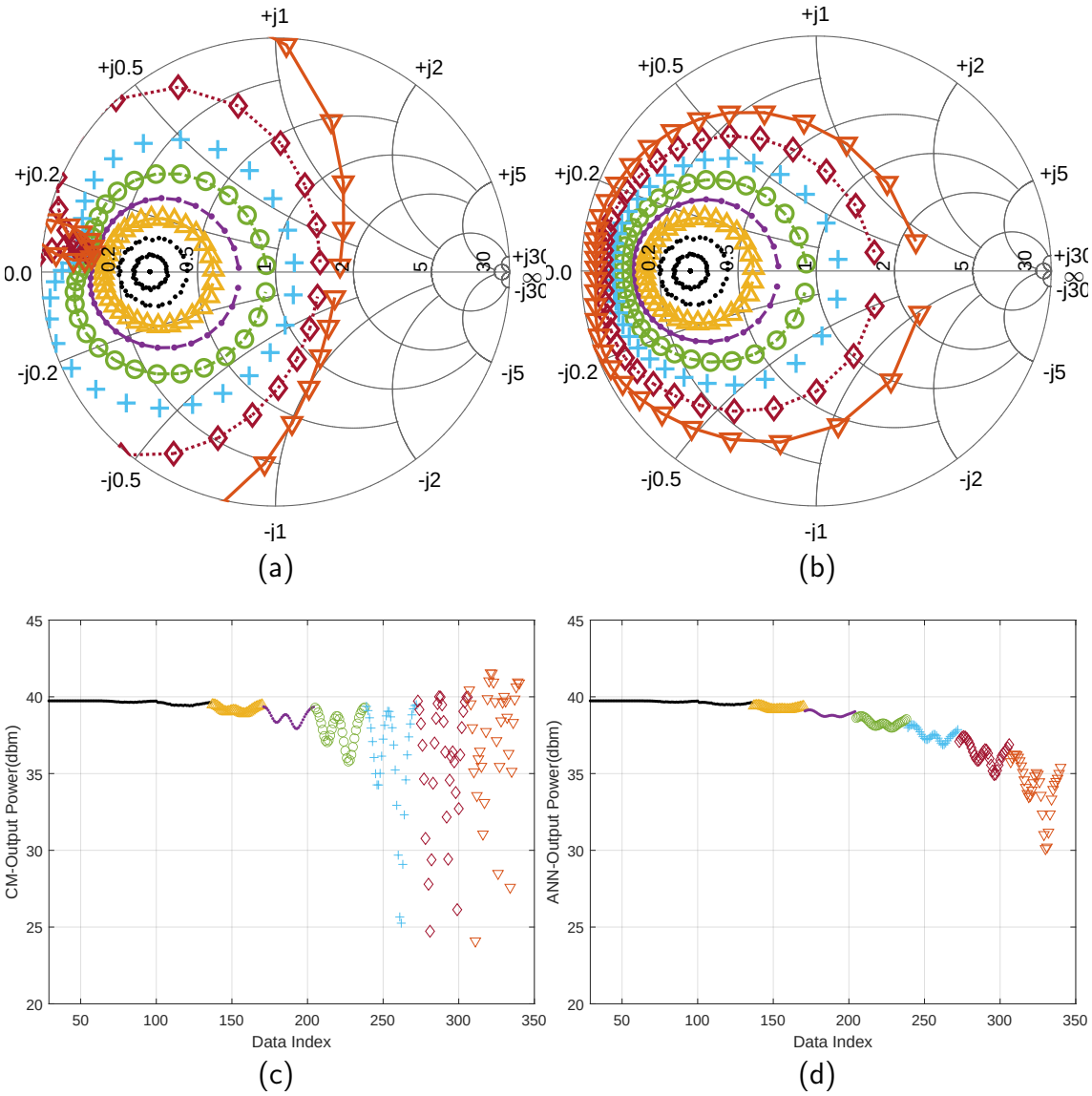

Figure 4.12: The performance shown with $\Gamma_{2,1}$ points plotted on the Smith Chart and output power of the coefficients extracted invented ANN based CM coefficient extractor (a,c) and the conventional A-B wave based ANN model (b,d) for the Wolfspeed device.

Different from the analysis done with simulation datasets in Chapter 3, under practical scenarios, measurement is not done on the extrapolation region, so the data reference for accurate extrapolation results comparison is not available. The extrapolated device response/model prediction result is evaluated using robust modelling theory. Ideally, the extrapolated $B_{2,1}$ wave as a function of the $A_{2,1}$ should show expanding circles/ellipses $\Gamma_{2,1}$ points when moving away from the optimum on the

Smith Chart. However, Fig. 4.12 (a) shows clearly that the extrapolated $\Gamma_{2,1}$ points sit on unrealistic trajectories with cusps and knots, when the coefficients are extracted from the measurement data directly using the invented coefficient extractor. This is best visualised in Fig. 4.12 (c) where the extrapolated output power is not following a decreasing trend away from the measured optimum. The erroneous extrapolation behaviours are all absent in the predicted $\Gamma_{2,1}$ points and the output power provided by the trained A-B wave ANN model, as shown in Fig. 4.12 (b,d). Hence, the trained A-B wave ANN model provides more reasonable extrapolation results, later defined as an artificial set of extrapolated data, with the calculated stimulus $A_{2,1}$ circles.

The artificial set of extrapolated data (shown in Fig. 4.12 (b)) is then fed into the invented coefficient extractor following the proposed method, as the modified targets to the LM training algorithm demonstrated in Algorithm 3. The coefficient extractor here has been structured (as in Fig. 4.8) containing 3 and 4 neurons in the first and second hidden layer respectively. A different set of coefficients is extracted with the artificial set of extrapolated data and the measurement dataset, and listed in Table 4.7, compared to the coefficient values extracted using the coefficient extractor with the measurement data only.

Table 4.7: The Extracted Coefficients Comparison For Measured $B_{2,1}$ of the Wolfspeed Device Using Different Methods

				$M_{2,1,m,n}$			
				Measured Data Only		Combined Method	
index	r	n	m	*Real*	*Imag.*	*Real*	*Imag.*
1	0	-2	2	0.0086	-0.0036	-0.0030	-0.0035
2	0	-1	1	0.1483	0.1056	0.0089	-0.0002
3	0	0	0	3.8870	1.4159	3.4993	1.3105
4	0	1	1	-0.1093	0.0447	-0.5295	-0.0831
5	0	2	2	0.1528	-0.0006	-0.0042	-0.0163
6	0	3	3	0.0163	-0.0026	-0.0014	0.0004
7	1	-1	3	0.0015	-0.0007	-0.0014	-0.0006
8	1	0	2	0.1300	0.1225	-0.0036	-0.0072
9	1	1	3	0.0561	0.0354	0.0011	-0.0011
10	1	2	4	0.0071	0.0023	0	0.0001

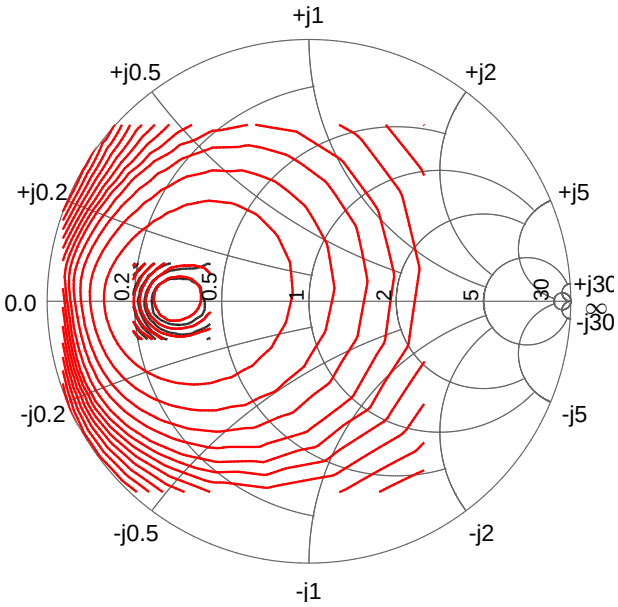

Figure 4.13: 0.4 dBm Output power contours prediction with the extracted coefficients using the proposed combined method (red) vs. Measurement (black) of the Wolfspeed device where the level NMSE of the interpolation region remains - 61 dB.

With the listed coefficients, the predicted $B_{2,1}$ can be calculated and so the device output power can be calculated and performed with contours on the Smith Chart as shown in Fig. 4.13, compared to the measured output power contours of the Wolfspeed device. The coefficients predicting accuracy in the measurement region remain. It can be seen that the output power contours demonstrated with no erroneous features shown in Fig. 4.13 as moving from the optimum to the edge of the Smith Chart.

The procedure is repeated to obtain the efficiency contours for further proving the extrapolation ability of the proposed combined method. A linear structure is implemented, as shown in Fig. 4.14, for a conventional A-B wave ANN behavioural model training.

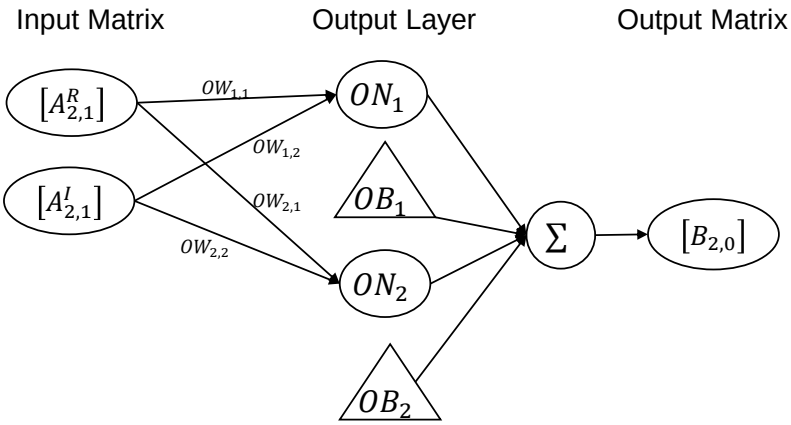

Figure 4.14: Linear A-B wave-based ANN model structure.

By feeding the colour-coded calculated $A_{2,1}$ in Fig.4.11 into the trained A-B wave ANN model, the predicted DC device response $B_{2,0}$, which is also the $I_{2,0}$ (drain DC current) can then be applied to the invented coefficient extractor using the modified LM Algorithm 3. The pure linear structure as Fig. 4.4, similar to Fig. 4.14 but changing the input matrix into related A travelling waves only and the output matrix into the DC device response $B_{2,0}$, is utilised here as well for the coefficient extractor. A different set of coefficients is extracted for $B_{2,0}$, listed in Table 4.8, compared to the coefficients extracted with the coefficient extractor using measurement data only.

Table 4.8: The Extracted Coefficients Comparison For Measured $B_{2,0}$ of the Wolfspeed Device Using Different Methods

				$M_{2,0,m,n}$			
				Measured Data Only		Combined Method	
index	*r*	*n*	*m*	*Real*	*Imag.*	*Real*	*Imag.*
1	0	-2	2	0.0044	0.0074	0	0
2	0	-1	1	0.0670	-0.0138	0.0314	-0.0349
3	0	0	0	0.7843	-0.0095	0.7257	0
4	0	1	1	0.0522	0.0088	0.0314	0.0350
5	0	2	2	-0.0034	-0.0040	0	0
6	0	3	3	-0.0007	0.0008	0	0
7	1	-1	3	0.0023	0.0016	0	0
8	1	0	2	0.0154	-0.0005	0	0
9	1	1	3	-0.0009	-0.0002	0	0.0001
10	1	2	4	-0.0003	0.0003	0	0

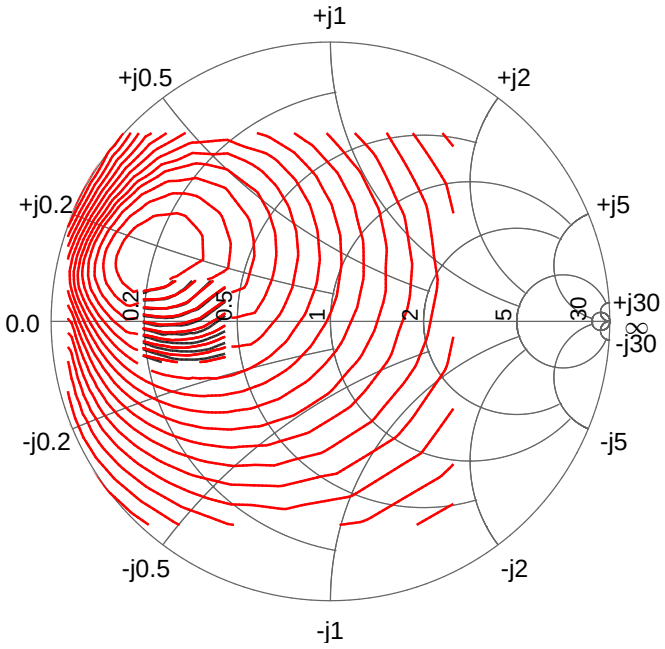

Figure 4.15: Predicted efficiency contours (5.6%/step) calculated with the extracted coefficients using the proposed combined method (red) vs. Measurement (black) of the Wolfspeed device, where the level NMSE of the interpolation region remains - 44 dB.

Results as shown in Fig. 4.15 demonstrate accurate predictions within the measurement region since the predicted efficiency contours from the coefficients extracted with the combined method are aligned with the measured efficiency contours. Also, no erroneous features appear in the extrapolated efficiency contours. Hence, coefficients extracted with high user-defined model order by combining the conventional A-B wave-based ANN behavioural and the invented ANN technique-based CM coefficient extractor, is proven able to provide accurate interpolation predictions and also reasonable extrapolation predictions.

A dataset acquired from load-pull measurement done with a WIN NP12 4x25 um on-wafer device at 20 GHz, biased at $V_{\mathrm{DS}} = 15$ V, $I_{\mathrm{Dq}} = 10$ mA with a constant input drive corresponding to 3 dB compression at the optimum load, is also utilised here. This is for verifying the combined method robustness on different device manufacture techniques, under different operation conditions, and responses located in different regions on the Smith Chart, compared to the Wolfspeed device measurement. The

measured WIN device measurement follows the same setup as Fig. 4.6 but with the R&S ZVA 67 [8], the acquired data location on the Smith Chart is shown in Fig. 4.16.

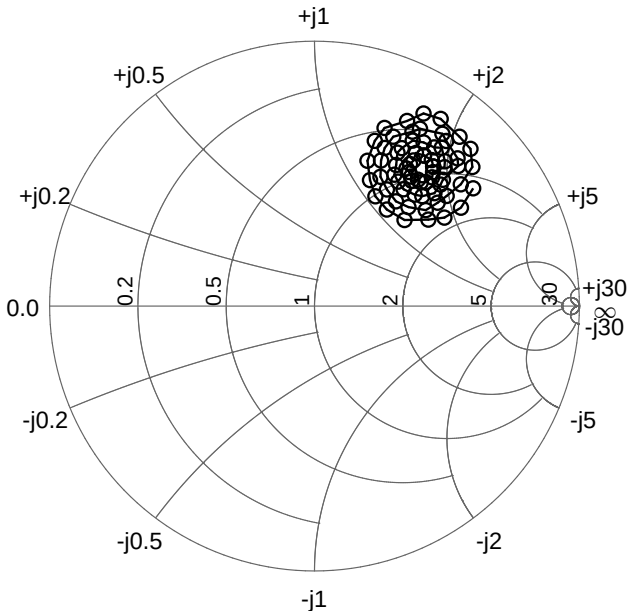

Figure 4.16: Measured WIN data.

The process is identical to the analysis for the Wolfspeed device measurement data, and has been repeated for the WIN device load-pull measurement dataset. Firstly, the measurement data shown in Fig. 4.16 is utilised for a 5^{th} order model with the invented ANN based CM coefficient extractor. The extracted coefficients are listed in Table 4.9.

Table 4.9: The Extracted Coefficients For Measured $B_{2,0}$ of the WIN Device Using the Invented ANN Based Coefficient Extractor

				$M_{2,1,m,n}$	
index	r	n	m	*Real*	*Imag.*
1	0	-2	2	0.0753	0.0613
2	0	-1	1	0.0156	0.1331
3	0	0	0	0.0383	0.4115
4	0	1	1	0.3171	-0.7009
5	0	2	2	-0.1507	-0.1988
6	0	3	3	0.0226	-0.1242
7	1	-1	3	-0.0225	0.1520
8	1	0	2	-0.2892	0.2043
9	1	1	3	-0.2737	-0.0078
10	1	2	4	-0.0618	-0.1077

Secondly, a conventional A-B wave-based ANN model is trained with the dataset, for an artificial set of extrapolated data. In this case with the measurement date of the WIN device, one hidden layer structure (as in Fig 3.13) containing 4 hidden neurons is selected for the A-B wave-based ANN model.

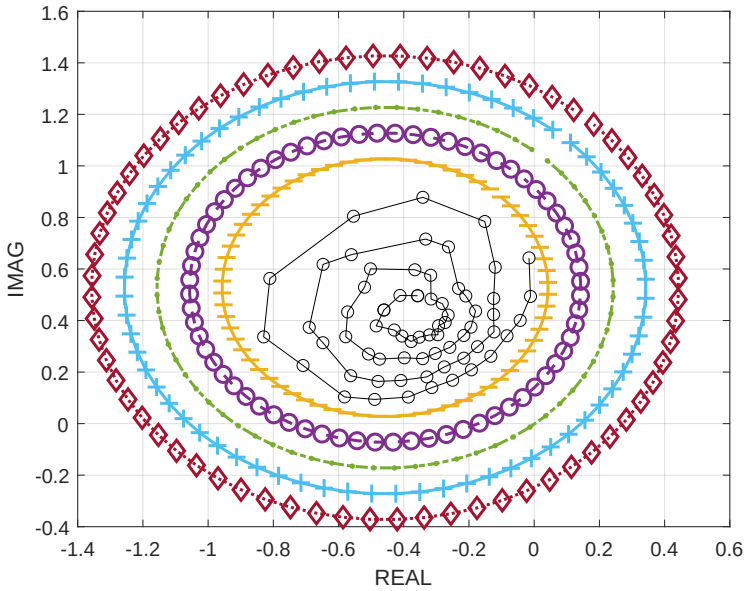

Figure 4.17: Calculated $A_{2,1}$ surrounding the measured dataset of the WIN device for the ANN the trained A-B wave-based ANN model to generate the artificial set of extrapolated data.

To propagate a calculated $A_{2,1}$ dataset that gets the maximum coverage within the whole Smith Chart that can be utilised with the trained A-B wave-based ANN model, values of the sweeping index c of $A^{\Delta}_{2,1}$ in (4.9a) have been determined as from 1 to 5 for the WIN device. The extrapolated load circles are markers and colour-coded consistently with c sweeps indexed as shown in Fig. 4.17.

The calculated $A_{2,1}$ data is then applied with both coefficient sets extracted with the invented ANN based coefficients extractor and the trained A-B wave ANN model for extrapolation performance comparison. The extrapolated results are shown in Fig. 4.18.

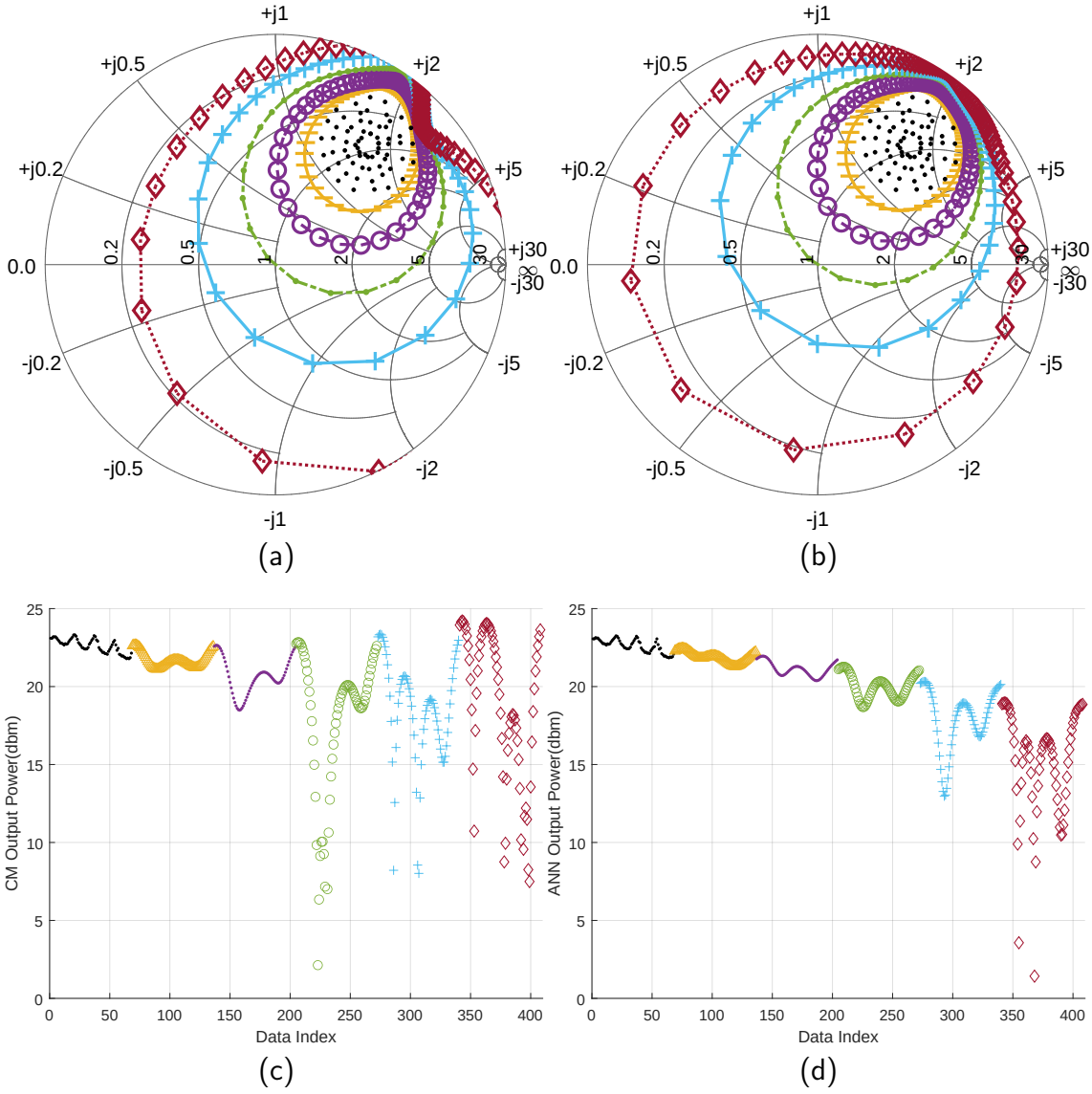

Figure 4.18: The performance shown with $\Gamma_{2,1}$ points plotted on the Smith Chart and output power of the coefficients extracted invented ANN based CM coefficient extractor (a,c) and the conventional A-B wave based ANN model (b,d) for the WIN device.

The results demonstrate the same scenario as the results presented with the Wolfspeed device measurement data. The $\Gamma_{2,1}$ points extrapolated by the invented coefficient extractor shown in Fig. 4.18 (a) are located on unrealistic trajectories, and bring with erroneous extrapolated output power values in Fig. 4.18 (c), as moving from the optimum to the edge of the Smith Chart. The extrapolation results provided by the trained A-B wave ANN model in Fig. 4.18 (b,d) follow the theoretical analysis in an ideal modelling state, the predicted $\Gamma_{2,1}$ points expand in circles and

the output power values follow a decreasing trend with no erroneous features as moving from the optimum to the edge of the Smith Chart.

Then, the artificial set of extrapolated data, which is the colour-coded data with different markers shown in Fig. 4.18 (b), predicted by the trained A-B wave ANN model extrapolation, is utilised as the modified targets to the LM training algorithm demonstrated in Algorithm 3. The coefficient extractor has been structured (as in Fig. 4.8) with containing 5 hidden neurons in both hidden layers for the WIN device, both hidden layers.

A different set of coefficients is extracted with the artificial set of extrapolated data and the measurement dataset, listed in Table 4.10. The predicted $B_{2,1}$ can be calculated with the listed coefficients, and so the device output power can be performed with contours on the Smith Chart as shown in Fig. 4.19, compared to the measured output power contours of the WIN device.

Table 4.10: The Extracted Cardiff Model Coefficients For Measured $B_{2,1}$ of the Wolfspeed Device Using the Combined Method

				$M_{2,1,m,n}$	
index	r	n	m	*Real*	*Imag.*
1	0	-2	2	0.0289	-0.0150
2	0	-1	1	0.0565	-0.0002
3	0	0	0	0.0882	0.3900
4	0	1	1	0.4974	-0.6540
5	0	2	2	-0.0099	-0.0337
6	0	3	3	-0.0033	-0.0118
7	1	-1	3	0.0095	0.0246
8	1	0	2	-0.0040	0.0226
9	1	1	3	-0.0286	0.0099
10	1	2	4	-0.0046	0.0003

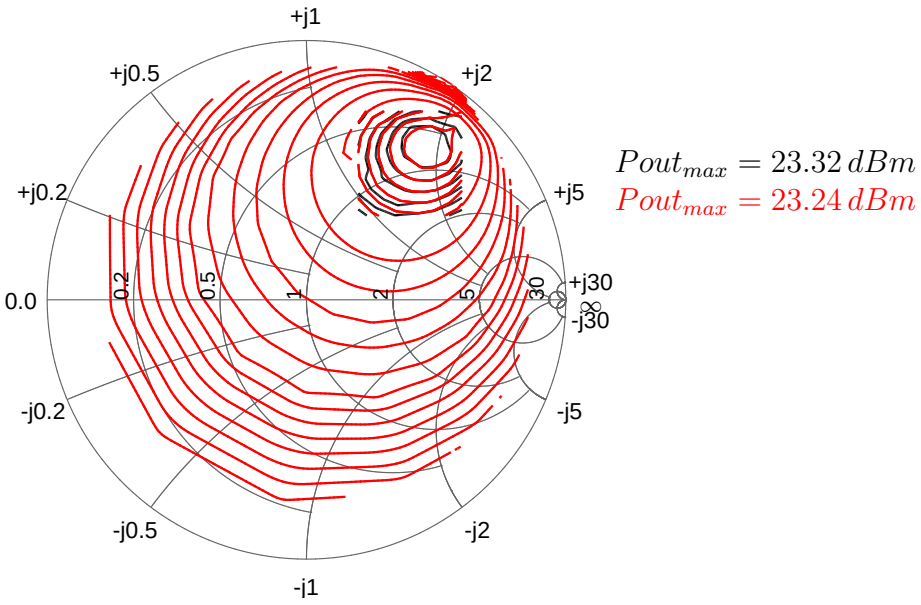

Figure 4.19: The combined method extracted coefficient performance of the WIN device, shown with predicted output power contours (1.3 dBm/step) on the Smith Chart, where the level of NMSE in the interpolation region remains - 51 dB.

A Linear A-B wave-based ANN model is trained for the DC response. By feeding the calculated $A_{2,1}$ into the trained model, the artificial set of extrapolated data is then utilised in the training target modified coefficient extractor, for coefficient extraction. The extracted $B_{2,0}$ correlated coefficients are listed in Table 4.11. The extracted coefficient predicted efficiency contours are shown in Fig. 4.20, compared to the measured data of the WIN device.

Table 4.11: The Extracted CM Coefficients For Measured $B_{2,0}$ of the WIN Device Using the Combined Method

				$M_{2,0,m,n}$	
index	*r*	*n*	*m*	*Real*	*Imag.*
1	0	-2	2	0	0
2	0	-1	1	0.0038	-0.0069
3	0	0	0	0.0409	0
4	0	1	1	0.0038	0.0068
5	0	2	2	0	0
6	0	3	3	0	0
7	1	-1	3	0	0
8	1	0	2	0	0
9	1	1	3	0	0
10	1	2	4	0	0

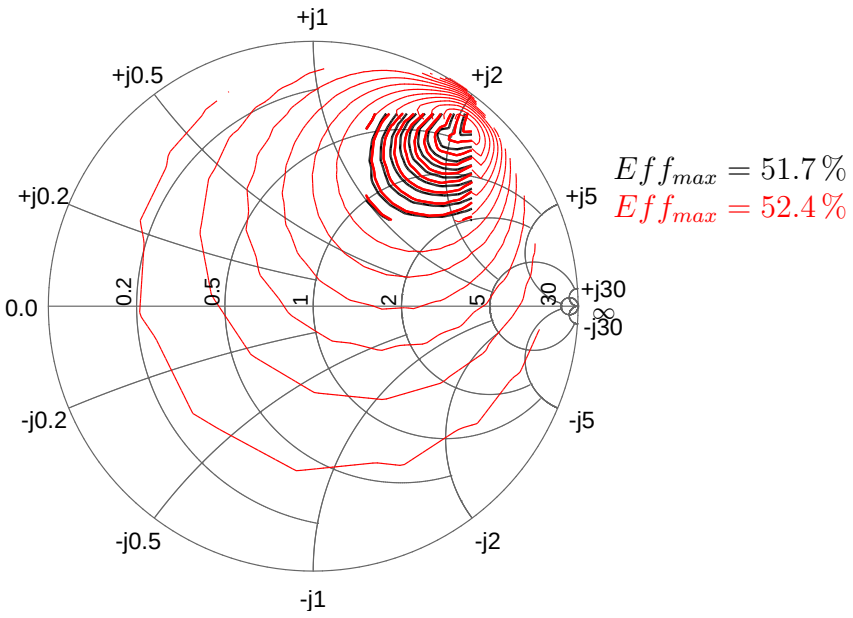

Figure 4.20: The combined method extracted coefficient performance of the WIN device, shown with predicted efficiency contours (6.4%/step) plotted on the Smith Chart, where the level of NMSE in the interpolation region remains - 39.8 dB.

4.4 Discussion

In practical scenarios, when the tailored datasets for properly defined truncated CMs are not available, the high mixing order CM coefficient sets obtained with the combined method, can now provide not only interpolation predictions with a high level of accuracy but also ensure extrapolation without unrealistic power and efficiency predictions.

However, the introduced combined method utilises the ANN technique as the core, which then indicates that the model structure will have to be properly selected. Following the analysis in Chapter 3, different determined values for the number of hidden neurons and the initial values of the ANN can provide completely different model accuracy and extrapolation ability. When utilising the conventional A-B wave-based ANN behavioural model to generate an artificial set of extrapolated data for the invented ANN technique-based CM coefficient extractor as the training

target, the A-B wave-based ANN will need to be carefully determined.

Here in this Chapter, the ANN structure determining process relies on parameter sweeps, and values with the best performance are selected. When the system complexity increases, this way of determining the structure does not always guarantee success if the sweeping plan proves ineffective. Other procedures can be further explored for a guaranteed ANN model structure determining method.

4.5 Conclusion

Overall in this chapter, the proposed methods provide verified opportunities for the high order CM coefficients with reasonable extrapolation ability to be extracted using the modified ANN technique.

An invented ANN technique-based CM coefficient extractor is introduced. The Wolfspeed 10 W packaged Gallium Nitride (GaN) device load-pull measurement datasets, under both CAD simulation environment and practical environment, are used for accuracy verification. With the modified LM training algorithm, the invented coefficient extractor is proven able to extract CM coefficients with the same level of accuracy as those extracted using the conventional CM formulation.

The combined procedure for extracting high user-defined order CM coefficients exploiting the reasonable extrapolation capabilities is also presented. The procedure combined the conventional A-B wave-based ANN behavioural model and the invented ANN technique-based CM coefficient extractor. The training target of the modified LM training algorithm can be varied. The verification results show that the combined method can help to avoid the non-physical CM model behaviour when used in CAD simulations to optimize the matching networks when CM model extraction is constrained by load-pull measurement limitations. The robustness of the proposed combined method is shown by utilising two different GaN devices,

Wolfspeed 10 W packaged GaN device and a WIN Semiconductor GaN on-wafer device, with practical measured load-pull datasets under different frequency and power levels.

References

[1] W. Yuan, M. Tian, J. Bell, "Implementation Efficiency Comparison Between ANN and the Cardiff Model in ADS," in *2023 International Workshop on Integrated Nonlinear Microwave and Millimetre-Wave Circuits (INMMIC)*, Aveiro, Portugal, Nov. 2023, pp. 1–4. DOI: 10.1109/INMMIC57329.2023.10321776.

[2] P.J. Tasker, J. Benedikt, "Waveform Inspired Models and the Harmonic Balance Emulator," *IEEE Microwave Magazine*, vol. 12, no. 2, pp. 38–54, Apr. 2011. DOI: 10.1109/MMM.2010.940101.

[3] M.T. Hagan, M.B. Menhaj, "Training feedforward networks with the Marquardt algorithm," *IEEE Transactions on Neural Networks*, vol. 5, no. 6, pp. 989–993, Jun. 1994. DOI: 10.1109/72.329697.

[4] M. Tian, J. Bell, E. Azad, R. Quaglia, P. Tasker, "A Novel Cardiff Model Coefficients Extraction Process Based on Artificial Neural Network," in *2023 IEEE Topical Conference on RF/Microwave Power Amplifiers for Radio and Wireless Applications*, Las Vegas, NV, USA, Jan. 2023, pp. 1–3. DOI: 10.1109/PAWR56957.2023.10046221.

[5] P.J. Tasker, "Robust Extraction of Cardiff Model Parameters from Appropriately Tailored Measured Load-Pull Data," in *2020 IEEE BiCMOS and Compound Semiconductor Integrated Circuits and Technology Symposium (BCICTS)*, Monterey, CA, USA, Nov. 2020, pp. 1–5. DOI: 10.1109/BCICTS48439.2020.9392942.

[6] M.R. Moure, M. Casbon, M. Fernández-Barciela, P.J. Tasker, "Direct extraction of an admittance domain behavioral model from large-signal load-pull measurements," in *2017 IEEE MTT-S International Microwave Symposium (IMS)*, Honololu, HI, USA, Jun. 2017, pp. 1057–1060. DOI: 10.1109/MWSYM.2017.8058775.

[7] R. Quaglia, D.J. Shepphard, S. Cripps, "A Reappraisal of Optimum Output Matching Conditions in Microwave Power Transistors," *IEEE Transactions on Microwave Theory and Techniques*, vol. 65, no. 3, pp. 838–845, Mar. 2017. DOI: 10.1109/TMTT.2016.2627557.

[8] E.M. Azad, J.J. Bell, R. Quaglia, Rubio, J. M., P.J. Tasker, "Gate Bias Incorporation into Cardiff Behavioural Modelling Formulation," in *2020 IEEE/MTT-S International Microwave Symposium (IMS)*, Los Angeles, CA, USA, Aug. 2020, pp. 420–423. DOI: 10.1109/IMS30576.2020.9223817.

Chapter 5

A Discovery of the Artificial Neural Network (ANN) Structure Defining Method

It has been presented in Chapter 3 that the Artificial Neural Network (ANN) model fitting process generally requires an initial setup for the values of the hidden neuron numbers, weights and biases. The ANN structure is not fixed for systems with different nonlinearity [1]–[3]. Different ANN initialisation configurations used when training ANNs yield different results with different associated errors [4]–[7]. Overdetermining the values may lead to the phenomenon of overlearning [8], [9]. For an optimisation method for finding the optimal configuration of an ANN behavioural model, an ANN structure determining method is proposed in this chapter.

Considering that the Cardiff Model (CM) provides a mathematically formulated nonlinear model that is based on the physics of signal mixing theory [10]–[12], the proposed method utilises the CM with tailored datasets for determining the nonlinearity of systems, hence, the required polynomial order. The ANN structure (number of hidden neurons) and the internal parameter determination process (val-

ues of the weights and biases), are guaranteed by the CM coefficients and the method results in high model accuracy and reasonable extrapolation ability. In the practical scenario with load-pull measurement systems, an alternative measurement procedure is introduced to acquire the required tailored dataset.

5.1 Proposed ANN Determination Procedure Overview

The overview of the proposed method in a flow diagram is shown as in Fig. 5.1.

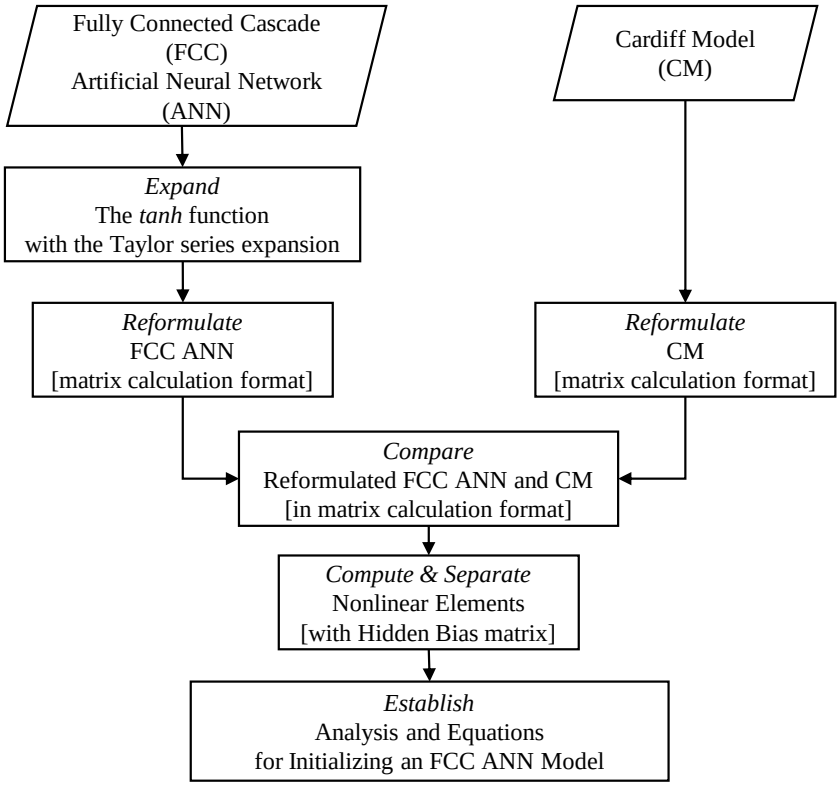

Figure 5.1: Flow diagram summarizing the procedure used to establish the equivalence between ANN and CM coefficients.

It follows these steps in detail:

1. Based on the fact that ANNs require complex numbers to be processed with the real and imaginary parts separated, the CM (structure diagram shown

in Fig. 5.2) needs to be reformulated to accommodate the separation of the complex variables (following the details explained in Step 1).

2. A single hidden layer structure ANN model [13] (conventional structure in Fig. 5.5) is reformulated, with the Taylor series expansion being applied to replace the tanh activation function. This provides a better understanding of how an ANN's structure operates on non-linear segments from layer to layer with the tanh activation function.

3. Following the details explained in Step 2, it is important to note that the tanh function generates both linear and constant terms as well as higher-order terms. To account for the linear and constant terms, a Fully Connected Cascaded (FCC) ANN structure is selected to ensure accurate prediction (interpolation) of measured results. It is the higher order terms that contribute to an improved extrapolation ability [14], [15].

4. After the ANN and CM models have been reformulated, their elements are matched to establish a new set of equations for identifying the required FCC ANN model configuration.

5. Finally, the proposed method for determining an FCC ANN model parameters is derived.

5.1.1 Step 1: Cardiff Model (CM) Equations Reformulation

The conventional CM mathematically relates the input and output power waves of the device through a set of model coefficients '$M_{p,h,m,n}$' [16], [17]. The formulation for datasets that is phase normalized to the complex exponential of the phase of $A_{1,1}$ for fundamental load-pull measurement datasets is as shown in (5.1):

$$B_{p,h} = \sum_{r=0}^{r=1} \sum_{n=0}^{n} M_{p,h,m,n} |A_{2,1}|^m \left(\angle A_{2,1}\right)^n \tag{5.1}$$

where $\angle A_{2,1}$ represents the complex exponential of the phase of $A_{2,1}$, the 'p' and 'h' subscripts denote the respective port and harmonics.

The choice of exponents is driven by mixing theory, which makes the model physically meaningful. Here in (5.1), the exponents 'm' and 'n' denote the coefficient-related power wave's magnitude and the complex exponential of the phase respectively. The 'm' and 'n' terms are related as '$m = |n| + 2r$', where 'r' is the magnitude indexing term is limited to integer values from 0 to 1 because of extrapolation concerns [16]–[18]. The simple CM diagram can be shown in Fig. 5.2.

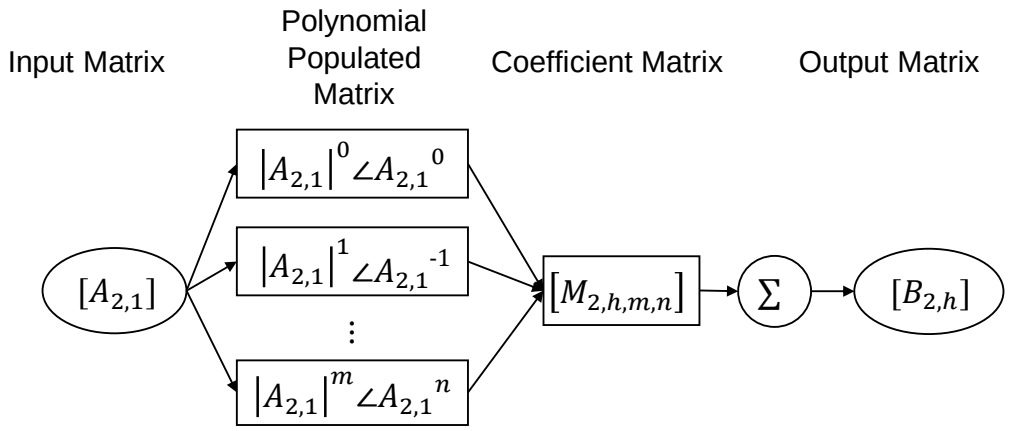

Figure 5.2: Conventional CM model diagram.

If propagating magnitude and phase exponent terms 'm' and 'n' follow a polynomial order instead of the standard CM mixing order, the conventional CM formulation (5.1) can be expanded and rearranged as follows from '$M_{p,h,0,0}$' to the general expansion limit '$M_{p,h,m,n}$':

$$
\begin{aligned}
B_{p,h} = {} & M_{p,h,0,0} + M_{p,h,1,1}A_{2,1} + M_{p,h,1,-1}A_{2,1}^{*} \\
& + M_{p,h,2,2}\left(A_{2,1}\right)^{2} + 2M_{p,h,2,0}A_{2,1}A_{2,1}^{*} + M_{p,h,2,-2}\left(A_{2,1}^{*}\right)^{2} \\
& + M_{p,h,3,3}\left(A_{2,1}\right)^{3} + 3M_{p,h,3,1}\left(A_{2,1}\right)^{2}\left(A_{2,1}^{*}\right) \\
& + 3M_{p,h,3,-1}A_{2,1}\left(A_{2,1}^{*}\right)^{2} + M_{p,h,3,-3}\left(A_{2,1}^{*}\right)^{3} \\
& \vdots \\
& + \begin{bmatrix} \dots & M_{p,h,m,n} & \dots \end{bmatrix} \cdot \begin{bmatrix} \vdots \\ \binom{m}{k}\left(A_{2,1}\right)^{m-k}\left(A_{2,1}^{*}\right)^{k} \\ \vdots \end{bmatrix}
\end{aligned}
\tag{5.2}
$$

where the value of 'n', which is the phase exponent term, can now be calculated with '$n = m - 2k$'. The value of 'm' equals to the polynomial order number [11] and 'k' ranges from 0 to 'm'. '$\left(A_{2,1}^{*}\right)$' represents the conjugate operation of $A_{2,1}$. The positive integer is known as the binomial coefficient:

$$
\binom{m}{k} = \frac{m!}{k!(m-k)!} \tag{5.3}
$$

Rearranging (5.2) into matrix form with real and imaginary parts separated, the $\begin{bmatrix} B_{p,h}^{R} \\ B_{p,h}^{I} \end{bmatrix}$ matrix can be calculated following the expansion of the dot product from matrices:

$$
\begin{bmatrix} \dots & \left(M_{p,h,m,n}^{R} + jM_{p,h,m,n}^{I}\right) & \dots \end{bmatrix}
$$

and

$$
\begin{bmatrix} \vdots \\ \binom{m}{k}\left(A_{2,1}^{R} + jA_{2,1}^{I}\right)^{m-k}\left(A_{2,1}^{R} - jA_{2,1}^{I}\right)^{k} \\ \vdots \end{bmatrix}.
$$

Hence, the formulation can be written with the binomial coefficients in the $A_{2,1}$ matrix expansion folded into the CM coefficients matrices, as (5.4).

Having the '$A_{2,1}$' stimulus incident waves separated into real and imaginary parts, the CM can be reformulated as (5.4).

$$\begin{aligned}\begin{bmatrix} B^R_{p,h} \\ B^I_{p,h} \end{bmatrix} = \begin{bmatrix} M_0 \end{bmatrix} + \begin{bmatrix} M_1 \end{bmatrix} \begin{bmatrix} A^R_{2,1} \\ A^I_{2,1} \end{bmatrix} + \begin{bmatrix} M_2 \end{bmatrix} \begin{bmatrix} \left(A^R_{2,1}\right)^2 \\ A^R_{2,1} A^I_{2,1} \\ \left(A^I_{2,1}\right)^2 \end{bmatrix} \\ + \begin{bmatrix} M_3 \end{bmatrix} \begin{bmatrix} \left(A^R_{2,1}\right)^3 \\ \left(A^R_{2,1}\right)^2 A^I_{2,1} \\ A^R_{2,1} \left(A^I_{2,1}\right)^2 \\ \left(A^I_{2,1}\right)^3 \end{bmatrix} + \cdots + \begin{bmatrix} M_o \end{bmatrix} \begin{bmatrix} \vdots \\ (A^R_{2,1})^{m-k} (A^I_{2,1})^k \\ \vdots \end{bmatrix}\end{aligned} \tag{5.4}$$

where 'R' and 'I' represent the real and imaginary parts of the complex data segments, the $[M_o]$ matrix is computed from sets of model coefficient '$M_{p,h,m,n}$', exponent pairs (m, n), associated with the respective mixing order [11], and 'k' ranges from 0 to 'o', where 'o' represents the expanded polynomial order.

In (5.4), the $[M_o]$ matrices with o as the polynomial order equals up to 3 are shown in the following as examples:

$$\begin{bmatrix} M_0 \end{bmatrix} = \begin{bmatrix} M^R_{p,h,0,0} \\ M^I_{p,h,0,0} \end{bmatrix} \tag{5.5}$$

$$\begin{bmatrix} M_1 \end{bmatrix} = \begin{bmatrix} \left(M^R_{p,h,1,1} + M^R_{p,h,1,-1}\right) & \left(-M^I_{p,h,1,1} + M^I_{p,h,1,-1}\right) \\ \left(M^I_{p,h,1,1} + M^I_{p,h,1,-1}\right) & \left(M^R_{p,h,1,1} - M^R_{p,h,1,-1}\right) \end{bmatrix} \tag{5.6}$$

$$\left[M_2\right] = \begin{bmatrix} \left(M^R_{p,h,2,2}+M^R_{p,h,2,0}+M^R_{p,h,2,-2}\right) & 2.\left(-M^I_{p,h,2,2}+M^I_{p,h,2,-2}\right) & \left(-M^R_{p,h,2,2}+M^R_{p,h,2,0}-M^R_{p,h,2,-2}\right) \\ \left(M^I_{p,h,2,2}+M^I_{p,h,2,0}+M^I_{p,h,2,-2}\right) & 2.\left(-M^R_{p,h,2,2}-M^R_{p,h,2,-2}\right) & \left(-M^I_{p,h,2,2}+M^I_{p,h,2,0}-M^I_{p,h,2,-2}\right) \end{bmatrix} \tag{5.7}$$

$$\begin{aligned} \left[M_3\right] = \begin{bmatrix} \left(M^R_{p,h,3,3}+M^R_{p,h,3,1}+M^R_{p,h,3,-1}+M^R_{p,h,3,-3}\right) \\ \left(M^I_{p,h,3,3}+M^I_{p,h,3,1}+M^I_{p,h,3,-1}+M^I_{p,h,3,-3}\right) \end{bmatrix} \\ \left(-3M^I_{p,h,3,3}-M^I_{p,h,3,1}+M^I_{p,h,3,-1}+3M^I_{p,h,3,-3}\right) \\ \left(3M^R_{p,h,3,3}+M^R_{p,h,3,1}-M^R_{p,h,3,-1}-3M^R_{p,h,3,-3}\right) \\ \left(-3M^R_{p,h,3,3}+M^R_{p,h,3,1}+M^R_{p,h,3,-1}-3M^R_{p,h,3,-3}\right) \\ \left(-3M^I_{p,h,3,3}+M^I_{p,h,3,1}+M^I_{p,h,3,-1}-M^I_{p,h,3,-3}\right) \\ \begin{bmatrix} \left(M^I_{p,h,3,3}-M^I_{p,h,3,1}+M^I_{p,h,3,-1}-M^I_{p,h,3,-3}\right) \\ \left(-M^R_{p,h,3,3}+M^R_{p,h,3,1}-M^R_{p,h,3,-1}+M^R_{p,h,3,-3}\right) \end{bmatrix} \end{aligned} \tag{5.8}$$

The reformulated CM equation (5.4) can also be presented by the structure diagram shown in Fig. 5.3.

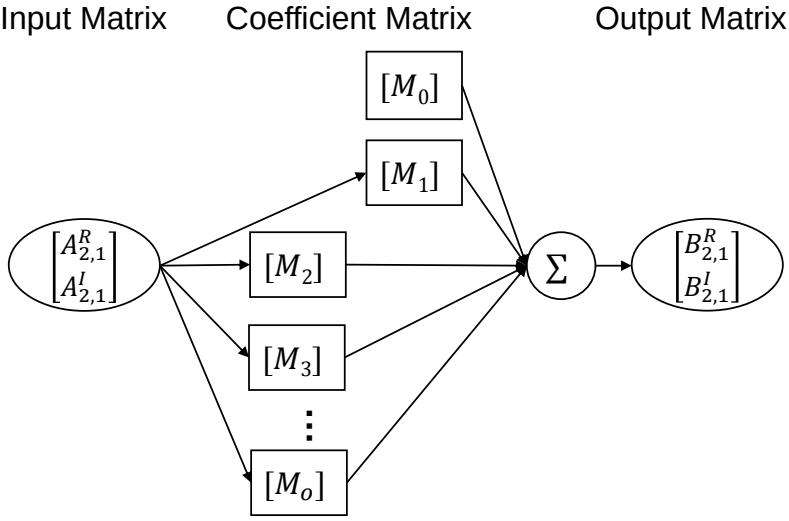

Figure 5.3: Diagram of the CM model reformulated for Real and Imaginary parts.

5.1.2 Step 2: General ANN Equations Reformulation

Before moving on to a FCC ANN model structure, a general simplest ANN model structure shown in Fig. 5.5, is first presented with Fig. 5.4. Based on the previous experiments, the ANN-based behavioural model necessitates having any input and output matrices split from the complex form into separate real and imaginary matrices. The model in the diagram gives rise to the following mathematical formulation (5.9).

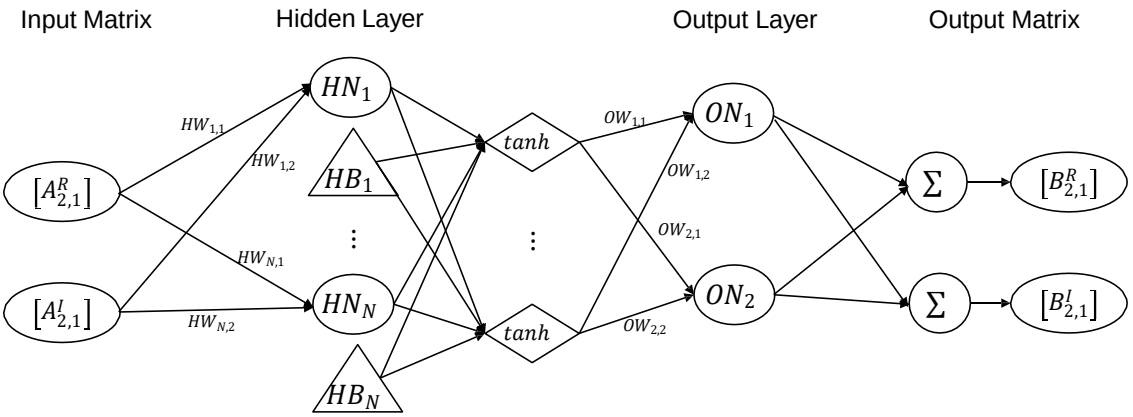

Figure 5.4: Conventional ANN model diagram.

$$\begin{bmatrix} B^R_{p,h} \\ B^I_{p,h} \end{bmatrix} = [OW] \tanh \left([HW] \begin{bmatrix} A^R_{2,1} \\ A^I_{2,1} \end{bmatrix} + [HB] \right) \tag{5.9}$$

where 'R' and 'I' are the abbreviations of real and imaginary parts of the complex data segments, while parameters '$[HW]$', '$[HB]$' and '$[OW]$' represent the number of hidden weights, hidden biases, and output weights respectively. With the $[HB]$ given by:

$$[HB] = \begin{bmatrix} HB_{1,1} \\ \vdots \\ HB_{NH,1} \end{bmatrix} \tag{5.10}$$

the $[HW]$ given by:

$$[HW] = \begin{bmatrix} HW_{1,1} & HW_{1,2} \\ \vdots & \\ HW_{NH,1} & HW_{NH,2} \end{bmatrix}. \tag{5.11}$$

and the $[OW]$ given by:

$$[OW] = \begin{bmatrix} OW_{1,1} & \cdots & OW_{1,NH} \\ OW_{2,1} & \cdots & OW_{2,NH} \end{bmatrix}. \tag{5.12}$$

The equation can then be structured into a matrix format diagram for the conventional ANN model in Fig. 5.5.

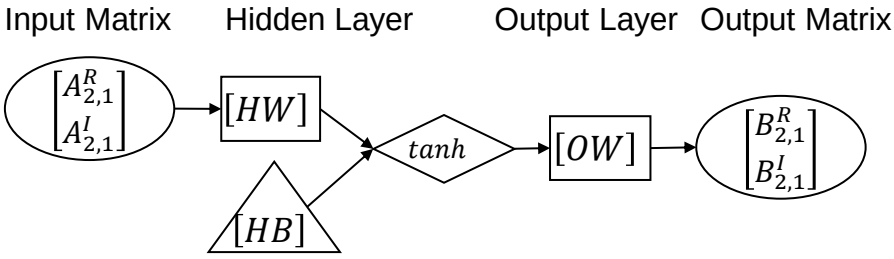

Figure 5.5: Conventional ANN model diagram in matrix format.

Inside the ANN structure, the non-linear transfer characteristic function tanh, also called the activation function [19], is the key to creating non-linearity within any ANN system. By formulating the tanh activation function with its Taylor series expansion, the non-linearity terms can be separated clearly for ANN determination analysis, and can then be compared with the reformulated CM formulation later.

The tanh function is defined as:

$$\tanh(\underline{x}) = \frac{2}{1 + e^{-2(\underline{x})}} - 1 \tag{5.13}$$

Following the Taylor series expansion theory:

$$f(x) \cong f(x_0) + \frac{f'(x_0)}{1!}(x - x_0) + \frac{f''(x_0)}{2!}(x - x_0)^2 + \frac{f'''(x_0)}{3!}(x - x_0)^3 + ... \tag{5.14}$$

The tanh function part in (5.9) can be reformulated as:

$$\tanh\left([HW]\begin{bmatrix}A_{2,1}^{R}\\ \\ A_{2,1}^{I}\end{bmatrix}+[HB]\right)=[\alpha]+\Delta[\alpha][HW]\begin{bmatrix}A_{2,1}^{R}\\ \\ A_{2,1}^{I}\end{bmatrix}+\Delta^{2}[\alpha]\left[HW^{2}\right]\begin{bmatrix}\left(A_{2,1}^{R}\right)^{2}\\ A_{2,1}^{R}A_{2,1}^{I}\\ \left(A_{2,1}^{I}\right)^{2}\end{bmatrix}$$
$$+\Delta^{3}[\alpha]\left[HW^{3}\right]\begin{bmatrix}\left(A_{2,1}^{R}\right)^{3}\\ \left(A_{2,1}^{R}\right)^{2}A_{2,1}^{I}\\ A_{2,1}^{R}\left(A_{2,1}^{I}\right)^{2}\\ \left(A_{2,1}^{I}\right)^{3}\end{bmatrix}$$
$$+\cdots+\Delta^{o}[\alpha]\left[HW^{o}\right]\begin{bmatrix}\vdots\\ (A_{2,1}^{R})^{o-k}(A_{2,1}^{I})^{k}\\ \vdots\end{bmatrix} \tag{5.15}$$

where:

$$[\alpha]=\tanh([HB]) \tag{5.16}$$

$$\Delta^{o}[\alpha]=\frac{1}{o!}\frac{\tanh^{o}([HB])}{([HB])^{o}}. \tag{5.17}$$

According to (5.16) and (5.17), the $[HB]$ matrices can be calculated and shown in detail with a polynomial order equals up to 3 :

$$\Delta[\alpha]=\frac{\tanh'([HB])}{([HB])}=\operatorname{sech}^{2}([HB]) \tag{5.18}$$

$$\Delta^{2}[\alpha]=\frac{1}{2}\frac{\tanh''([HB])}{([HB])^{2}}=-\tanh([HB])\operatorname{sech}^{2}([HB]) \tag{5.19}$$

$$\Delta^{3}[\alpha]=\frac{1}{6}\frac{\tanh'''([HB])}{([HB])^{3}}=\frac{\operatorname{sech}^{2}([HB])}{3}\{\tanh^{2}([HB])-\operatorname{sech}^{2}([HB])\} \tag{5.20}$$

Therefore, the original ANN model equation shown in (5.9) can now be reformulated as follows:

$$\begin{bmatrix} B^R_{p,h} \\ B^I_{p,h} \end{bmatrix} = [OW]\,[\alpha] + [OW]\,\Delta\,[\alpha]\,[HW] \begin{bmatrix} A^R_{2,1} \\ A^I_{2,1} \end{bmatrix} + [OW]\,\Delta^2\,[\alpha]\,\left[HW^2\right] \begin{bmatrix} \left(A^R_{2,1}\right)^2 \\ A^R_{2,1}A^I_{2,1} \\ \left(A^I_{2,1}\right)^2 \end{bmatrix}$$
$$+ [OW]\,\Delta^3\,[\alpha]\,\left[HW^3\right] \begin{bmatrix} \left(A^R_{2,1}\right)^3 \\ \left(A^R_{2,1}\right)^2 A^I_{2,1} \\ A^R_{2,1}\left(A^I_{2,1}\right)^2 \\ \left(A^I_{2,1}\right)^3 \end{bmatrix}$$
$$+ \cdots + [OW]\,\Delta^o\,[\alpha]\,[HW^o] \begin{bmatrix} \vdots \\ (A^R_{2,1})^{o-k}(A^I_{2,1})^k \\ \vdots \end{bmatrix} \tag{5.21}$$

Since the defined FCC ANN model deals with datasets that consist of real and imaginary pairs, the two elements in (5.11) associated with each hidden neuron in the $[HW]$ matrix, will also represent the real and imaginary parts of the same complex number. Hence, $[HW]$ can be re-written as follows:

$$[HW] = \begin{bmatrix} \rho_1 \cos\theta_1 & \rho_1 \sin\theta_1 \\ \vdots & \\ \rho_{NH} \cos\theta_{NH} & \rho_{NH} \sin\theta_{NH} \end{bmatrix} \tag{5.22}$$

Defining the $[HW]$ matrix in the polar form provides an easier way to explore possible suitable values. This format is then used to determine corresponding $[HW^o]$ matrices:

$$[HW^{o}] = \begin{bmatrix} \rho_1 & 0 & \dots & 0 \\ \vdots & & \ddots & \vdots \\ 0 & \dots & 0 & \rho_{NH} \end{bmatrix} \begin{bmatrix} \dots & \binom{o}{k} (\cos\theta_1)^{o-k} (\sin\theta_1)^{k} & \dots \\ & \vdots & \\ \dots & \binom{o}{k} (\cos\theta_{NH})^{o-k} (\sin\theta_{NH})^{k} & \dots \end{bmatrix} \tag{5.23}$$

Note, the expansion of $[HW^{o}]$ matrix follows the binomial theorem. 'k' ranges from 0 to o, and 'o' refers to the polynomial order number. The positive integer is known as the binomial coefficient as:

$$\binom{o}{k} = \frac{o!}{k!(o-k)!} \tag{5.24}$$

The $[HW^{o}]$ can then be simply computed (5.25).

$$[HW^{o}] = \begin{bmatrix} [\rho_1(\cos\theta_1 + \sin\theta_1)]^{o} \\ \vdots \\ [\rho_{NH}(\cos\theta_{NH} + \sin\theta_{NH})]^{o} \end{bmatrix} \tag{5.25}$$

Here in (5.25), since 'ρ_{NH}' is set to limit the spread range of when the data is biased on the tanh activation function without exceeding a proper coverage range according to the non-linearity, it will be defined respectively unrelated to the phase angles when analysing the values of the $[HW]$ matrix. 'NH' here represents the number of hidden neurons used in the ANN structure.

It must be noted that the constant and linear elements inside the Taylor series reformulated ANN model will not be independent of the higher-order non-linearities. Hence, analysis done on the Taylor Series expansion starts from the higher order elements, respectively, because the parameters ('$[HW]$', '$[HB]$' and '$[OW]$') are shared

between linear and non-linear elements, so lower order elements will be affected by the higher order elements due to the calculation operation order. Therefore, extra weight '$[CW]$' (Cascaded Weights) and bias matrices '$[OB]$' (Output Bias) will be required for correcting the constant and linear elements provided by the Taylor series expansion.

5.1.3 Step 3: FCC ANN Equations Reformulation

The Knowledge-based Neural Network (KBNN) structure, which can also be simplified to be an FCC ANN structure with one hidden layer, has been proven more robust than the multilayer perceptron (MLP) structure [14], especially when the dataset is insufficient. The general ANN structure in Fig. 5.5, is then transformed into an FCC ANN structure [8] for a possible accurate model with reasonable extrapolation ability shown in Fig. 5.6.

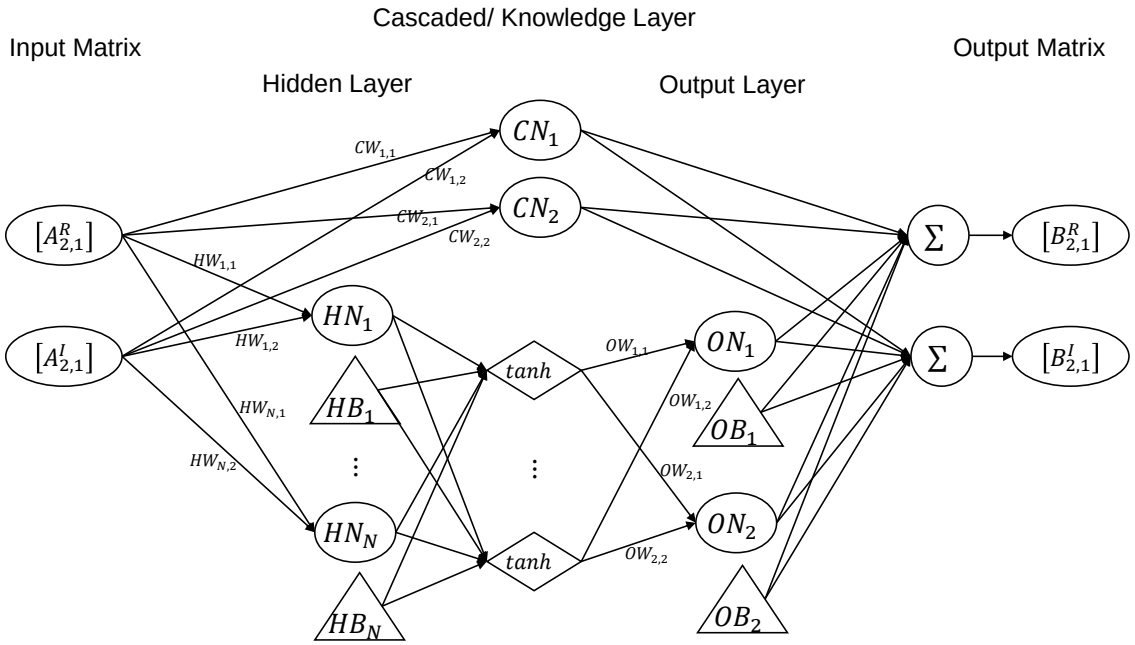

Figure 5.6: FCC ANN model diagram.

The diagram executes the mathematical formulation as (5.26), which can then be

translated into a matrix format FCC ANN model diagram as in Fig. 5.7.

$$\begin{bmatrix} B^R_{p,h} \\ B^I_{p,h} \end{bmatrix} = [OB] + [CW] \begin{bmatrix} A^R_{2,1} \\ A^I_{2,1} \end{bmatrix} + [OW] \tanh \left([HW] \begin{bmatrix} A^R_{2,1} \\ A^I_{2,1} \end{bmatrix} + [HB] \right) \tag{5.26}$$

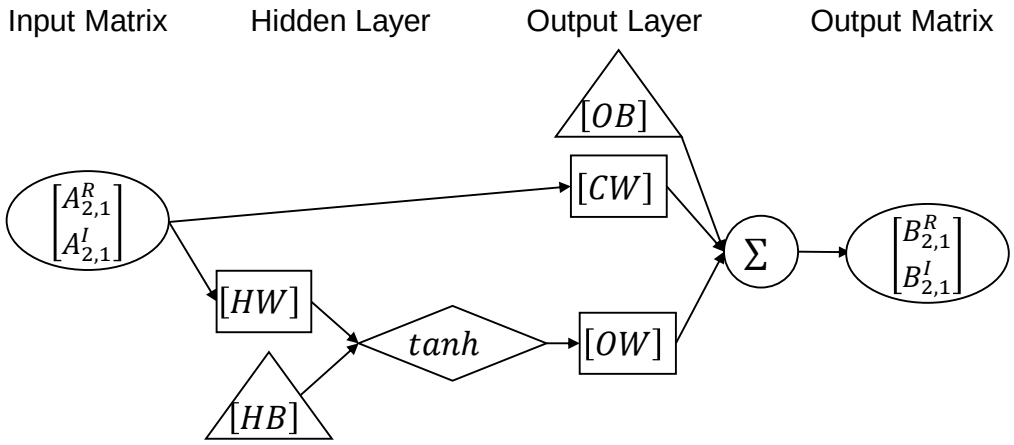

Figure 5.7: FCC ANN model diagram.

The added extra weights and biases are brought in by the FCC ANN structure can be utilised for correcting the dependent constant and linear element, generated by analyzing the 2^{nd} and 3^{rd} order respectively, inside the reformulated expanded equation in (5.21). The original format of an FCC ANN equation (5.26) will then be reformulated as (5.27).

$$
\begin{aligned}
\begin{bmatrix} B^R_{p,h} \\ B^I_{p,h} \end{bmatrix} &= ([OB] + [OW]\,[\alpha]) \\
&+ ([CW] + [OW]\,\Delta\,[\alpha]\,[HW]) \begin{bmatrix} A^R_{2,1} \\ A^I_{2,1} \end{bmatrix} \\
&+ [OW]\,\Delta^2\,[\alpha]\,\left[HW^2\right] \begin{bmatrix} \left(A^R_{2,1}\right)^2 \\ A^R_{2,1}A^I_{2,1} \\ \left(A^I_{2,1}\right)^2 \end{bmatrix} \\
&+ [OW]\,\Delta^3\,[\alpha]\,\left[HW^3\right] \begin{bmatrix} \left(A^R_{2,1}\right)^3 \\ \left(A^R_{2,1}\right)^2 A^I_{2,1} \\ A^R_{2,1}\left(A^I_{2,1}\right)^2 \\ \left(A^I_{2,1}\right)^3 \end{bmatrix} \\
&+ \cdots + [OW]\,\Delta^o\,[\alpha]\,[HW^o] \begin{bmatrix} \vdots \\ (A^R_{2,1})^{o-k}(A^I_{2,1})^k \\ \vdots \end{bmatrix}
\end{aligned}
\tag{5.27}
$$

By using the matrices formulation, shown in (5.27), the FCC ANN structure can be re-drawn as shown in Fig. 5.8. It is now clear how the levels of non-linearity in the system are being processed by different weights and biases inside the FCC ANN model. A direct comparison can now be done between the reformulated CM (Fig. 5.3) and the FCC ANN model (Fig. 5.8).

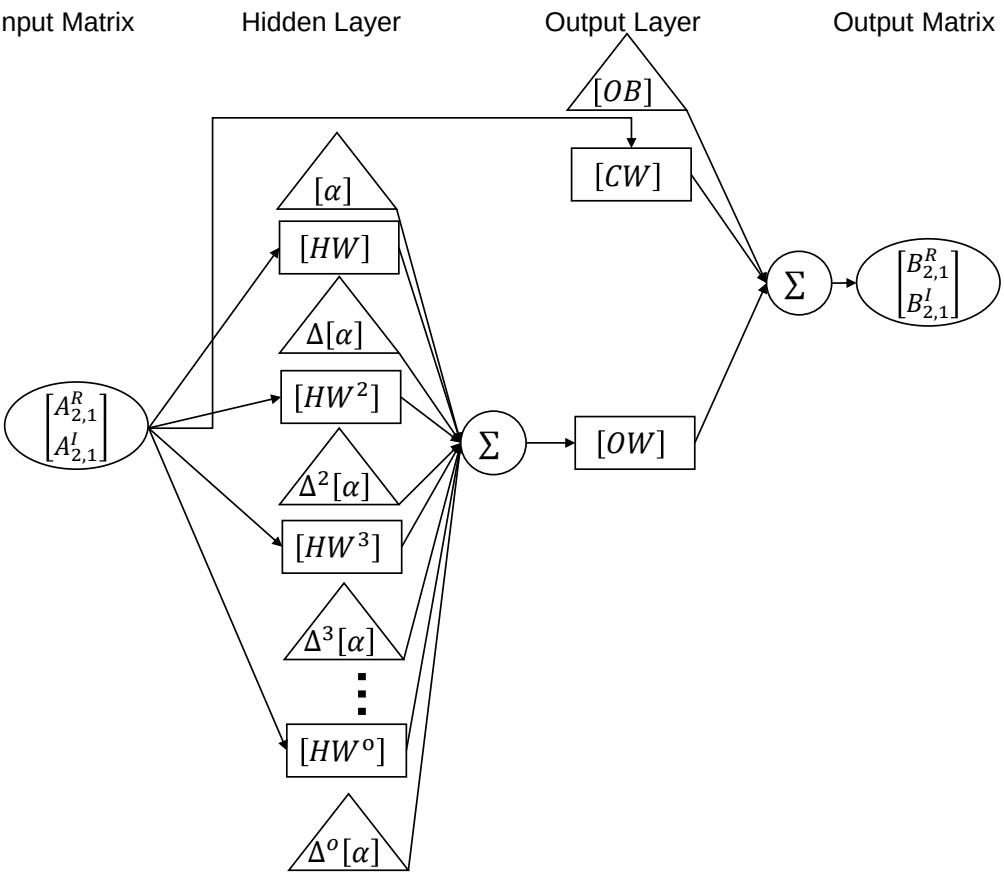

Figure 5.8: Reformulated FCC ANN model diagram.

5.1.4 Step 4: Equating Formulations and ANN Model Structure Identification

Comparison can now be analysed with equations (5.4) and (5.27), and also Fig. 5.3 and 5.8. When observing the structure of both models, as in Fig. 5.5 and 5.3, the similarities between the two model structures can be seen. The coefficient matrix columns in Fig. 5.3 can fulfill a similar process as the hidden layer and output layer in Fig. 5.5.

The non-linearities inside the two systems can be equated as follows: where the first line of the matrices' calculation in (5.27) will match with the constant $[M_0]$ matrix in (5.4); the second line of the matrices' calculation in (5.27) is generating the fundamental part of the response; and the 2^{nd} and 3^{rd} order responding output non-

linearities are generated by the third and fourth row of the matrices' multiplication in (5.27), respectively. Hence, a set of equations (5.28) - (5.32) can be extracted by equating the linear and non-linear terms inside the calculation processes:

$$[M_0] = [OB] + [OW]\,[\alpha] \tag{5.28}$$

$$[M_1] = [CW] + [OW]\,\Delta\,[\alpha]\,[HW] \tag{5.29}$$

$$[M_2] = [OW]\,\Delta^2\,[\alpha]\,\left[HW^2\right] \tag{5.30}$$

$$[M_3] = [OW]\,\Delta^3\,[\alpha]\,\left[HW^3\right] \tag{5.31}$$

$$\vdots$$

$$[M_o] = [OW]\,\Delta^o\,[\alpha]\,[HW^o] \tag{5.32}$$

These equations provide a method for linking CM complexity and coefficients to FCC ANN model structure and parameters.

By knowing the number and dimensions of the $[M_o]$ matrices required from the identified CM, the associated ANN matrices dimensions, $[OW]$, $[HB]$ and $[HW]$, necessary to ensure that the matrix equations (5.28) - (5.32) are self-consistent, can now be determined. The ANN structure with the required hidden neuron number can now be directly identified, by analyzing load-pull data complexity using the CM. Consider the case where the accurate modelling of the load-pull data is found to require a 3^{rd} order non-linear CM [16]. In this case, we need an ANN structure that can satisfy (5.28) - (5.31). Following the contribution of the non-linearities inside the expanded ANN structure, the higher order non-linearities segment will be analysed first, by solving (5.30) - (5.31), then the linear segment can be calculated, by solving (5.28) - (5.29).

The size of the $[M_2]$ matrix, given by the CM, in this case, is $[2 \times 3]$. Hence, the matrices dimensions on the right-hand side of (5.30), $[OW]\,\Delta^2\,[\alpha]\,[HW^2]$, must also

result in a $[2 \times 3]$ matrix, hence implying an ANN structure with 3 hidden neurons. There is the same scenario for solving (5.31). The size of the $[M_3]$ matrix, given by the CM, is $[2 \times 4]$. Hence the $[OW]\,\Delta^3\,[\alpha]\,[HW^3]$ product must also result in a $[2 \times 4]$ matrix, implying an ANN structure with 4 hidden neurons. However, in a given FCC ANN model the number of hidden neurons is a single value, hence different sizes for the required weights ($[OW]$ and $[HW]$), and bias ($[HB]$) matrices is not possible. This can be addressed by using the sum of the two different matrix sizes which, in this case, leads to an FCC ANN structure with 7 hidden neurons.

In summary, it has been identified that an FCC ANN model with 7 hidden neurons is the maximum complexity necessary to model a 3^{rd} order non-linear system.

5.1.5 Step 5: FCC ANN Model Parameter determination

Now, the ANN model structure identification has been achieved. There is still a potential situation where the initial values of the ANN model parameters lead to a non-converging backpropagation training process. Therefore, having properly determined values of the ANN model parameters $[OW]$, $[HB]$ and $[HW]$ can be helpful for the training process. However, it is not possible to compute the ANN model parameters, the three matrices $[OW]$, $[HB]$ and $[HW]$, directly from the CM by simply reversing equations (5.28) - (5.31). Two of the ANN model matrices have to be predetermined. Following the feed forward process of the ANN structure, the first set of matrices that should be defined are matrix $[HB]$, and $[HW]$. Once determined, $[OW]$ can then be computed directly using equations (5.33) and/or (5.34).

$$[OW] = [M_2]\left[\Delta^2\,[\alpha]\left[HW^2\right]\right]^{-1} \tag{5.33}$$

$$[OW] = [M_3]\left[\Delta^3\,[\alpha]\left[HW^3\right]\right]^{-1} \tag{5.34}$$

The selection of $[HB]$ is critical to ensuring that equations (5.33) and (5.34) give

the same value of $[OW]$. It can be seen from the reformulated CM equation (5.4) that the $[M_2]$ matrix deals with the 2^{nd} order non-linearity and the $[M_3]$ matrix ideals with the 3^{rd} order non-linearity. To determine an FCC ANN using (5.30) and (5.31), according to the calculation through the tanh function, the $[HB]$ matrix can now be used to enable hidden neurons to target specific orders of non-linearity. The values of $\Delta^o[\alpha]$ matrices will be the key in this step.

The 3^{rd} order non-linear systems require an ANN model with 7 hidden neurons. Hence, $[HB]$ and $[HW]$ are as follows:

$$[HB] = \begin{bmatrix} HB_{1,1} \\ HB_{2,1} \\ HB_{3,1} \\ HB_{4,1} \\ HB_{5,1} \\ HB_{6,1} \\ HB_{7,1} \end{bmatrix} \tag{5.35}$$

$$[HW] = \begin{bmatrix} HW_{1,1} & HW_{1,2} \\ HW_{2,1} & HW_{2,2} \\ HW_{3,1} & HW_{3,2} \\ HW_{4,1} & HW_{4,2} \\ HW_{5,1} & HW_{5,2} \\ HW_{6,1} & HW_{6,2} \\ HW_{7,1} & HW_{7,2} \end{bmatrix} \tag{5.36}$$

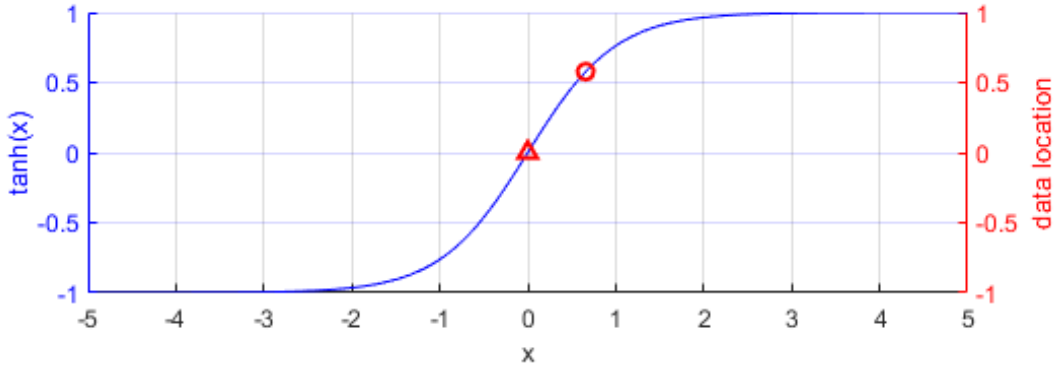

Figure 5.9: Selected bias point (red markers) locations on the tanh(x) function. Location when 3^{rd} order derivative equals 0 (circle) and location when 2^{nd} order derivative equals 0 (triangle).

Referring to the Taylor series expansion of the tanh function, (5.15), if an element of matrix $[HB]$ is set to 0.6585 (bias point Fig. 5.9-circle marker) then the 3^{rd} order element will be cancelled, because the corresponding element of matrix $\Delta^3[\alpha]$ is 0; alternatively when an element of matrix $[HB]$ equals 0 (bias point Fig. 5.9-triangle marker), then the 2^{nd} order element will be cancelled because the corresponding element of matrix $\Delta^2[\alpha]$ is 0.

Hence, using the required matrix sizes, mentioned in step 4, set the values of $[HB]$ matrix elements as follows:

$$[HB] = \begin{bmatrix} HB_{1,1} \\ HB_{2,1} \\ HB_{3,1} \\ HB_{4,1} \\ HB_{5,1} \\ HB_{6,1} \\ HB_{7,1} \end{bmatrix} = \begin{bmatrix} 0.6585 \\ 0.6585 \\ 0.6585 \\ 0 \\ 0 \\ 0 \\ 0 \end{bmatrix} \tag{5.37}$$

hence

$$\left[\Delta^2[\alpha]\right] = \begin{bmatrix} 0.38 \\ 0.38 \\ 0.38 \\ 0 \\ 0 \\ 0 \\ 0 \end{bmatrix} \tag{5.38}$$

and

$$\left[\Delta^3[\alpha]\right] = \begin{bmatrix} 0 \\ 0 \\ 0 \\ -0.33 \\ -0.33 \\ -0.33 \\ -0.33 \end{bmatrix} \tag{5.39}$$

The FCC ANN structure for 2^{nd} and 3^{rd} order non-linear contributions have now been separated and assigned to hidden neurons[1-3] and [4-7] respectively. There is now no requirement to solve (5.33) and (5.34) simultaneously. They can be reformulated as follows:

$$[OW_2] = 0.38\,[M_2]\left[HW_2^2\right]^{-1} \tag{5.40}$$

$$[OW_3] = -0.33\,[M_3]\left[HW_3^3\right]^{-1} \tag{5.41}$$

where the $[HW]$ and $[OW]$ have been separated into two parts based on the non-linear order, as follows:

$$[HW] = \begin{bmatrix} HW_2 \\ HW_3 \end{bmatrix} \tag{5.42}$$

and

$$[OW] = \begin{bmatrix} OW_2 & OW_3 \end{bmatrix} \tag{5.43}$$

Segment Analysis for the 2^{nd} Order

Analytical solutions for the 2^{nd} order segment are achievable if (5.40) can be solved, which then require the $[HW_2^2]$ matrix to be an invertible square matrix, provided it is non-singular. Since the defined dimension of the $[M_2]$ matrix (5.7) refers to a 3 hidden neurons situation, then $[HW_2^2]$, shown below, is a square matrix.

$$\left[HW_2^2\right] = \begin{bmatrix} \rho & 0 & 0 \\ 0 & \rho & 0 \\ 0 & 0 & \rho \end{bmatrix} \begin{bmatrix} \cos^2\theta_1 & 2\cos\theta_1\sin\theta_1 & \sin^2\theta_1 \\ \cos^2\theta_2 & 2\cos\theta_2\sin\theta_2 & \sin^2\theta_2 \\ \cos^2\theta_3 & 2\cos\theta_3\sin\theta_3 & \sin^2\theta_3 \end{bmatrix} \tag{5.44}$$

To make sure that (5.44) is a non-singular square matrix, the values of the 3 phase angles have to be selected to ensure the following conditions:

$$\begin{cases} \theta_1 \neq \theta_2 \pm p\pi \\ \\ \theta_2 \neq \theta_3 \pm q\pi \end{cases} \tag{5.45}$$

where p and q are any positive integer. For example, in this thesis, $\theta_1 = 45°$, $\theta_2 = 90°$ and $\theta_3 = 135°$ have been used.

Then the elements of the $[HW_2^2]$ matrix used in (5.40) can be calculated by selecting the value of ρ. The example in the method verification sections with specific datasets will discuss in detail the criteria for the selection of ρ.

Segment Analysis for the 3^{rd} Order

Similarly, an analytical solution for the 3^{rd} order segment, is achievable if (5.41) can be solved, which requires the $[HW_3^3]$ matrix to be an invertible square matrix, provided it is non-singular. Since the defined dimension of the $[M_3]$ matrix (5.8) refers to a 4 hidden neurons situation, then $[HW_3^3]$, shown below, is a square matrix.

$$\left[HW_3^3\right] = \begin{bmatrix} \rho & 0 & 0 & 0 \\ 0 & \rho & 0 & 0 \\ 0 & 0 & \rho & 0 \\ 0 & 0 & 0 & \rho \end{bmatrix} \begin{bmatrix} \cos^3\theta_4 & 3\cos^2\theta_4\sin\theta_4 & 3\cos\theta_4\sin^2\theta_4 & \sin^3\theta_4 \\ \cos^3\theta_5 & 3\cos^2\theta_5\sin\theta_5 & 3\cos\theta_5\sin^2\theta_5 & \sin^3\theta_5 \\ \cos^3\theta_6 & 3\cos^2\theta_6\sin\theta_6 & 3\cos\theta_6\sin^2\theta_6 & \sin^3\theta_6 \\ \cos^3\theta_7 & 3\cos^2\theta_7\sin\theta_7 & 3\cos\theta_7\sin^2\theta_7 & \sin^3\theta_7 \end{bmatrix} \tag{5.46}$$

To make sure that (5.46) is a non-singular matrix, also follows the conditions shown with (5.45) for all the four angles, for example, $\theta_4 = 36°$, $\theta_5 = 72°$, $\theta_6 = 108°$ and $\theta_7 = 144°$ are used in this thesis. Then the value of the $[HW_3^3]$ matrix used to solve (5.41) can be selected by sweeping the value of ρ, relating to the specific dataset.

In summary, it has been shown that the proper selection of the hidden node bias values allows for the allocation of hidden nodes to a specific non-linear order, thus enabling values of the FCC ANN model parameters to be directly computed from the corresponding CM coefficients '$M_{p,h,m,n}$'.

5.2 Method Verification With Simulations

In this section, a set of load-pull simulation data, with a complete 3^{rd} order data complexity, will be used as the first step for verifying the method using data that has a very low noise floor. The way of using the proposed method is summarized in the flow diagram, shown in Fig.5.10.

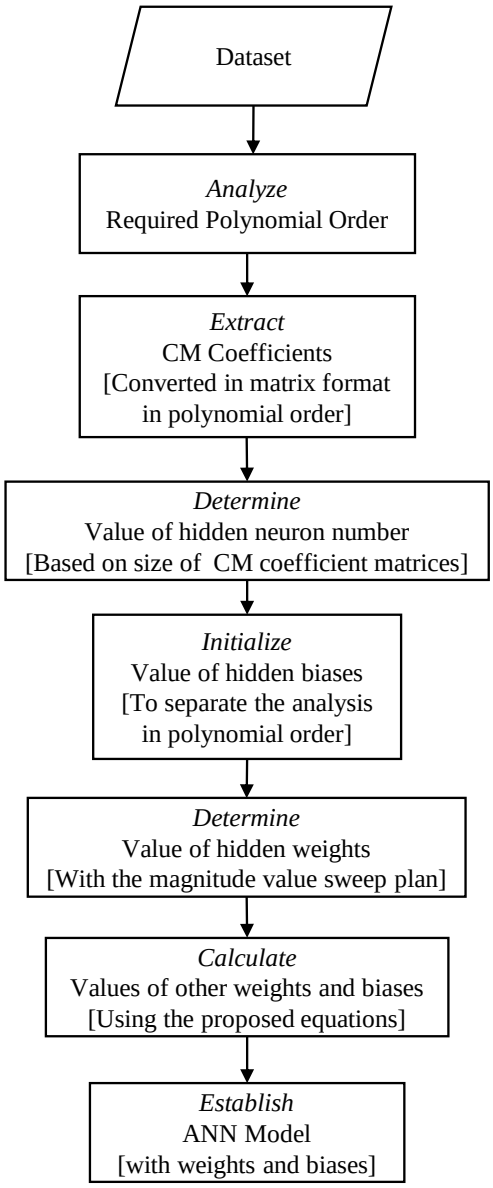

Figure 5.10: Flow diagram summarizing the proposed ANN determining method.

5.2.1 Simulation Data Acquisition

The same simulation setup as illustrated in Chapter 3 is utilised here for the load-pull simulation of the Wolfspeed 10 W device (CG2H40010F), biased at V_{gs} = -2.2 V, V_{ds} = 28 V. In Fig. 5.11-5.12, the data is collected with a constant input drive corresponding to 1 dB compression at the optimum load.

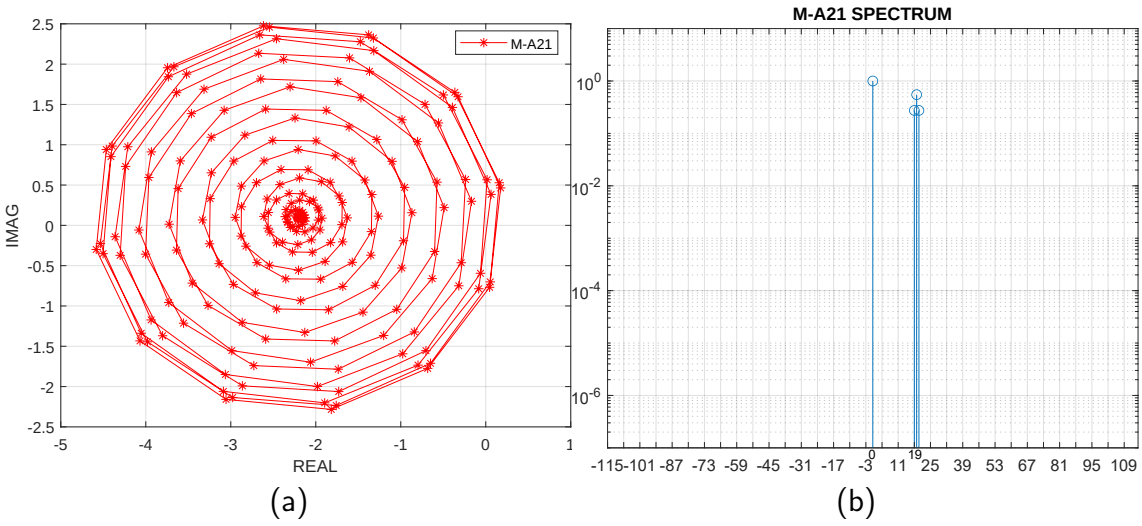

Figure 5.11: $A_{2,1}$ sample (a) and its Fourier Transformed spectrum (b) on a trajectory computed using 229 simulated points with the phase modulation rate of Sp = 19.

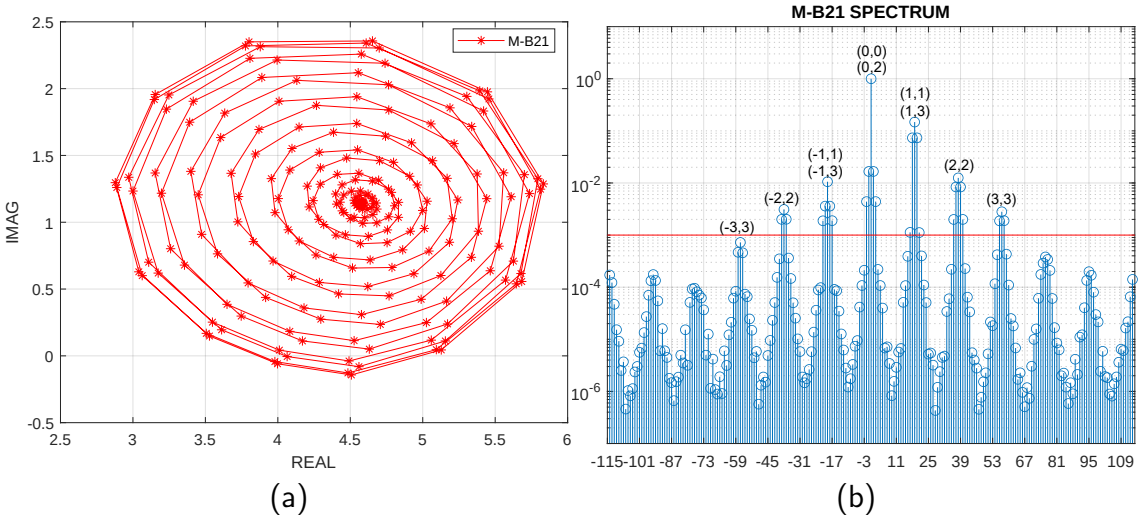

Figure 5.12: $B_{2,1}$ sample (b) and its Fourier Transformed spectrum (a) with error bar (red) on the trajectory computation, and the expected exponents' $|A_{2,1}|^m(\angle A_{2,1})^n$ values of the CM for extracting coefficients in (n,m).

According to the analysis in [16], 10 coefficients should be extracted here for an accurate CM with the -60 dB error threshold (red line in Fig. 5.12-right). Knowing that the ANN training process requires data normalization before feeding the data, the CM is extracted after normalizing the data based on the tanh function range, [-1 1]. The magnitude and phase-restricted terms exponents and the extracted coefficients are determined, calculated, and listed in Table,5.1. The performance of

the extracted CM will be discussed later in the next step.

Table 5.1: The Extracted CM Coefficients For $B_{2,1}$ of the Wolfspeed device

				$M_{2,1,m,n}$	
index	r	n	m	*Real*	*Imag.*
1	0	0	0	0.7597	0.1
2	0	1	1	-0.5608	-0.0748
3	0	-1	1	-0.0502	0.0390
4	0	2	2	0.0741	-0.1155
5	1	0	2	-0.2547	-0.1019
6	0	-2	2	0.0222	0.0247
7	1	3	3	-0.0638	-0.0333
8	1	1	3	0.0108	0.1137
9	0	-1	3	0.1177	-0.1419
10	0	-3	3	-0.0162	-0.0070

5.2.2 Method Created Model Analysis with ρ Sweep

According to the identified CM polynomial terms shown in Fig.5.12 using the analysis explained in [16], it is now clear that $[M_o]$ matrices with the value of 'm' up to 3 are all that are required to model this dataset. As defined in section 5.1.4, a dataset that requires a 3^{rd} order non-linear CM will determine a complete FCC ANN model structure as 1 hidden layer with 7 hidden neurons.

Following the analysis process in section 5.1.5, with the selected phase angles $\theta_1 = 45°$, $\theta_2 = 90°$ and $\theta_3 = 135°$ for $[HW_2]$ and $\theta_4 = 36°$, $\theta_5 = 72°$, $\theta_6 = 108°$ and $\theta_7 = 144°$ for $[HW_3]$, the determined value of $[HW]$ and $[OW]$ can be explored with the CM coefficients (listed in Table 5.1) and a magnitude element ρ sweep plan for this specific dataset.

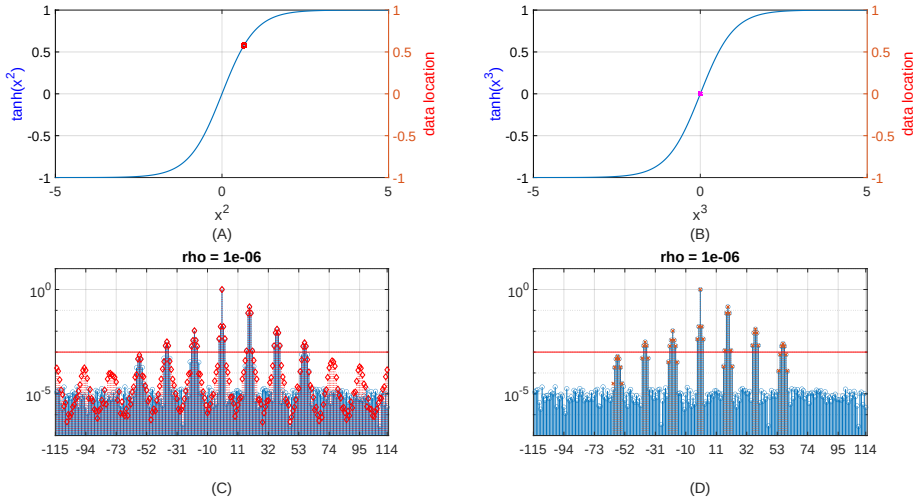

(a) $\rho = 0$

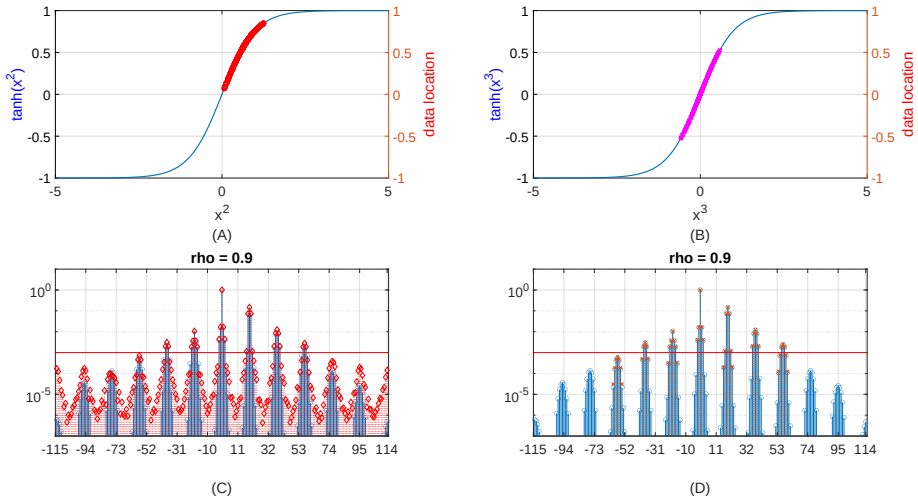

(b) $\rho = 0.9$

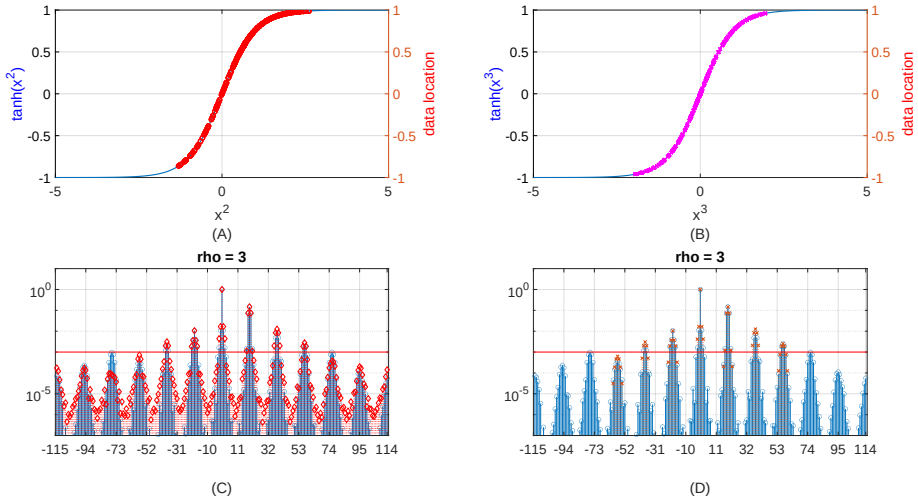

(c) $\rho = 3$

Figure 5.13: The dataset coverage on the $\tanh(x)$ function range without the $3^{rd}/2^{nd}$ order segment (A-B) location after determined weights and biases. The Fourier Transformed spectrum comparison plot (C-D) of the modelled $B_{2,1}$(blue) and the $B_{2,1}$ samples from the simulation (red) and the calculated from the CM (orange) with error bar (redline) on the trajectory computation.

The effect brought by the different values of ρ is shown in Fig.5.13 and 5.14. It can be seen from the figures that a bigger value of ρ results in a bigger coverage on the tanh function within the acquired dataset range (Fig.5.13(a)-(b)), which then generates a $B_{2,1}$ model with a more complex Fourier Transformed spectrum, hence an effective "higher noise floor" comparing to the collected dataset (Fig.5.13(c)) and the CM predictions (Fig.5.13(d)). Also, as shown in Fig.5.14(a), the performance of the determined ANN model and the CM gets identical when the value of ρ gets close to 0. Eventually, as ρ is swept from 0 up to 3, as shown in Fig.5.14(b), the accuracy of the model decreases.

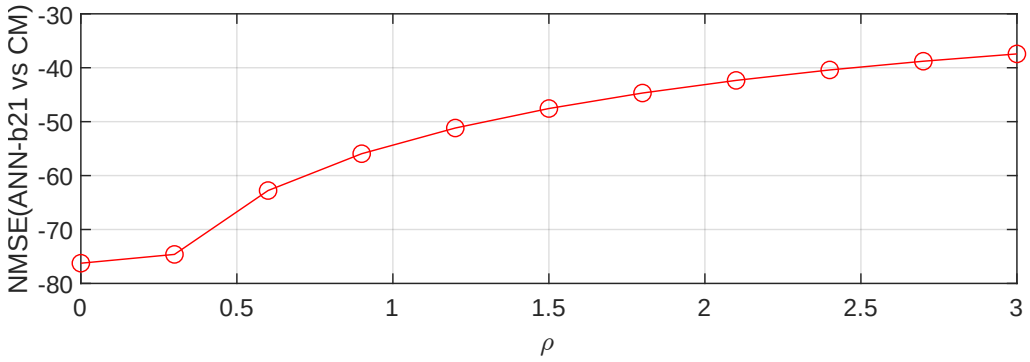

(a) NMSE from ANN prediction vs. Cardiff Model prediction

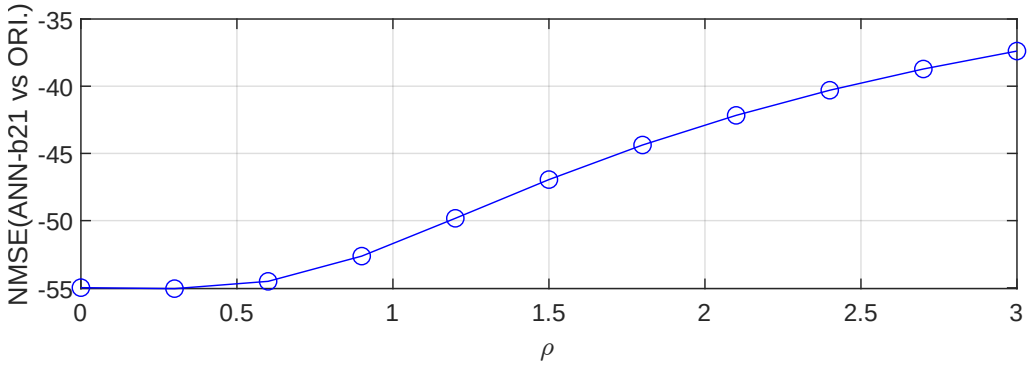

(b) NMSE from ANN prediction vs. Simulation data

Figure 5.14: The FCC ANN performance for $B_{2,1}$ prediction changing trend with ρ sweep from 0 to 3.

Theoretically, the value of ρ can be selected from any point where the ANN model is performing an NMSE level below - 40 dB [12] for an accurate model. However, knowing from Fig.5.13 and 5.14 that the accuracy of determined ANN model decreases when ρ gets bigger, simultaneously, performs identically to the CM with ρ

approaching 0. In this specific case, $\rho = 0.9$ is selected to determine an accurate ANN model, but also different from the CM. With the defined $[HB]$, $[HW_2]$ and $[HW_3]$. (5.40) and (5.41) can now be solved to determine the associated $[OW_2]$ and $[OW_3]$ matrices.

Then, the value of $[CW]$ and $[OB]$ can all be calculated and listed as follows:

$$\left[HW\right] = \begin{bmatrix} HW_2 \\ HW_3 \end{bmatrix} = \begin{bmatrix} HW_{1,1} & HW_{1,2} \\ HW_{2,1} & HW_{2,2} \\ HW_{3,1} & HW_{3,2} \\ HW_{4,1} & HW_{4,2} \\ HW_{5,1} & HW_{5,2} \\ HW_{6,1} & HW_{6,2} \\ HW_{7,1} & HW_{7,2} \end{bmatrix} = \begin{bmatrix} 0.6364 & 0.6364 \\ 0 & 0.9 \\ -0.6364 & 0.6364 \\ 0.7281 & 0.5290 \\ 0.2781 & 0.8560 \\ -0.2781 & 0.8560 \\ -0.7281 & 0.5290 \end{bmatrix} \tag{5.47}$$

$$\begin{aligned} \left[OW\right] &= \begin{bmatrix} OW_2 & OW_3 \end{bmatrix} \\ &= \begin{bmatrix} OW_{1,1} & OW_{1,2} & OW_{1,3} & OW_{1,4} & OW_{1,5} & OW_{1,6} & OW_{1,7} \\ OW_{2,1} & OW_{2,2} & OW_{2,3} & OW_{2,4} & OW_{2,5} & OW_{2,6} & OW_{2,7} \end{bmatrix} \\ &= \begin{bmatrix} 0.0581 & 0.6176 & 0.9579 & 0.0191 & -0.1231 & 1.3936 & 0.3113 \\ 0.4517 & -0.5826 & 0.7844 & 0.7317 & -0.4842 & 0.5626 & 0.1400 \end{bmatrix} \end{aligned} \tag{5.48}$$

$$\begin{bmatrix} CW_{1,1} & CW_{1,2} \\ CW_{2,1} & CW_{2,2} \end{bmatrix} = \begin{bmatrix} 0.4053 & -1.9500 \\ -0.0343 & -1.2136 \end{bmatrix} \tag{5.49}$$

$$\begin{bmatrix} OB_{1,1} \\ OB_{2,1} \end{bmatrix} = \begin{bmatrix} -0.1835 \\ -0.2773 \end{bmatrix} \tag{5.50}$$

Performing a feedforward process on the generated FCC ANN, with the weights and biases listed above, results in a set of $B_{2,1}$ data that can be compared with the $B_{2,1}$

data that is collected from the simulation, see Fig. 5.15.

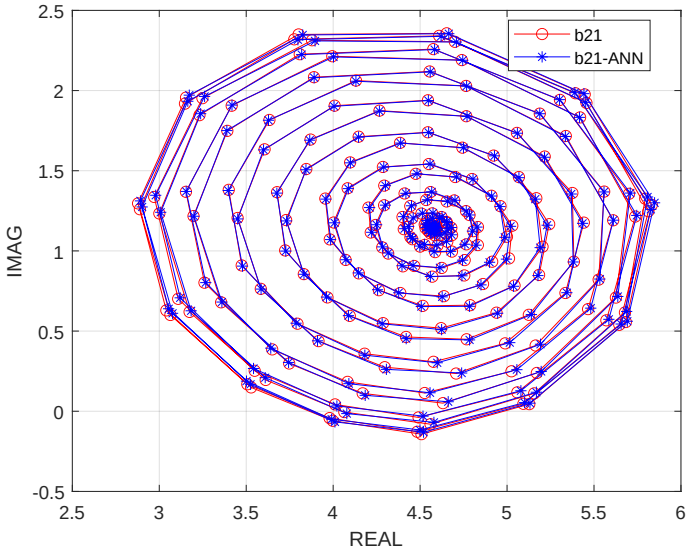

Figure 5.15: The $B_{2,1}$ prediction from the determined FCC ANN (blue stars) and the $B_{2,1}$ acquired from the simulation with complete data complexity (red circles) of the Wolfspeed device.

5.2.3 Repeated Analysis for DC Component

Modelling DC components is essential when developing design-relevant models since it is related to device efficiency performance, which is one of the key factors to expect as a design target. The $B_{2,0}$ plotted in Fig. 5.16, which is the DC drain current collected from ADS simulation, also has a spectrum complexity consistent with the model order of 3. Therefore, 10 CM coefficients are extracted for the ANN determination, listed in Table 5.2, for the same 7 hidden neuron structure as for the $B_{2,1}$.

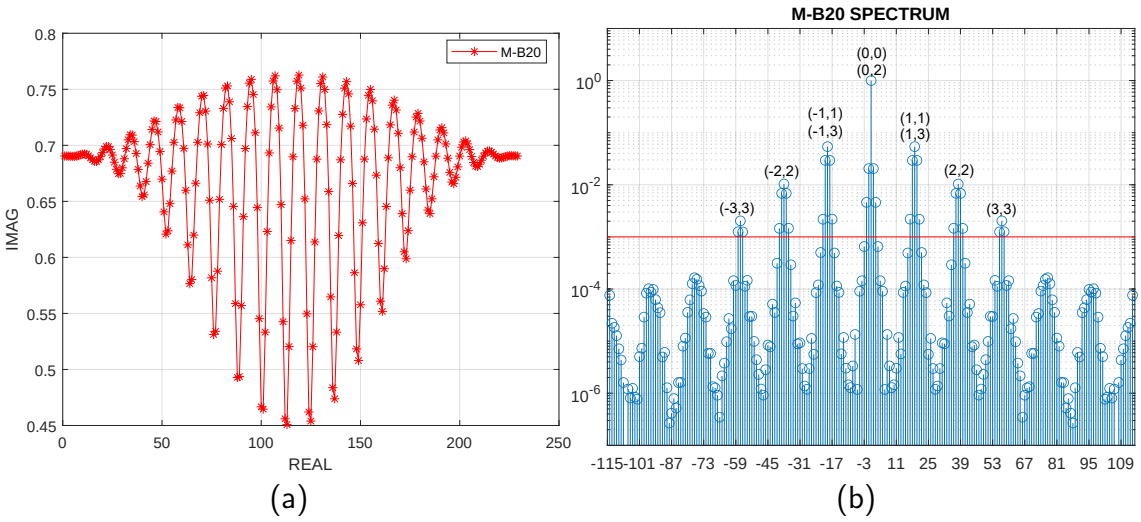

Figure 5.16: $B_{2,0}$ sample (a) and its Fourier Transformed spectrum (b) with error bar (red) on the trajectory computation, and the expected exponents' $|A_{2,1}|^m(\angle A_{2,1})^n$ values of the CM for extracting coefficients in (n,m).

Table 5.2: The Extracted CM Coefficients For $B_{2,0}$ of the Wolfspeed device

				$M_{2,0,m,n}$	
index	*r*	*n*	*m*	*Real*	*Imag.*
1	0	0	0	0.0126	0
2	0	1	1	0.0115	0.0234
3	0	-1	1	0.0115	-0.0234
4	0	2	2	0.0104	-0.0127
5	1	0	2	-0.0487	0
6	0	-2	2	0.0104	0.0127
7	1	3	3	-0.0065	-0.0029
8	1	1	3	0.0226	0.0224
9	0	-1	3	0.0226	-0.0224
10	0	-3	3	-0.0065	0.0029

Here, $\rho = 0.9$ is still the selected case following the ρ sweep. Therefore, the value of $[HB]$ and $[HW]$ will stay the same as previously listed with the phase angles determined in section 5.1.5. The calculated values of weights and biases (using (5.51)-(5.53)) are listed below. Performing a feedforward process on the determined ANN model, the predicted set of $B_{2,0}$ data can be compared with the $B_{2,0}$ data that

is collected from the simulation, see Fig. 5.17.

$$\begin{aligned}\begin{bmatrix} OW \end{bmatrix} &= \begin{bmatrix} OW_2 & OW_3 \end{bmatrix} \\ &= \begin{bmatrix} OW_{1,1} & OW_{1,2} & OW_{1,3} & OW_{1,4} & OW_{1,5} & OW_{1,6} & OW_{1,7} \\ OW_{2,1} & OW_{2,2} & OW_{2,3} & OW_{2,4} & OW_{2,5} & OW_{2,6} & OW_{2,7} \end{bmatrix} \\ &= \begin{bmatrix} 0.0084 & 0.1328 & 0.1711 & -0.0985 & 0.0303 & 0.2010 & 0.1425 \\ 0 & 0 & 0 & 0 & 0 & 0 & 0 \end{bmatrix}\end{aligned} \tag{5.51}$$

$$\begin{bmatrix} CW_{1,1} & CW_{1,2} \\ CW_{2,1} & CW_{2,2} \end{bmatrix} = \begin{bmatrix} 0.3148 & -0.4240 \\ 0 & 0 \end{bmatrix} \tag{5.52}$$

$$\begin{bmatrix} OB_{1,1} \\ OB_{2,1} \end{bmatrix} = \begin{bmatrix} -0.1677 \\ 0 \end{bmatrix} \tag{5.53}$$

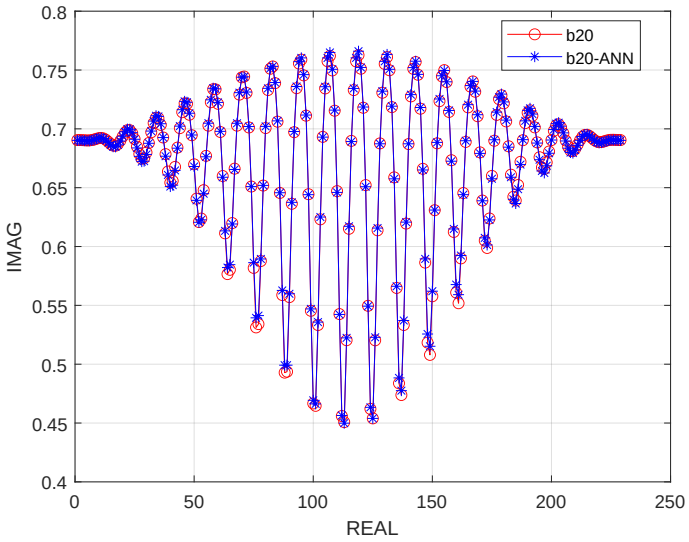

Figure 5.17: The $B_{2,0}$ prediction from the determined FCC ANN (blue stars) and the $B_{2,0}$ acquired from the simulation with complete data complexity (red circles) of the Wolfspeed device.

When considering the coefficients in Table 5.2, a clear pattern can be seen when the coefficients are extracted as conjugated pairs. This will result in having the $[M_i]$

matrices simplified in dimension because the sum of the imaginary parts is 0. In this case, the imaginary part from the output of the FCC ANN does not have to be hard-wired to 0 as when using the conventional ANN structure. The imaginary part will be 0 directly after the calculation.

5.2.4 Power and Efficiency Contour Plots

With both $B_{2,1}$ and $B_{2,0}$, the prediction results for the output power and efficiency contours are shown in Fig. 5.18 - 5.19. The NMSE calculated between the proposed method (determined FCC ANN model) and the simulated dataset demonstrates an NMSE error level lower than - 50 dB [12] for both of the output power and efficiency contours. In this case, the proposed method for determining the FCC ANN behavioural model structure using the CM coefficients is proven accurate.

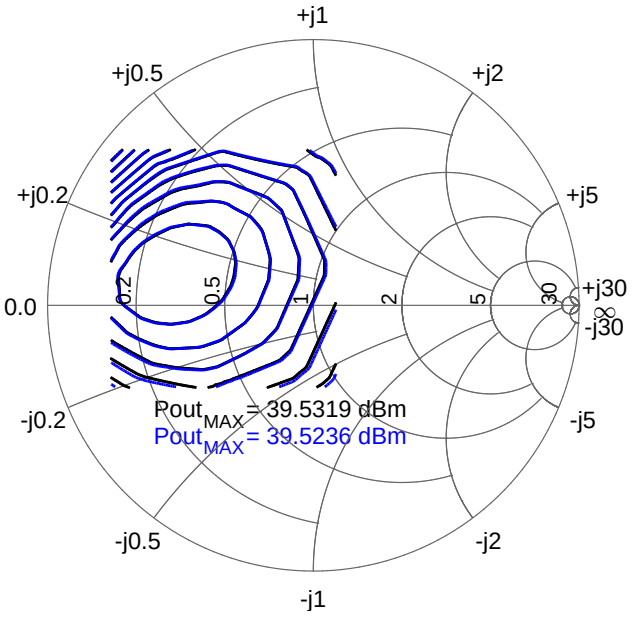

Figure 5.18: The predicted (blue) and simulated (black) output power comparison of the Wolfspeed device.

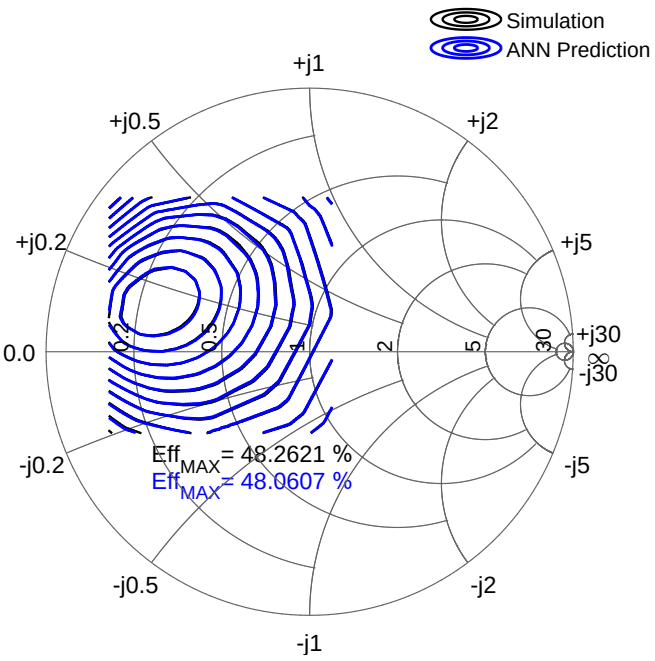

Figure 5.19: The predicted (blue) and simulated (black) efficiency contours comparison of the Wolfspeed device.

5.3 Method Verification with Measurement

For verifying the method robustness with different RF devices, a high-density load-pull measurement was set up for a WIN NP12 4×75 GaN on-wafer device at 20 GHz, biased with $V_{DS} = 15\,V$, $I_{DS} = 30\,mA$. In Fig. 5.20 - 5.21, the data is collected with a constant input drive corresponding to 3 dB compression at the optimum load for acquiring a dataset with higher complexity.

To allow the analysis in [16] with tailored datasets, an equivalent set of manually calculated modulated stimulus signal $A_{2,1}$ generated as a reference for choosing data points from the measurement dataset, as shown in Fig. 5.21. To get a clean spectrum plot with a noise floor lower than - 60 dB, the selected measurement $A_{2,1}$ dataset, needs to be a good match, at least within - 35 dB error level, to the ideal modulated $A_{2,1}$ dataset.

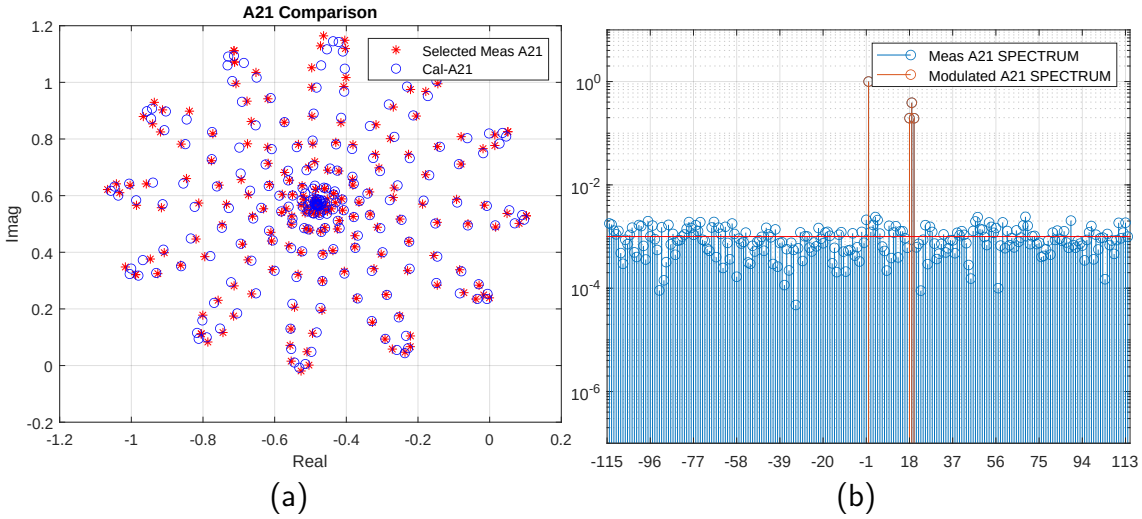

Figure 5.20: Selected $A_{2,1}$ samples (a) from the calculation (blue circles)and picked from measurement (red dots) and its Fourier Transformed spectrum comparison (b, calculated shown in red and measured shown in blue) on a trajectory computed using 229 simulated points. of the WIN device measurement

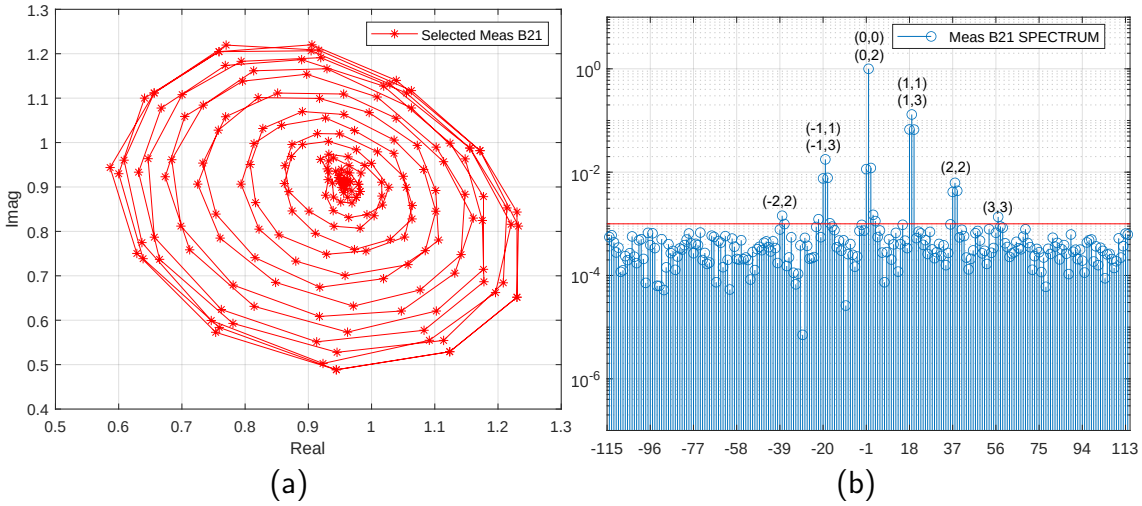

Figure 5.21: $B_{2,1}$ sample (a) and its Fourier Transformed spectrum (b) with -60 dB error bar (red) on the trajectory computation, and the expected exponents' $|A_{2,1}|^m(\angle A_{2,1})^n$ values of the CM for extracting coefficients in (n,m) of the WIN device measurement.

5.3.1 Model Determination

According to the response Fourier Transformed spectrum in Fig. 5.21, 9 pairs of magnitude and phase-restricted terms exponents can be defined. The correlated extracted coefficients are calculated and listed in Table 5.3. Based on the CM reformulation (5.4), all the exponents' pairs related coefficient components are required

for a 3^{rd} polynomial order case, because of the $[M_o]$ matrices. When any of them do not exist on the spectrum plot, the coefficient values will be set to 0.

Table 5.3: The Extracted CM Coefficients For $B_{2,1}$ of the WIN device measurement

				$M_{2,1,m,n}$	
index	*r*	*n*	*m*	*Real*	*Imag.*
1	0	0	0	0.7589	0.7178
2	0	1	1	0.0010	-0.5840
3	0	-1	1	0.0599	-0.0622
4	0	2	2	0.0374	-0.0629
5	1	0	2	-0.1485	-0.1334
6	0	-2	2	-0.0098	0.0125
7	1	3	3	0.0021	-0.0319
8	1	1	3	0.0534	0.0152
9	0	-1	3	0.0130	0.1072
10	0	-3	3	0	0

The required analysis with the ρ sweep plan and the calculation is done. According to the results shown in Fig. 5.22, $\rho = 1.2$ is selected in this case for good model performance. The prediction results for the $B_{2,1}$ are shown in Fig. 5.23.

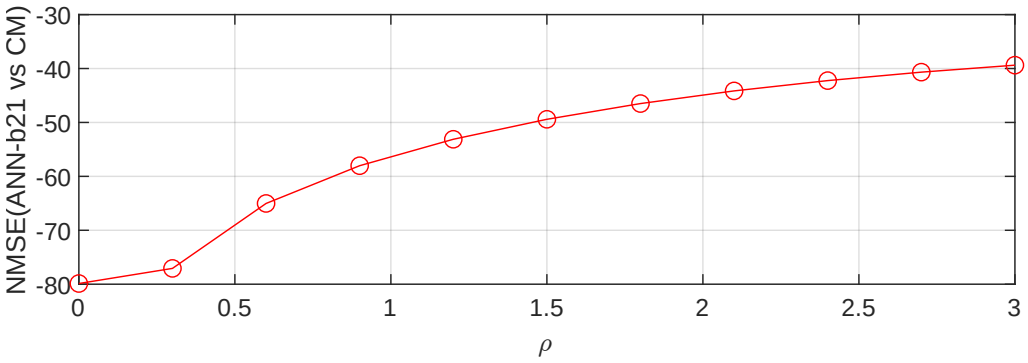

(a) NMSE from ANN prediction vs. CM prediction

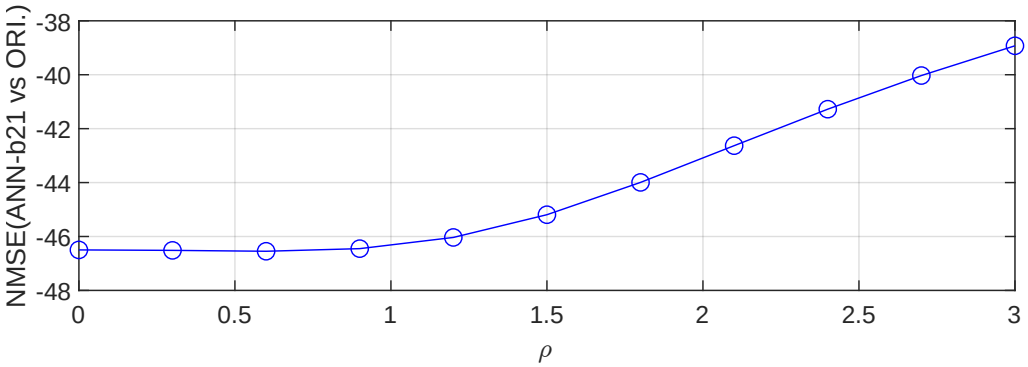

(b) NMSE from ANN prediction vs. Simulation data

Figure 5.22: The FCC ANN performance for $B_{2,1}$ prediction of the WIN device changing trend with ρ sweep from 0 to 3.

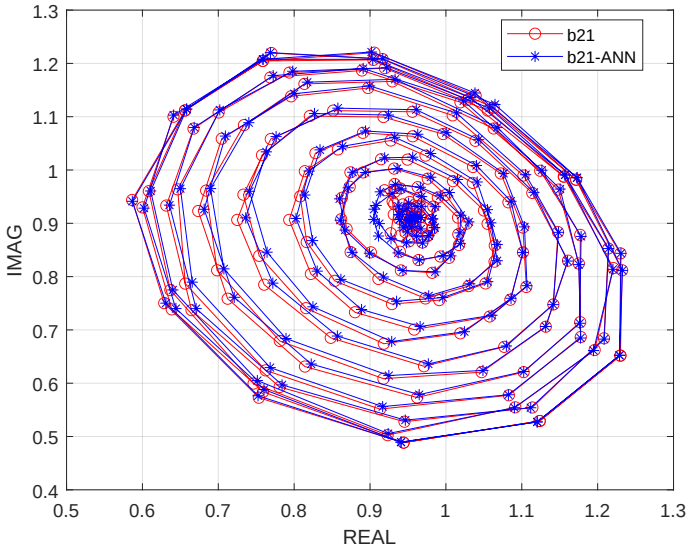

Figure 5.23: The $B_{2,1}$ prediction of the WIN device from the determined FCC ANN (blue stars) and the $B_{2,1}$ acquired from the measurement with the analyzed data complexity (red circles).

Repeating the same procedure for the DC component, $B_{2,0}$, which is the drain cur-

rent. As shown in the spectrum plot from Fig. 5.24, there are 3^{rd} order terms located close to the - 60 dB noise floor, highlighted in yellow, which could be potentially picked. However, the experiment demonstrates that the FCC ANN models determined without the 3^{rd} order terms are accurate enough, performing an NMSE level lower than - 40 dB. Here, with the 6 extracted CM coefficients listed in Table 5.4, the FCC ANN model determined using the proposed method with 3 hidden neurons in the hidden layer is providing $B_{2,0}$ predictions as in Fig. 5.25.

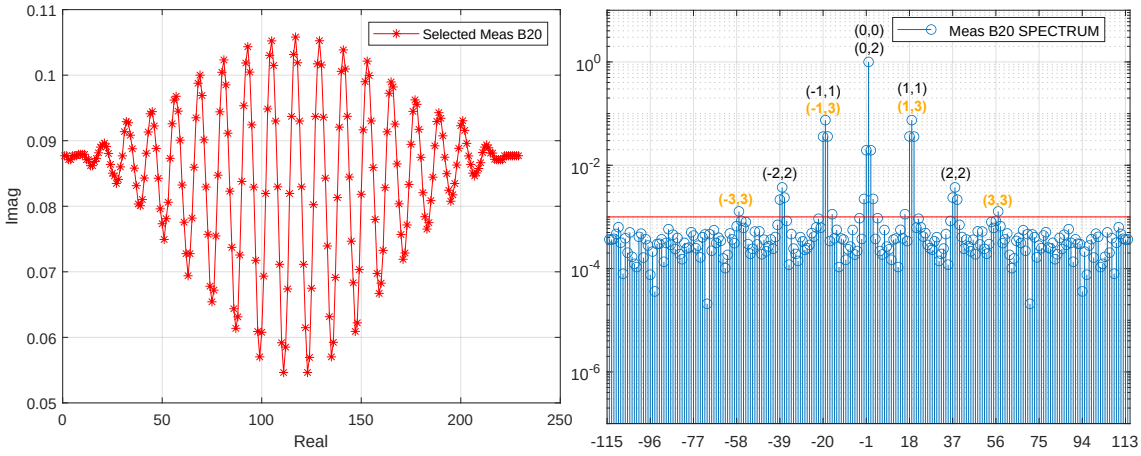

Figure 5.24: $B_{2,0}$ sample (a) and its Fourier Transformed spectrum (b) with - 60 dB error bar (red) on the trajectory computation, and the expected exponents'$|A_{2,1}|^m(\angle A_{2,1})^n$ values of the CM for extracting coefficients in (n,m).

Table 5.4: The Extracted CM Coefficients For $B_{2,0}$ of the WIN device

				$M_{2,0,m,n}$	
index	*r*	*n*	*m*	*Real*	*Imag.*
1	0	0	0	0.0036	0
2	0	1	1	0.0096	0.0192
3	0	-1	1	0.0096	-0.0192
4	0	2	2	-0.0009	-0.0025
5	1	0	2	-0.0213	0
6	0	-2	2	-0.0009	0.0025

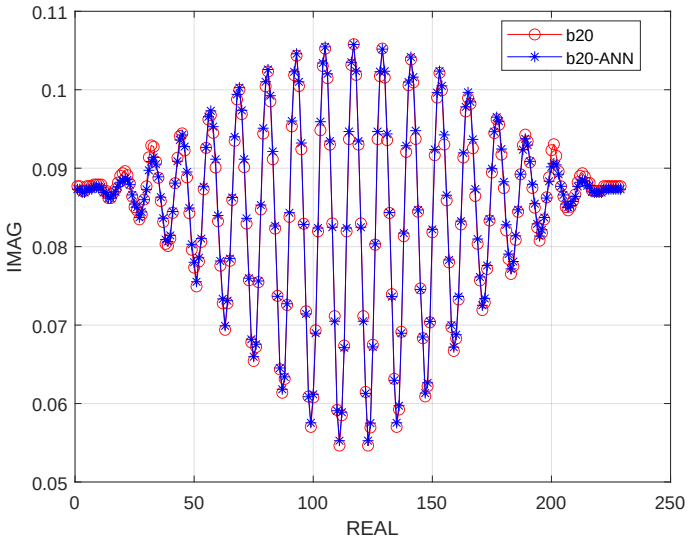

Figure 5.25: The $B_{2,0}$ prediction of the WIN device from the determined FCC ANN (blue stars) and the $B_{2,0}$ acquired from the measurement with the analyzed data complexity (red circles).

With both $B_{2,0}$ and $B_{2,1}$, the prediction results for the output power and efficiency contours for the WIN device are shown in Fig. 5.26 - 5.27. The NMSE calculated between the proposed method (determined FCC ANN model) and the measured dataset are both below - 40 dB [12] for the output power and efficiency contours.

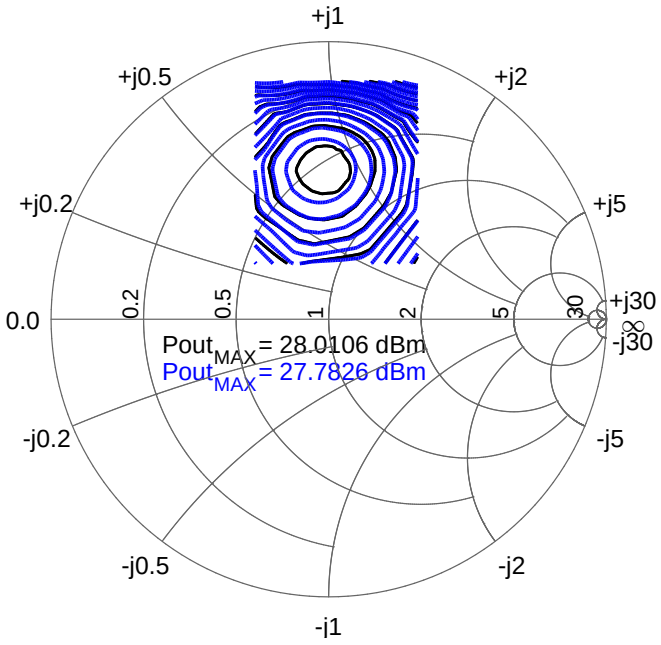

Figure 5.26: The predicted (blue) and measured (black) output power contours of the WIN device.

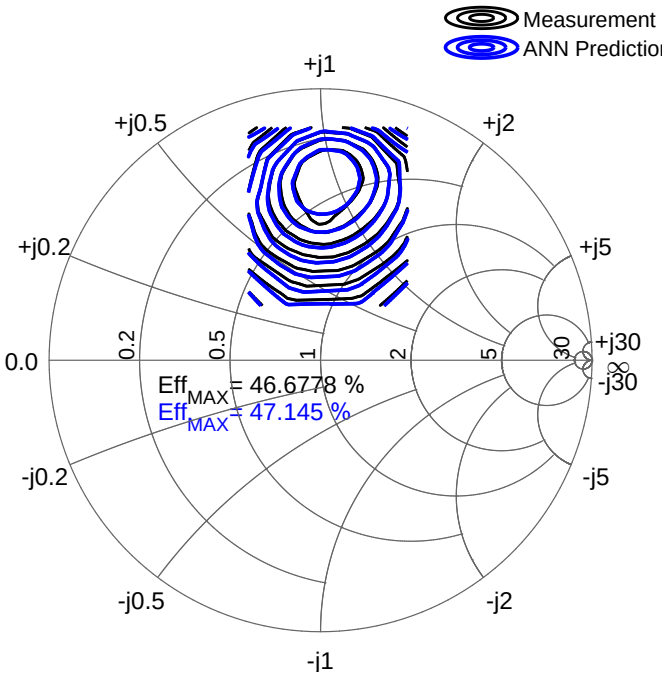

Figure 5.27: The predicted and measured efficiency contours of the WIN device.

5.3.2 Model Extrapolation Ability

While the range of $A_{2,1}$ values is limited during measurement because of transistor operation and measurement system limitations, much larger values of $A_{2,1}$ corresponding to loads covering the whole Smith Chart are possible during CAD optimisation. The extrapolation capability of both models therefore needs to be tested using an appropriately expanded $A_{2,1}$ range.

A set of $A_{2,1}$ is manually generated, with a maximised coverage surrounding the measured $A_{2,1}$ dataset in circles for model extrapolation ability investigation. The corresponding output power and efficiency contours are shown in Fig. 5.28 - 5.29. The problem regions, shown with the prediction results provided by the original CM coefficients, are zoomed in and highlighted with annotations to identify erroneous behaviours.

The results in erroneous performance predictions can be better visualised in Fig. 5.30. The raised features and erroneous predictions, provided by the original

CM coefficients used for determining the ANN structure, are not presented in the results offered by the proposed method-determined ANN model.

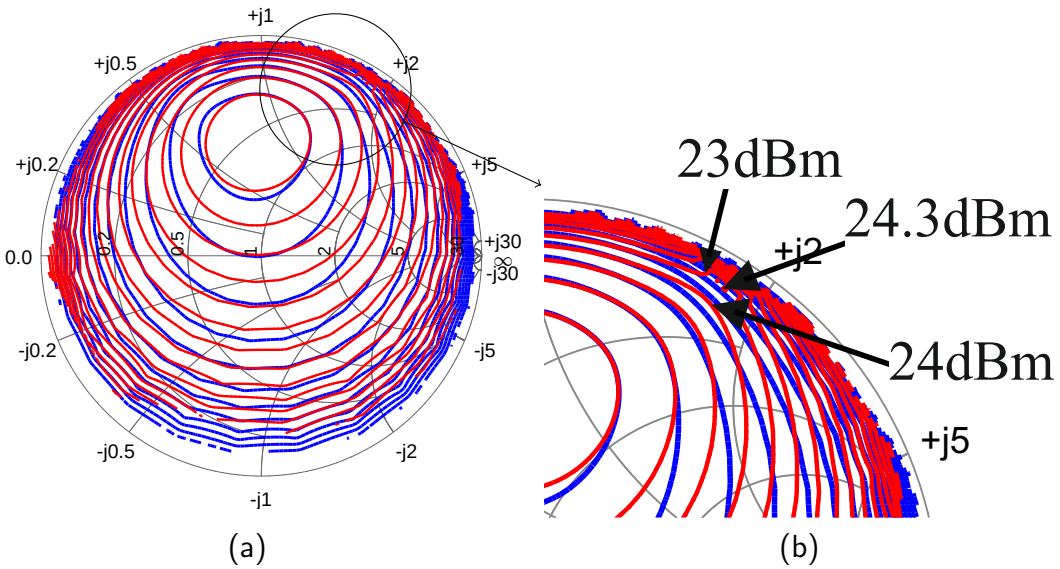

Figure 5.28: Comparison of CM (red) and ANN (blue) modelling of the output power contours of the WIN device.

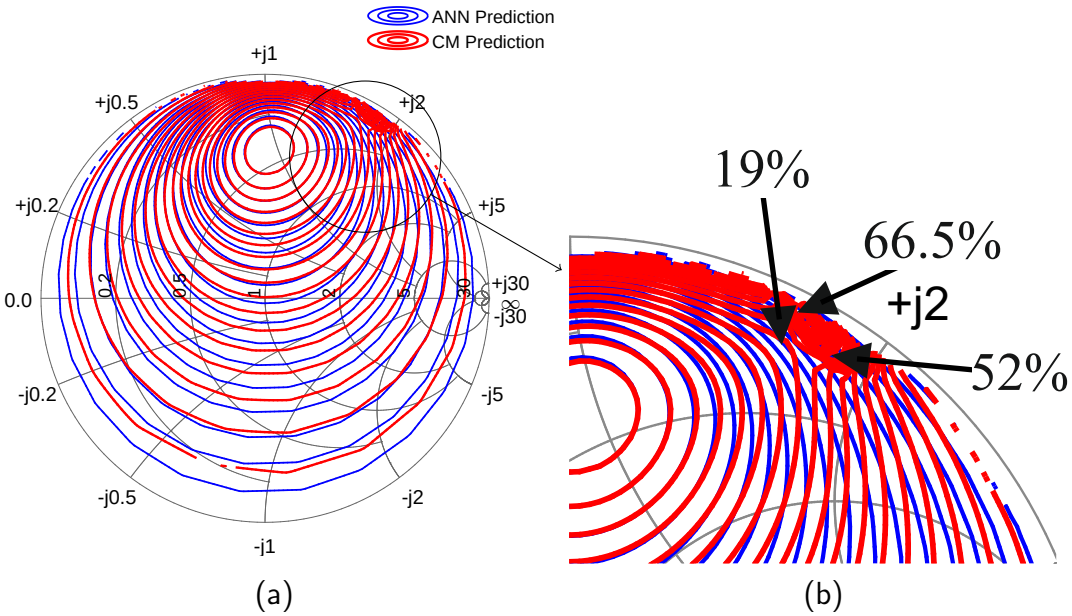

Figure 5.29: Comparison of CM (red) and ANN (blue) modelling of the efficiency contours of the WIN device.

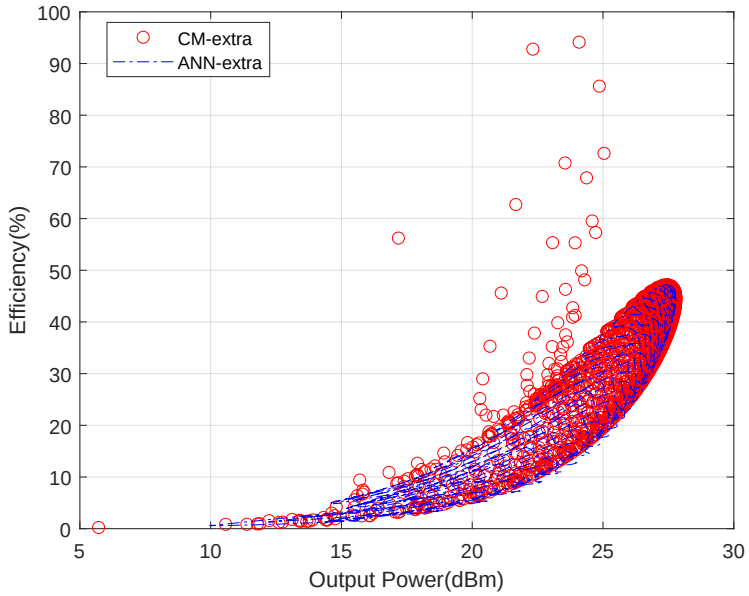

Figure 5.30: Modeled efficiency vs. output power for the WIN device models, including the extrapolation region. CM (red circles) and ANN (blue line).

5.4 Discussion

The method developed has proven robust enough to determine both an appropriate FCC ANN model structure and the determined set of ANN model parameters, weights and bias values, using both simulated and measured transistor load-pull datasets. Several significant observations need to be discussed.

When determining the ANN structure through the established equations based on the extracted CM coefficient matrices' dimension, alternatively, a pseudo-inverse can also be applied to the calculation process. In this case, a square matrix is no longer required for the matrix calculation, hence, the required number of hidden neurons in the determined structure could be potentially reduced without compromising the model accuracy.

The phase angle selection, mentioned in the $[HW]$ dimension analysis and determining section, highlights multiple valid, non-singular solutions that can be applied to the matrices since the correlated magnitude term 'ρ' and phase angles 'θ' can be

varied. When varying the phase angles 'θ' over $0° - 360°$, there can be multiple (repeating) solutions of the $[HW]$ matrix which can all provide an invalid, singular matrix condition. Hence, multiple determination options can be possible for the ANN model parameters to enable an accurate model performance. All these solutions can provide similar model performance.

Consider now in this chapter, the selection of 'ρ', which defines tanh function operational range of the ANN hidden nodes and the accuracy of the determined ANN model, is selected with sweep plans. This can be further investigated for a method for optimal selection. Besides, although there is no ANN training process presented in this work, there is a potential that varying the value of ρ can have an impact on the training if required.

5.5 Conclusion

In this chapter, a novel method, based on the CM, that determines the structure of a FCC ANN model is introduced. The proposed method is proven appropriate for non-linear transistor modelling. In addition, a method for determining the values of the ANN model parameters, values of the required weights and biases, from the coefficients of the CM extracted by analysing tailored load-pull measurement datasets has been formulated.

With the dataset collected from the Wolfspeed GaN device load-pull simulation in ADS, the method has produced an accurate ANN model with an error level lower than - 50 dB. For the WIN GaN device measurement dataset, the proposed method also produces an accurate ANN model with an error level lower than - 40 dB.

In addition, under a practical load-pull measurement scenario, the verification demonstrates that the coefficients of the CM extracted by analysing tailored load-pull measurement datasets do not always guarantee a reasonable extrapolation

ability. The extrapolation ability of ANN models determined with the proposed methods is proven more robust on extrapolation prediction than that of the extracted CM coefficients.

References

[1] Villiers, J. d., E. Barnard, "Backpropagation neural nets with one and two hidden layers," *IEEE Transactions on Neural Networks*, vol. 4, no. 1, pp. 136–141, Jan. 1993. DOI: 10.1109/72.182704.

[2] Kwok, T. .-., Yeung, D. .-., "Constructive algorithms for structure learning in feedforward neural networks for regression problems," *IEEE Transactions on Neural Networks*, vol. 8, no. 3, pp. 630–645, Mar. 1997. DOI: 10.1109/72.572102.

[3] D. Hunter, H. Yu, M.S. Pukish, I., J. Kolbusz, B.M. Wilamowski, "Selection of Proper Neural Network Sizes and Architectures—A Comparative Study," *IEEE Transactions on Industrial Informatics*, vol. 8, no. 2, pp. 228–240, Feb. 2012. DOI: 10.1109/TII.2012.2187914.

[4] R. J. Jesus, M. L. Antunes, R. A. da Costa, S. N. D., J. F. F. Mendes, R. L. Aguiar, "Effect of Initial Configuration of Weights on Training and Function of Artificial Neural Networks," *Mathematics*, vol. 9, no. 18, p. 2246, Sep. 2021. DOI: 10.3390/math9182246.

[5] G. Thimm, E. Fiesler, "High-order and multilayer perceptron initialization," *IEEE Transactions on Neural Networks*, vol. 8, no. 2, pp. 349–359, Feb. 1997. DOI: 10.1109/72.557673.

[6] X. Glorot, Y. Bengio, "Understanding the difficulty of training deep feedforward neural networks," in *Proceedings of the Thirteenth International Conference on Artificial Intelligence and Statistics*, Y. W. Teh and M. Titterington, Eds., ser. Proceedings of Machine Learning Research, vol. 9, Chia Laguna Resort, Sardinia, Italy: PMLR, May 2010, pp. 249–256. [Online]. Available: https://proceedings.mlr.press/v9/glorot10a.html.

[7] A. Jarndal, S. Husain, M. Hashmi, "Genetic algorithm initialized artificial neural network based temperature dependent small-signal modeling technique for GaN high electron mobility transistors," *International Journal of RF and Microwave Computer-Aided Engineering*, vol. 31, no. 3, e22542, Jan. 2021. DOI: https://doi.org/10.1002/mmce.22542. eprint: https://onlinelibrary.

wiley.com/doi/pdf/10.1002/mmce.22542. [Online]. Available: https://onlinelibrary.wiley.com/doi/abs/10.1002/mmce.22542.

[8] Q. -J. Zhang, K. C. Gupta, *Neural Networks for RF and Microwave Design*. Boston, MS, USA: Artech House, 2000.

[9] A. Khusro, S. Husain, M.S. Hashmi, A.Q. Ansari, "Small signal behavioral modeling technique of GaN high electron mobility transistor using artificial neural network: An accurate, fast, and reliable approach," *International Journal of RF and Microwave Computer-Aided Engineering*, vol. 30, no. 4, e22112, Apr. 2020. DOI: https://doi.org/10.1002/mmce.22112.

[10] H. Qi, J. Benedikt, P. Tasker, "A Novel Approach for Effective Import of Nonlinear Device Characteristics into CAD for Large Signal Power Amplifier Design," in *2006 IEEE MTT-S International Microwave Symposium Digest*, San Francisco, CA, USA, Jun. 2006, pp. 477–480. DOI: 10.1109/MWSYM.2006.249596.

[11] P.J. Tasker, J. Benedikt, "Waveform Inspired Models and the Harmonic Balance Emulator," *IEEE Microwave Magazine*, vol. 12, no. 2, pp. 38–54, Apr. 2011. DOI: 10.1109/MMM.2010.940101.

[12] M.R. Moure, M. Casbon, M. Fernández-Barciela, P.J. Tasker, "Direct extraction of an admittance domain behavioral model from large-signal load-pull measurements," in *2017 IEEE MTT-S International Microwave Symposium (IMS)*, Honololu, HI, USA, Jun. 2017, pp. 1057–1060. DOI: 10.1109/MWSYM.2017.8058775.

[13] V.K. Devabhaktuni, C. Xi, F. Wang, Q.J. Zhang, "Robust training of microwave neural models," in *1999 IEEE MTT-S International Microwave Symposium Digest (Cat. No.99CH36282)*, vol. 1, Anaheim, CA, USA, Jun. 1999, 145–148 vol.1. DOI: 10.1109/MWSYM.1999.779444.

[14] W. Fang, Q.J. Zhang, "Knowledge based neural models for microwave design," in *1997 IEEE MTT-S International Microwave Symposium Digest*, vol. 2, Denver, CO, USA, Jun. 1997, 627–630 vol.2. DOI: 10.1109/MWSYM.1997.602870.

[15] J.C. Pedro, S.A. Maas, "A comparative overview of microwave and wireless power-amplifier behavioral modeling approaches," *IEEE Transactions on Microwave Theory and Techniques*, vol. 53, no. 4, pp. 1150–1163, Apr. 2005. DOI: 10.1109/TMTT.2005.845723.

[16] P.J. Tasker, "Robust Extraction of Cardiff Model Parameters from Appropriately Tailored Measured Load-Pull Data," in *2020 IEEE BiCMOS and Compound Semiconductor Integrated Circuits and Technology Symposium (BCI-*

CTS), Monterey, CA, USA, Nov. 2020, pp. 1–5. DOI: 10.1109/BCICTS48439.2020.9392942.

[17] T. Husseini, A. Al-Rawachy, J. Benedikt, J. Bell, P. Tasker, "Global Behavioural Model Generation Using Coefficients Interpolation," in *2019 IEEE MTT-S International Microwave Symposium (IMS)*, Boston, MA, USA, Jun. 2019, pp. 200–203. DOI: 10.1109/MWSYM.2019.8700998.

[18] H. Qi, J. Benedikt, P.J. Tasker, "Nonlinear Data Utilization: From Direct Data Lookup to Behavioral Modeling," *IEEE Transactions on Microwave Theory and Techniques*, vol. 57, no. 6, pp. 1425–1432, Jun. 2009. DOI: 10.1109/TMTT.2009.2019996.

[19] B.L. Kalman, S.C. Kwasny, "Why tanh: choosing a sigmoidal function," in *[Proceedings 1992] IJCNN International Joint Conference on Neural Networks*, vol. 4, Baltimore, MD, USA, Jun. 1992, 578–581 vol.4. DOI: 10.1109/IJCNN.1992.227257.

Chapter 6

Summary and Future Work

The results shown in Chapters 3-5 demonstrated that the proposed methods for extracting/determining behavioural models for RF devices, the invented Artificial Neural Network (ANN) based Cardiff Model (CM) coefficient extractor, the established equations allow the Fully Connected Cascaded (FCC) ANN model structure and values of weights and biases, are all verified to have reasonable extrapolation predicting ability while maintaining the interpolation prediction accuracy, in the meantime, proven robust enough with different device responses.

A behavioural model with reasonable extrapolation ability creates the opportunity for breaking away from the limitation of model extraction with practical load-pull measurements. This enables much larger operational coverage on the Smith Chart when utilising behavioural models during CAD optimisation for RF design tasks with a limited set of practical measurement data. Hence, a more efficient modelling procedure, which attains the objective of this work.

6.1 Summary

Specific problems investigated for model extrapolation ability have been solved by proposing targeted methods.

It is investigated in Chapter 3 that an overdetermined CM will potentially bring erroneous extrapolation predictions, in a practical scenario when the tailored datasets for determining a proper model to extract the CM are not available. In the meantime, the conventional A-B wave-based FCC ANN is proven possible to provide a more reasonable extrapolation prediction than that of the CM, with proper configuration. Since it is illustrated that the CM requires less runtime to be processed in a CAD environment. The ANN based CM coefficient extractor is invented in Chapter 4 to address the high user-defined CM order extrapolation issue.

The invention in Chapter 4 relies on modifying the conventional Levenberg-Marquardt (LM) backpropagation training algorithm. The modification is done on the error calculation condition statement of the LM algorithm. with a combination of the A-B wave-based ANN model and the modified LM algorithm, the ANN based CM coefficient extractor is invented. It allows the coefficients to be extracted with a high user-defined order CM to obtain high interpolation accuracy and reasonable extrapolation ability.

The challenge for practically utilising the invented high order CM coefficient extractor is captured from Chapter 4. The invented ANN based CM coefficient extractor, which allows reasonable extrapolation ability, contains a 'random' model determination of the conventional A-B wave based ANN behavioural model configuration. The structure and the internal parameters of the ANN are selected relying on sweep plans based on experiences. To escape from falling into traps when searching for a proper ANN model, a set of equations is established for using the extracted CM coefficients to determine an ANN configuration properly in Chapter 5.

The proposed methods in Chapter 5 with the established equations permit A-B wave-based ANN models to be determined with physics-based theory. By expanding the CM and the ANN implementing formulation with the Taylor series expansion theory, it is observed that the two models share similar polynomial structures that can be compared. The set of equations is established in the process of rearranging and equalising the CM and the ANN formulation. It is verified that ANN structure determined by the required matrices dimension of the established equations, and the ANN weights and biases values calculated from the CM coefficients enable ANN models to be accurate for interpolation and reasonable for extrapolation without the backpropagation training process.

6.2 Future Work

The proposed methods in this work have fulfilled the aim to a degree that allows the CM or the ANN behavioural model to be more robust compared to their conventional extraction process when utilised in a CAD environment. However, future work still calls for development based on the current progress. Further exploration can be suggested to focus on optimisation, or application range expansion of the proposed methods in this work.

If prioritising the proposed methods' further optimisation perspective, it is illustrated in the discussion section of Chapter 5, where there are remaining significant investigations for the ANN determination process:

The calculation process of the established equations in Chapter 5, allows the ANN structure to be determined from the reformulated CM coefficient matrices with dimension based on the analysed polynomial order. Experiments have been implemented in MATLAB, which presented that pseudo-inverse for matrices calculation enables a reduction of hidden neuron numbers for the determined ANN structure. Moving on to the hidden weights determining process, the correlated magnitude

parameter allows flexible activation function operational range selection; phase parameters yield multiple possible solutions for an accurate ANN to be configured through the established equations. All three parameters indicate that the ANN determination through the CM can be further optimised.

According to the experiments done for the conventional A-B wave-based ANN structure in Chapter 3, when multiple solutions for an accurate ANN model appear, the extrapolation ability presented can be different from one solution to another, even the interpolation accuracy is at a similar level. Now in this work, the performance of extrapolation predictions is not fully analysed with all the possible optimised solutions. The selected approach follows the results offered by sweep plans for ensuring the determined ANN models are neither identical nor entirely different to the extracted CM. Further study can be developed on the relationship between the magnitude and phase parameters to the extrapolation ability of the hidden neuron number minimised ANN models determined from extracted CMs among all the possible solutions.

It is noteworthy to mention that the tailored datasets for nonlinearity analysis on determining a proper model to extract the CM are not always available with practical load-pull measurement systems. However, to ensure the reasonable extrapolation ability for the CM determined ANN in Chapter 5, the tailored datasets are still utilised to properly define the required model order based on specific data complexity. Although it is mentioned that the ANN structure can be simplified, hence, speeding up the ANN model processing time when implemented in a CAD environment. Also, an alternative method is introduced, for acquiring a tailored dataset from practical load-pull measurements by processing high-density datasets. It can be expensive to achieve based on the fact that a high-density load-pull highly depends on the precision of the measurement setup. A trade-off between the ANN training time and the high-density load-pull measurement cost may need to be taken into consideration when selecting from the proposed methods.

Verification experiments done to prove the accuracy, extrapolation ability and robustness of the proposed methods in this work were based on fundamental load-pull measurements. To further expand the application range of the proposed methods, datasets that contain harmonic effects should be studied. Theoretically, the proposed methods should be expandable for higher levels of nonlinearity/system complexity, since the provided formulations are all generalised, and the theory based on the conventional CM and ANN are both proven valid across harmonics. Verification with harmonic measurements can then further convince the proposed methods in this work for practical utilisation in RF-related tasks.